NOVEL OPTIMIZATION METHODS IN MICROWAVE ENGINEERING: APPLICATIONS IN IMAGING AND DESIGN

By

Ali Khalatpour, B.Sc.

A Thesis
Submitted to the School of Graduate Studies
in Partial Fulfillment of the Requirements
For the Degree
Master of Applied Science

McMaster University

ABSTRACT

In this thesis, inverse problems related to microwave imaging and microwave component design are investigated. Our contribution in microwave imaging for breast tumor detection can be divided into two parts. In the first part, a vectorial 3D near-field microwave holography is proposed which is an improvement over the existing holography algorithms. In the second part, a simple and fast post-processing algorithm based on the principle of blind de-convolution is proposed for removing the integration effect of the antenna aperture. This allows for the data collected by the antennas to be used in 3D holography reconstruction. The blind deconvolution algorithm is a well-known algorithm in signal processing and our contribution here is its adaptation to microwave data processing.

Second, a procedure for accelerating the space-mapping optimization process is presented. By exploiting both fine- and surrogate-model sensitivity information, a good mapping between the two model spaces is efficiently obtained. This results in a significant speed-up over direct gradient-based optimization of the original fine model and enhanced performance compared with other space-mapping approaches. Our approach utilizes commercially available software with adjoint-sensitivity analysis capabilities.

ACKNOWLEDGEMENTS

It is a pleasure to thank many people who made this thesis possible. First and foremost, I offer my sincerest gratitude to my M.A.Sc. supervisor, Dr. Natalia K. Nikolova, who has supported me throughout my thesis with her patience and knowledge whilst allowing me the room to work in my own way. With her enthusiasm, inspiration, and her great efforts to explain things clearly and simply, she helped me to understand and proceed through this long way. Throughout my M.A.Sc program, she provided encouragement, sound advice, good teaching, good company, and lots of novel ideas. One simply could not wish for a better supervisor.

I would like to thank the members of my supervisory committee, Dr. Mohamed H. Bakr, and Dr. John W. Bandler, for their precious time and valuable suggestions for the work done in this thesis. I gratefully acknowledge Dr. John W. Bandler for providing me with the opportunity to learn about new concepts.

Furthermore, I am deeply indebted to my colleagues at the Computational Electromagnetics Laboratory at McMaster University for sharing their experience in research as well as participating in stimulating team discussions. I would especially like to thank my colleague and co-author Dr. Reza Khalaj Amineh for his valuable efforts and support. I was very lucky to have my wonderful colleagues and friends since they not only gave me support but also made my long journey much more cheerful. My thanks go to all the friends including Kaveh Moussakhani, Dr. Li Liu, Dr. Mohamed Swillam, Mohammad S. Dadash, Osman Ahmed, Mohamed Negm, Yifan Zhang, Arthur Montazeri, and Dr. Qingsha Chen.

Words fail me to express my appreciation to my beloved wife Maryam whose dedication, love and persistent confidence in me, has taken the load off my shoulder. I owe her for letting her intelligence, passions, and ambitions collide with mine, unselfishly. Therefore, I would also thank Amouzandeh's family for letting me take her hand in marriage and walk away to explore new opportunities together.

My deep love and appreciation goes to my family in Iran with whom I shared my childhood and whose love and support still sustain me today. My sister and brothers: Maryam, Yaser, and Mehdi who are all so much part of me and my memories of childhood. To my parents who gave me curiosity about life which has resulted in this thesis.

CONTENTS

CHAPTER 1

INTRODUCTION

Mathematically, problems in electromagnetics are divided into two major categories: inverse problems and forward problems [1]. In forward problems, the medium in which the waves propagate is known and the field solution is to be found. In the inverse problems, the field solution is partially known and the properties of the medium in which the wave propagates are sought.

In this thesis, inverse problems related to microwave imaging and microwave component design are investigated. In microwave imaging, the scattered electromagnetic wave in the observation domain is partially known through measurements while the incident field is known *a priori*. The objective is to reconstruct the electrical properties of the examined domain.

In the microwave design problem, we seek to optimize the structure's properties such as shape and material parameters based on design specifications.

1.1 MICROWAVE IMAGING FOR BREAST CANCER DIAGNOSTICS

Breast cancer is the most widespread cancer among women [2]. X-ray mammography [3][4] is one of the common approaches to early breast cancer diagnostics. There are several problems associated with this method. The most important is that 5%–15% of the tumors cannot be seen through mammography [4][5]. In addition, the ionization of tissues caused by X-rays prevents frequent examination of women. Magnetic resonance imaging (MRI) is known to be the most sensitive of the available approaches but it is expensive and is not broadly available [6]. Microwave imaging is a promising emerging modality for this purpose.

In 1979 Jacobi *et al.* [7] developed a water-immersed antenna system that was able to satisfactorily image canine kidney [8]. Later, research activities included experimental microwave imaging based mainly on linear reconstruction algorithms utilizing the Born and the Rytov approximations (e.g., see [9][10]). The performance of the linear reconstruction algorithms is limited to small low contrast objects [11][13]. Thus, the later developments have mainly been focused on iterative nonlinear reconstruction algorithms which can handle the case of strong complex scatterers. These algorithms, however, are more computationally intensive [14][21]. They are also inherently ill-posed and nonlinear. Often, the nonlinearity of the problem causes the algorithm to get trapped in a local minimum leading to an incorrect reconstruction results [22].

Radar-based imaging is another category of microwave imaging. In radar-based imaging, a map of the scattering based on the contrast in the dielectric properties within the breast is created. The radar approach was adopted from military and ground-penetrating applications and was adopted to breast-cancer detection in the late nineties by Benjamin [23][24] and Hagness [25]. In contrast to most optimization-based techniques, the proposed radar systems operate at higher frequencies (up to 10 GHz) and use a large bandwidth (as much as 8 GHz). Most of these radars are therefore ultrawide band (UWB). The scattering information is obtained from the transmission and the reception of short UWB electromagnetic pulses. The simplest algorithm proposed for radar-based imaging was a standard delay-and-sum (DAS) focusing [26]. More elaborate techniques such as microwave imaging via space-time (MIST) address some drawbacks of DAS. The MIST algorithm [27][28] outperforms mono-static DAS, although multi-static DAS still outperforms mono-static MIST [29]. An advantage of radar-based imaging over the optimization-based imaging is its relatively simple and robust signal processing. To date there have been only a few experimental breast-imaging radar systems reported in the open literature [27][30]-[32]. Although radar-based techniques have their advantages (e.g., simplicity), they provide limited performance in terms of image resolution and clutter rejection. In addition to the drawbacks mentioned above for optimization-based and radar-based techniques, most of the proposed imaging setups so far require immersing the antennas and the breast tissue in a coupling liquid. This not only complicates the maintenance and sanitation of the setup but also causes additional loss in microwave measurements. All of the above drawbacks have hindered the progress toward successful clinical trials.

Microwave holographic imaging is a technique which has been developed for concealed weapon detection in the Pacific Northwest National Laboratory [33][34] . It relies on the measurement of the magnitude and phase of the wave scattered from the imaged target on a rectangular or cylindrical aperture. Knowledge of the magnitude and phase across an aperture allows Fourier-transform (FT) based reconstruction of the target's reflectivity. This technique has been used to form high-resolution two-dimensional (2D) or three-dimensional (3D) images. Using wide-band frequency data allows for 3D image reconstruction. A successful implementation of the algorithm for detection of concealed weapons is reported in [33][34].

In order to be able to apply microwave holographic technique to near-field imaging such as breast cancer detection, the original technique has been modified in [35][38]. So far, microwave holography has been proposed for concealed weapon detection [33][34][39], near-field analysis of antennas [40], biomedical imaging [41], and non-destructive testing and evaluation [41].

1.2 MOTIVATION

In [41], a novel sensor is proposed to be used in microwave imaging for breast cancer detection. This new sensor has the following advantages. (1) The need for coupling liquids is eliminated due to the low-loss solid dielectric material incorporated into the antenna structure. This not only simplifies the imaging setup but also eliminates the additional power loss due to the coupling liquids. (2) The small sensor aperture leads to enhanced spatial resolution in the images. (3) The UWB operation of the antenna allows for aperture raster scanning in the UWB frequency range. Since both the new sensor and the new holography algorithm proposed in [38] have a significant potential to be used in breast cancer detection, a new techniques to exploit both advantages is required. The first problem is that the mentioned holography algorithm is based on a point source receiver and transmitter. Thus, the aperture size of the antenna cannot be neglected in interpreting the received signals. A method for reducing the integration effect of the antenna aperture is required.

1.3 CONTRIBUTIONS

First, a vectorial form for 3D near-field holography is proposed [44] which is an improvement over the holography algorithm proposed in [38]. Second, a simple and fast post-processing algorithm based on the principle of blind de-convolution is proposed for removing the integration effect of the antenna aperture [45]. This allows for the data collected by the antennas to be used for 3D holography reconstruction. The blind deconvolution algorithm is a well-known algorithm in signal processing [46][49] and our contribution here is its adaptation to microwave data processing.

1.4 ACCELERATED SPACE MAPPING WITH ADJOINT SENSITIVITIES

Microwave circuits and systems are vital for modern technology. They cover a vast range of applications from a small device like a cell phone to large scientific projects such as space discovery. The development of computer-aided design (CAD) tools and optimization methods has led to significant advances in microwave design and modeling capabilities, with advantages such as lower development costs and shortened design cycles [50][51].

Microwave engineering has its beginning in the last century. In the early days, the design of microwave circuits would often require the rather tedious and expensive process of "cut and try": measurements and subsequent amendments on numerous prototypes [52]. Modern CAD tools for microwave circuit design [53][55] are developed to overcome these difficulties. Nowadays, as powerful computers become available, such CAD tools are widely used. Together with the CAD tools, the search for efficient optimization methods intensifies. Traditional optimization methods [56]-[58] directly utilize simulated responses and possibly available derivatives to guide the design toward the required specifications. However, the higher the fidelity of the simulation, the more expensive is direct optimization. Traditional electromagnetic (EM) optimization is still a formidable computational task.

Space mapping (SM) [59][60], first proposed by Bandler *et al*. in 1994, aims at solving this computational problem. It allows for the efficient optimization of expensive and complex models referred to as ”fine” models by means of iterative optimization. The major burden of the iterative optimization is shifted onto the so called “coarse” model which is not accurate but is much cheaper computationally. SM is a widely recognized contribution to engineering design for its distinguishing feature of combing the efficiency of empirical models with the accuracy of EM simulations. It has been extensively applied to modeling and design of engineering devices and systems [61] especially in the microwave area.

1.5 MOTIVATION

The sensitivities of the *S*-parameters are now available in some commercial software packages through self-adjoint sensitivity analysis [62] (SASA). These sensitivities significantly decrease the optimization time. On the other hand space mapping is a well known approach which also decreases the optimization burden. An approach which exploits both SASA and SM is promising.

1.6 CONTRIBUTIONS

In this thesis an algorithm which exploits the advantages of both response sensitivities and space mapping is proposed [63]. The relation between the mapping matrix between the fine and coarse model spaces and the sensitivities of the coarse and fine models was derived in [63]. Due to the lack of response sensitivities in commercial software, a possible algorithm to use this relation has not been developed till now. In this thesis, an algorithm which uses response sensitivities with respect to the design parameters and the implicit parameters is proposed. A useful design framework based on the proposed algorithm is also presented [65].

1.7 OUTLINE OF THESIS

In chapter 2, an improved holographic microwave imaging techniques is proposed to reconstruct an image of the targets. In this algorithm, both co-pol and cross-pol data are used which leads to better image quality. These techniques are based on the Fourier analysis of the data recorded by two antennas scanning together two separate rectangular parallel apertures on both sides of a target. No assumptions are made about the incident field, which can be derived by either simulation or measurement. Both the back-scattered and forward-scattered signals can be used to reconstruct the image of the target.

In chapter 3, a novel application of blind deconvolution is presented to improve the quality of image obtained through microwave raster scanning.

In chapter 4, a procedure for accelerating the space mapping optimization process is presented. Exploiting both fine- and surrogate-model sensitivity information, a good mapping between the two model spaces is efficiently obtained. This results in a significant speed-up over direct gradient-based optimization of the original fine model and enhanced performance compared with other space-mapping approaches. Our approach utilizes commercially available software with adjoint-sensitivity analysis capabilities.

REFERENCES

[1] P. Neittaanmaki, M. Rudnicki, and A. Savini, *Inverse Problems and Optimal Design in Electricity and Magnetism*. Clarendon Press, Oxford, 1996.

[2] D. M. Parkin, F. Bray, J. F. And, and P. Pisani, “Global cancer statistics, 2002,” *CA: A Cancer J. Clinicians*, vol. 55, pp. 74–108, Mar. 2005.

[3] C. H. Jones, “Methods of breast imaging,” *Phys. Med. Biol.*, vol. 27, pp. 463–499, Apr. 1982.

[4] M. Säbel and H. Aichinger, “Recent developments in breast imaging,” *Phys. Med. Biol.*, vol. 41, pp. 315–368, Mar. 1996.

[5] P. T. Huynh, A. M. Jarolimek, and S. Daye, “The false-negative mammogram,” *Radiographics*, vol. 18, pp. 1137–1154, Sep. 1998.

[6] E. C. Fear, S. C. Hagness, P. M. Meaney, M. Okoniewski, and M. A. Stuchly, “Enhancing breast tumor detection with near-field imaging,” *IEEE Microwave Magazine*, vol. 3, no. 1, pp. 48−56, Mar. 2002.

[7] J. H. Jacobi, L. E. Larsen, and C. T. Hast, “Water-immersed microwave antennas and their application to microwave interrogation of biological targets,” *IEEE Trans. Microwave Theory Tech.*, vol. MTT-27, no. 1, pp. 70–78, Jan. 1979.

[8] L. E. Larsen and J. H. Jacobi, “Microwave scattering parameter imagery of an isolated canine kidney,” *Med. Phys.*, vol. 6, pp. 394–403, 1979.

[9] A. J. Devaney, “Reconstructive tomography with diffracting wave-fields,” *Inv. Problems*, vol. 2, no. 2, pp. 161–183, May 1986.

[10] R. Aitmehdi, A. P. Anderson, S. Sali, and M. Ferrando, “The determination of dielectric loss tangent by microwave phase tomography,” *Inv. Problems*, vol. 4, no. 2, pp. 333–345, May 1988.

[11] M. Slaney, A. C. Kak, and L. E. Larsen, “Limitations of imaging with first order diffraction tomography,” *IEEE Trans. Microwave Theory Tech.*, vol. 32, no. 8, pp. 860–873, Aug. 1984.

[12] J. C. Bolomey, C. Pichot, and G. Gaboriaud, “Planar microwave camera for biomedical applications: Critical and prospective analysis of reconstruction algorithms,” *Radio Sci.*, vol. 26, no. 2, pp. 541–549, Apr. 1991.

[13] A. Fhager and M. Persson, “Comparison of two image reconstruction algorithms for microwave tomography,” *Radio Sci.*, vol. 40, no. 3, Jun. 2005.

[14] A. Abubakar, P. M. van den Berg, and J. J. Mallorqui, “Imaging of biomedical data using a multiplicative regularized contrast source inversion method,” *IEEE Trans. Microwave Theory Tech.*, vol. 59, no. 7, pp. 1761–1771, Jul. 2002.

[15] R. E. Kleinman and P. M. van den Berg, "A modified gradient method for two-dimensional problems in tomography," *J. Comput. Appl. Math.*, vol. 42, no. 1, pp. 17–35, Sep. 1992.

[16] W. C. Chew and Y. M.Wang, "Reconstruction of two-dimensional permittivity distribution using the distorted born iterative method," *IEEE Trans. Med. Imag.*, vol. 9, no. 2, pp. 218–225, Jun. 1990.

[17] A. E. Bulyshev, A. E. Souvorov, S. Y. Semenov, V. G. Posukh, and Y. E. Sizov, "Three-dimensional vector microwave tomography: Theory and computational experiments," *Inv. Problems*, vol. 20, no. 4, pp. 1239–1259, Aug. 2004.

[18] A. Abubakar and P. M. van den Berg, "Iterative forward and inverse algorithms based on domain integral equations for three-dimensional electric and magnetic objects," *J. Comput. Phys.*, vol. 195, no. 1, pp. 236–262, Mar. 2004.

[19] Z. Q. Zhang and Q. H. Liu, "Three-dimensional nonlinear image reconstruction for microwave biomedical imaging," *IEEE Trans. Biomed. Eng.*, vol. 51, no. 3, pp. 544–548, Mar. 2004.

[20] Q. Fang, P. M. Meaney, S. D. Geimer, A. V. Streltsov, and K. D. Paulsen, "Microwave image reconstruction from 3D fields coupled to 2D parameter estimation," *IEEE Trans. Med. Imag.*, vol. 23, no. 4, pp. 475–484, Apr. 2004.

[21] S. Y. Semenov, A. E. Bulyshev, A. Abubakar, V. G. Posukh, Y. E. Sizov, A. E. Souvorov, P. M. van den Berg, and T. C. Williams, "Microwave-tomographic imaging of high dielectric-contrast objects using different image-reconstruction approaches," *IEEE Trans. Microwave Theory Tech.*, vol. 53, no. 7, pp. 2284–2295, Jul. 2005.

[22] T. Isernia, V. Pascazio, and R. Pierri, "On the local minima in a tomographic imaging technique," *IEEE Trans. Geosci. Remote Sens.*, vol. 39, no. 7, pp. 1596–1607, Jul. 2001.

[23] R. Benjamin, "Synthetic, post-reception focusing in near-field radar," *Proc. EUREL Int. Conf. on the Detection of Abandoned Land Mines: A Humanitarian Imperative Seeking a Tech. Solution*, pp. 133–137, Oct 1996.

[24] R. Benjamin, "Detecting reflective object in reflective medium," U.K. GB 2313969, Dec. 1997.

[25] S. C. Hagness, A. Taflove, and J. E. Bridges, "Two-dimensional FDTD analysis of a pulsed microwave confocal system for breast cancer detection: Fixed-focus and antenna-array sensors," *IEEE Trans. Biomed. Eng.*, vol. 45, pp. 1470–1479, Dec. 1998.

[26] E. C. Fear and M. A. Stuchly, "Microwave system for breast tumor detection," *IEEE Microwave Wireless Compon. Lett.*, vol. 9, pp. 470–472, Nov. 1999.

[27] L. Xu, S. K. Davis, S. C. Hagness, D. W. van der Weide, and B. D. Van Veen, "Microwave imaging via space-time beamforming: Experimental investigation of tumor detection in multilayer breast phantoms," *IEEE Trans. Microwave Theory Tech.*, vol. 52, pt. Part 2, pp. 1856–1865, Aug. 2004.

[28] E. J. Bond, L. Xu, S. C. Hagness, and B. D. Van Veen, "Microwave imaging via space-time beamforming for early detection of breast cancer," in *Proc. IEEE Int.*

Conf. on Acoust., Speech, and Signal Process. (ICASSP ’02), vol. 3, pp. 2909–2912, May 2002.

[29] Y. Xie, B. Guo, L. Xu, J. Li, and P. Stoica, “Multi-static adaptive microwave imaging for early breast cancer detection,” in *Proc. 39th Asilomar Conf. on Signals, Syst. and Comput.*, pp. 285–289, Nov. 2005.

[30] M. Klemm, I. J. Craddock, J. A. Leendertz, A. Preece, and R. Benjamin “Radar-based breast cancer detection using a hemispherical antenna array-experimental results” *IEEE Trans. Antennas and Propag.*, vol. 57, no. 6, pp. 1692–1704, Jun. 2009.

[31] E. C. Fear, J. Sill, and M. A. Stuchly, “Experimental feasibility study of confocal microwave imaging for breast tumor detection,” *IEEE Trans. Microw. Theory Tech.*, vol. 51, pp. 887–892, Mar. 2003.

[32] J. M. Sill and E. C. Fear, “Tissue sensing adaptive radar for breast cancer detection—experimental investigation of simple tumor models,” *IEEE Trans. Microwave Theory Tech.*, vol. 53, pp. 3312–3319, Nov. 2005.

[33] D. M. Sheen, D. L. McMakin, and T. E. Hall, “Three-dimensional millimeter-wave imaging for concealed weapon detection,” *IEEE Trans. Microw. Theory Tech.*, vol. 49, no. 9, pp. 1581−1592, Sep. 2001.

[34] D. M. Sheen, D. L. McMakin, and T. E. Hall, “Near field imaging at microwave and millimeter wave frequencies,” *IEEE/MTT-S Int. Microwave Symp.*, pp. 1693−1696, Jun. 2007.

[35] M. Ravan, R. K. Amineh, and N. K. Nikolova, “Two-dimensional near-field microwave holography,” *Inverse Problems*, vol. 26, no. 5, May. 2010.

[36] M. Ravan, R. K. Amineh, and N. K. Nikolova, “Microwave holography for near-field imaging,” *IEEE AP-S/URSI Int. Symp. on Antennas and Propagation*, July 2010.

[37] M. Ravan, R. K. Amineh, and N. K. Nikolova, “Near-field microwave holographic imaging: target localization and resolution study,” *XX URSI Comm. B Int. Symp. on Electromagnetic Theory* (EMT-S 2010), Aug. 2010.

[38] R. K. Amineh, M. Ravan, A. Khalatpour, and N. K. Nikolova, “Three-dimensional near-field microwave holography using reflected and transmitted signals,” accepted for publication in *IEEE Trans. Antennas Propag.*

[39] N. H. Farhat and W. R. Guard, “Millimeter wave holographic imaging of concealed weapons,” *Proc. of the IEEE*, vol. 59, pp. 1383−1384, 1971.

[40] D. Slater, *Near-Field Antenna Measurements*, Artech House, Boston, 1991.

[41] M. Elsdon, M. Leach, S. Skobelev, and D. Smith, “Microwave holographic imaging of breast cancer,” *IEEE Int. Symp. on Microwave, Antenna, Propag., and EMC Tech. For Wireless Commun.*, pp. 966−969, Aug. 2007.

[42] J. T. Case, I. Robbins, S. Kharkovsky, F. Hepburn, and R. Zoughi, “Microwave and millimeter wave imaging of the space shuttle external fuel tank spray on foam insulation (SOFL) using synthetic aperture focusing techniques,” (SAFT) *Review of Quantitative Nondestructive Evaluation*, vol. 25, pp. 1546−1553, Aug. 2006.

[43] R. K. Amineh, M. Ravan, A. Trehan, and N. K. Nikolova, "Near-field microwave imaging based on aperture raster scanning with TEM horn antennas," *IEEE Trans. Antennas Propag.*, vol. 59, no. 3, pp. 928−940, Mar. 2011.

[44] R. K. Amineh, A. Khalatpour, and N. K. Nikolova, "Three-dimensional near-field microwave holography using co-polarized and cross-polarized data," submitted to *IEEE Antennas and Wireless Propagation Letters.*

[45] A. Khalatpour, R. K. Amineh, and N. K. Nikolova, "Image quality enhancement in the microwave raster scanning method accepted for the presentation at the *IEEE MTT-S Int. Microwave Symposium* 2011, June 2011

[46] D. Kundur and D. Hatzinakos, "Blind image deconvolution," *IEEE Signal Proc. Mag.*, vol. 13, no. 3, pp. 43–64, May. 1996.

[47] G. R. Ayers and J. C. Dainty, "Iterative blind deconvolution method and its applications," *Optics Lett.*, vol. 13, no. 7, pp. 547–549, July. 1988.

[48] B. L. K. Davey, R. G. Lane, and R. H. T. Bates, "Blind deconvolution of noisy complex-valued image," *Optics Comm.*, vol. 69, no. 7, pp. 353–356, Jan. 1989.

[49] B. C. McCallum, "Blind deconvolution by simulated annealing," *Optics Comm.*, vol. 75, no. 2, pp. 101–105, Feb. 1990.

[50] J. W. Bandler, "Optimization methods for computer-aided design," *IEEE Trans. Microwave Theory Tech.*, vol. 17, no. 8, pp. 533–525, Aug. 1969.

[51] J. W. Bandler, "Computer optimization of microwave circuits," *Proc. European Microwave Conf.*, Stockholm, Sweden, pp. B8/S: 1S: 8, Aug. 1971.

[52] M. B. Steer, J. W. Bandler, and C. M. Snowden, "Computed-aided design of RF and microwave circuits and systems," *IEEE Trans. Microwave Theory Tech.*, vol. 50, no. 3, pp. 996–1005, Mar. 2002.

[53] D. M. Pozar, *Microwave Engineering*, Wiley, Hoboken, NJ, 2005. D.G.

[54] *Ansoft Corporation*, http://www.ansoft.com.

[55] Agilent ADS 2005A, *Agilent Technologies*, 1400 Fountain grove Parkway, Santa Rosa, CA 95403–1799, USA.

[56] J. W. Bandler and S. H. Chen, "Circuit optimization: the state of the art," *IEEE Trans. Microwave Theory Tech.*, vol. 36, no. 2, pp. 424–443, Feb. 1998.

[57] J. W. Bandler, W. Kellermann, and K. Madsen, "A superlinearly convergent minimax algorithm for microwave circuit design," *IEEE Trans. Microwave Theory Tech.*, vol. *MTT*-33, no. 12, pp. 1519–1530, Dec. 1985.

[58] J. W. Bandler, S. H. Chen, S. Daijavad, and K. Madsen, "Efficient optimization with integrated gradient approximations," *IEEE Trans. Microwave Theory Tech.*, vol. 36, no. 2, pp. 444–455, Feb. 1988.

[59] J. W. Bandler, R. M. Biernacki, S. H. Chen, P. A. Grobelny, and R.H. Hemmers, "Space mapping technique for electromagnetic optimization," *IEEE Trans. Microwave Theory Tech.*, vol. 42, no. 12, pp. 2536–2544, Dec. 1994.

[60] J. W. Bandler, Q. S. Cheng, S. A. Dakroury, A. S. Mohamed, M. H. Bakr, K. Madsen, and J. Søndergaard, "Space mapping: the state of the art," *IEEE Trans. Microwave Theory Tech.*, vol. 52, no. 1, pp. 337–361, Jan. 2004.

[61] S. Koziel and J. W. Bandler, *International Journal of Numerical Modeling*, vol. 23, no. 6, pp. 425–446, Nov 2010.

[62] N. K. Nikolova, J. Zhu, D. Li, M. H. Bakr, and J. W. Bandler, “Sensitivity analysis of network parameters with electromagnetic frequency domain simulators,” *IEEE Trans. Microwave Theory Tech*., vol. 54, no. 2, pp. 670–681, Feb. 2006.

[63] A. Khalatpour, R. K. Amineh, Q. S. Cheng, M. H. Bakr, N. K. Nikolova, and J. W. Bandler, “Accelerating space mapping optimization with adjoint sensitivities,” *IEEE Microw. Wireless Compon Lett.,* vol. 21, no. 6, pp. 280–282, June 2011.

[64] M. H. Bakr, J. W. Bandler, N. Georgieva, and K. Madsen, “A hybrid aggressive space-mapping algorithm for EM optimization,” *IEEE Trans. Microwave Theory Tech*., vol. 47, no. 12, pp. 2440–2449, Dec. 1999.

[65] A. Khalatpour, R. K. Amineh, Q. S. Cheng, N. K. Nikolova, and J. W. Bandler, “Adjoint-accelerated design framework for novel materials in microwave applications,” accepted for the presentation at the 41st *European Microwave Conference*, Oct. 2011.

CHAPTER 2

THREE-DIMENSIONAL NEAR-FIELD MICROWAVE HOLOGRAPHY USING CO-POLARIZED AND CROSS-POLARIZED DATA

2.1 INTRODUCTION

Various methods have been proposed for microwave imaging. We described common optimization-based and radar-based techniques proposed so far for breast imaging in chapter 1. We also described the challenges in microwave imaging which have prevented the realization of reliable clinical imaging setups so far.

A microwave holographic imaging technique has been proposed in Pacific Northwest National Laboratory [1][2] which relies on the measurement of the magnitude and phase of the wave scattered from the imaged target on a rectangular aperture. Knowledge of the magnitude and phase across an aperture allows Fourier-transform (FT) based reconstruction of the target's reflectivity. This technique has been used to form high-resolution two-dimensional (2D) or three-dimensional (3D) images. In this method, a transmitter antenna and a receiver antenna move together on one side of the target to scan a rectangular planar aperture.

An extension has been made to the holographic image reconstruction developed in [1][2] to include not only back-scattered but also forward-scattered signals for 2D and 3D imaging [3]-[6]. In this development, no assumptions are made about the incident field such as those based on plane-wave representations. The incident field can be given in a numerical form as in the case when it is derived through electromagnetic simulation or it can be given through measurement. This is especially important in near-field imaging where the target is close to the antenna and the spherical plane-wave assumptions for the illuminating wave are not valid. In the 2D technique, the *S*-parameters collected at a single frequency are then processed to first localize the target in the range direction and then reconstruct a 2D image of the target. In the 3D technique, the *S*-parameters collected at several frequencies are processed to reconstruct a 3D target region slice by slice.

In [1][2], the solution is provided based on a simplifying assumption leading to a scalar wave equation. For example, using two co-polarized dipole antennas, which generate and sample only the co-polarized components of the incident and scattered fields, is the case considered in [5][6]. However, the algorithm in [5][6] can be extended to handle both co-polarized and cross-polarized data.

Here, a full vector 3D holography for near-field imaging is presented [7]. It allows for the combined use of the data collected from co-polarized and cross-polarized measurements. We demonstrate that this leads to significantly improved reconstructed image. The reconstruction results when using co-polarized data only, cross-polarized data only, and combined co-polarized and cross-polarized data are presented for X-shaped and square-shaped targets.

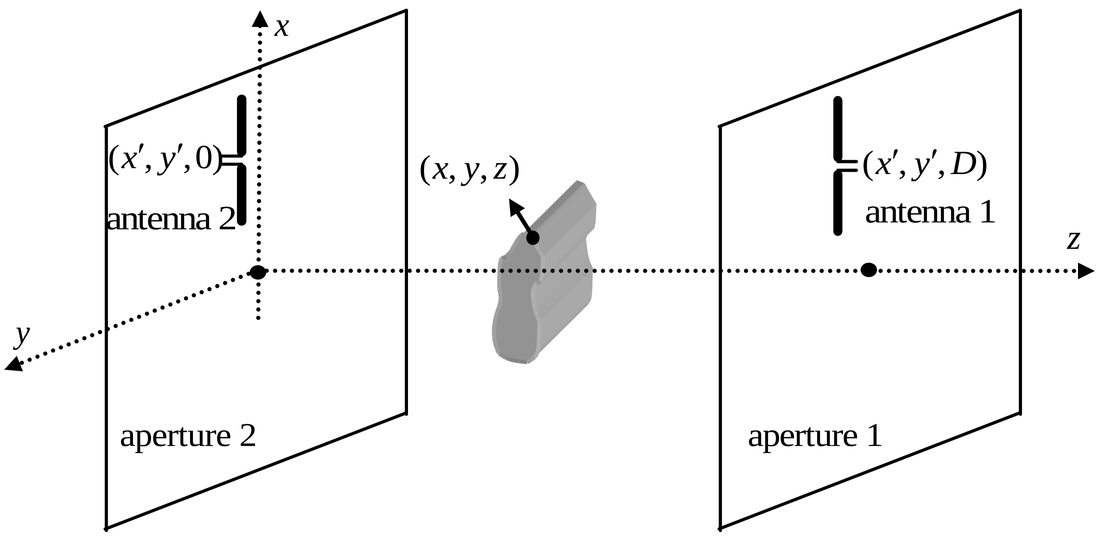

Fig. 1. 3D microwave holography setup with the two dipoles being co-polarized [7].

2.2 THEORY

The microwave holography setup considered here employs planar raster scanning. It consists of two dipole antennas and a target in between as shown in Fig. 1. The formulation of the scattered field when using the linear Born approximation is [8]

$$\boldsymbol{E}^{\mathrm{sc}}(\boldsymbol{r}) \approx \iiint_V \underline{\underline{\boldsymbol{G}}}(\boldsymbol{r},\boldsymbol{r}') \cdot \boldsymbol{E}^{\mathrm{inc}}(\boldsymbol{r}')[k_s^2(\boldsymbol{r}') - k_b^2]d\boldsymbol{r}' \tag{1}$$

where $\boldsymbol{E}^{\mathrm{sc}}$ is the scatted field observed at position $\boldsymbol{r}$, $\underline{\underline{\boldsymbol{G}}}(\boldsymbol{r},\boldsymbol{r}')$ is Green's dyadic function, $\boldsymbol{E}^{\mathrm{inc}}$ is the incident field at the position of $\boldsymbol{r}'$ of the scatterer, and k_s and k_b are the wave numbers of the scatterer and the background medium, respectively. The condition for applying first-order Born approximation is that the radius a of a sphere enclosing the target satisfy [9]

$$(n-1)a < \frac{\lambda_{\min}}{4} \tag{2}$$

in which n is the index of refraction of the target with respect to the background.

In contrast to the work in [5], where only the co-polarized component (*x*-component) of the incident and scattered fields were considered, here we provide a full vector holographic theory. This theory allows for the development of reconstruction algorithms employing both co-polarized and cross-polarized measured data.

As shown in Fig. 1, the antennas perform 2D scan while moving together on two separate parallel planes positioned at $z=0$ and $z=D$. Assume that at any measurement frequency f_l ($l=1,2,\dots,N_f$) we know the incident field $\boldsymbol{E}^{\text{inc}}(0,0,0;x,y,z;f_l)$ at any point (x,y,z) in the inspected volume when the transmitting antenna is at $(0,0,0)$. In addition, all scalar components of Green's tensor function $G_i^j(x,y,z;0,0,D;f_l)$ (i, j = x, y, or z) are known for an *i*-polarized point source at (x,y,z) and E_j^{sc} measured at $(0,0,D)$. This information can be obtained via simulations as explained in [5]. For brevity, we set

$$\boldsymbol{E}^{\text{inc}}(x,y,z,f_l)\equiv\boldsymbol{E}^{\text{inc}}(0,0,0;x,y,z;f_l) \tag{3}$$

$$\underline{\underline{\boldsymbol{G}}}(x,y,z,f_l)\equiv\underline{\underline{\boldsymbol{G}}}(x,y,z;0,0,D;f_l)\,. \tag{4}$$

Let the signal $E_j^{\text{sc}}(x',y',D,f_l)$ be the scattered wave received at (x',y',D). This implies that the transmitting antenna is at $(x',y',0)$ since it moves together with the receiving antenna. The incident field and Green's functions for the case where the antenna pair is at (x',y') can be obtained from those in (3) and (4) by a simple translation if the background medium is uniform:

$$\boldsymbol{E}^{\text{inc}}(x',y',0;x,y,z;f_l)=\boldsymbol{E}^{\text{inc}}(x-x',y-y',z,f_l) \tag{5}$$

$$\underline{\underline{\boldsymbol{G}}}(x', y', 0; x, y, z; f_l) = \underline{\underline{\boldsymbol{G}}}(x - x', y - y', z, f_l)\,. \tag{6}$$

Then, each j-component ($j = x$, y, or z) of the scattered field is written as [7]

$$E_j^{\mathrm{sc}}(x', y', D, f_l) = \iiint\limits_{z\,y\,x} f(x, y, z, f_l) \sum_{m=1}^{3} g_m(x' - x, y' - y, z, f_l) dxdydz \tag{7}$$

where

$$f(x, y, z, f_l) = k_s^2(x, y, z, f_l) - k_b^2(f_l), \tag{8}$$

$$g_1(x, y, z, f_l) = E_x^{\mathrm{inc}}(-x, -y, z, f_l) G_x^j(-x, -y, z, f_l), \tag{9}$$

$$g_2(x, y, z, f_l) = E_y^{\mathrm{inc}}(-x, -y, z, f_l) G_y^j(-x, -y, z, f_l). \tag{10}$$

$$g_3(x, y, z, f_l) = E_z^{\mathrm{inc}}(-x, -y, z, f_l) G_z^j(-x, -y, z, f_l). \tag{11}$$

We refer to $f(x, y, z, f_l)$ as the contrast function. In [5], we have described how to deal with dispersive mediums. The same approach can be employed here as well. For now, for simplicity we assume that the contrast function is frequency-independent, i.e., $f(x, y, z) \equiv f(x, y, z, f_l)$, and isotropic, i.e., polarization independent.

Notice that in (7), the integral over x and y can be interpreted as a 2D convolution integral. Thus, the 2D FT of $E_j^{\mathrm{sc}}(x', y', D, f_l)$ is written as

$$E_j^{\mathrm{sc}}(k_x, k_y, D, f_l) = \int\limits_z F(k_x, k_y, z) \sum_{m=1}^{3} G_m(k_x, k_y, z, f_l) dz, \quad j = x, y, z \tag{12}$$

where $F(k_x, k_y, z)$ and $G_m(k_x, k_y, z, f_l)$ are the 2-D FTs of $f(x, y, z)$ and $g_m(x, y, z, f_l)$, respectively; and k_x and k_y are the Fourier variables with respect to x and y, respectively.

To reconstruct the contrast function, we first approximate the integral in (12) by a discrete sum with respect to z for the N_z reconstruction planes

$$E_j^{\mathrm{sc}}(k_x,k_y,D,f_l)=\sum_{n=1}^{N_z}F(k_x,k_y,z_n)\sum_{m=1}^{3}G_m(k_x,k_y,z_n,f_l)\Delta z \tag{13}$$

where Δz is the distance between two neighboring reconstruction planes. By expanding (13), a set of linear equation is obtained, which can be solved for $F(k_x,k_y,z_n)$.

For the setup shown in Fig. 1, there could be four antenna configurations when performing the raster scan: (1) antenna 1 and antenna 2 both being *x*-polarized (X-X case); (2) antenna 1 being *x*-polarized while antenna 2 being *y*-polarized (X-Y case); (3) antenna 1 being *y*-polarized while antenna 2 being *x*-polarized (Y-X case); and (4) antenna 1 and antenna 2 both being *y*-polarized (Y-Y case).

Four complex *S*-parameters are acquired at the two antenna terminals for each of the four polarization cases listed above. These four *S*-parameters constitute four separate scattered signals at those in (1) (two reflection and two transmission coefficients). Thus, by performing wideband *S*-parameter measurements at N_f frequencies, writing (13) for each polarization case leads to $4\times N_f$ equations at each spatial-frequency pair (k_x,k_y). The system of equations for all four polarization cases are combined to form a system of $12\times N_f$ equations, which must be solved for $F(k_x,k_y,z_n)$, n = 1,2,.., N_z. Here, we assume that by rotation of the setup the reflection coefficients do not change, so we will have $12\times N_f$ equations instead of $16\times N_f$ equations.

The constructed system of equations is solved in the least-square sense to find $F(k_x,k_y,z_n)$, $n=1,2,\ldots,N_z$, at each spatial frequency pair (k_x,k_y). Then, inverse 2D FT is applied to $F(k_x,k_y,z_n)$, to reconstruct a 2D slice of the function $f(x,y,z_n)$ at each

$z = z_n$ plane. Then, the normalized modulus of $f(x, y, z_n)$, $|f(x, y, z_n)|/M$, where M is the maximum of $|f(x, y, z_n)|$ for all z_n, is plotted versus x and y to obtain a 2D image of the target at each $z = z_n$ plane, $n = 1, 2, \ldots, N_z$. By putting together all 2D slice images, a 3D image of the target is obtained.

2.3 VERIFICATION

The reconstruction results when measuring the *S*-parameters for two co-polarized (*x*-polarized) dipoles have been thoroughly studied in [5]. Here, we show the improvement when adding the data obtained from cross-polarized dipole measurements (one dipole is *x*-polarized while the other one is *y*-polarized). We consider only symmetric targets. Thus, it suffices to perform only two sets of measurements for co- and cross-polarized configurations, X–X and X–Y measurements, instead of four sets. By measuring wideband *S*-parameters for these configurations, a system of $7 \times N_f$ equations is constructed at each (k_x, k_y) ($4 \times N_f$ equations from the X–X measurement and $3 \times N_f$ additional equations from the X–Y measurement).

In [5], we employed *x*-polarized dipoles and only the *x*-component of the incident field was considered in the reconstruction planes. Here, not only we use co- and cross-polarized dipole measurements but also we consider both the co- and cross-polarized components of the incident field in the reconstruction planes. To investigate the improvement in the image reconstruction results, two $\lambda/2$ (at 6.5 GHz) dipole antennas with targets in between are simulated in FEKO Suite 6 [10] as illustrated in Fig. 2.

In both examples, the background medium is lossy with ε_r = 16 and σ = 0.5 S/m at all frequencies. As shown in Fig. 2(a), in the first example, the target is an X-shape object composed of two arms of length 20 mm and a square cross-section with a side of 2 mm. This target is placed at z = 30 mm while its arms are positioned along the x- and y-axes. As shown in Fig. 2(b), in the second example, the target is a square-shape object composed of four arms parallel to the x- and y-axes. Each arm has a length of 20 mm with a square cross-section of side 2 mm. This target is also placed at z = 30 mm. The constitutive parameters of both targets are ε_r = 32 and σ = 1 S/m at all frequencies.

The antennas perform 2D scans by moving together on the two parallel aperture planes and collecting wideband (in the frequency range from 3 to 10 GHz) S-parameters at each position. The apertures have a size of 60 mm $\times$ 60 mm with their centers being on the z axis. They are located at z = 50 mm and z = 0.

The sampling rates in the spatial and frequency domains are chosen such that the sampling criteria in [5] are fulfilled. The spatial and frequency sampling rates are 1.5 mm and 0.25 GHz, respectively. This provides measurements for each S-parameter at 1681 positions and at 29 frequencies for each position. Also, from [5], the computed cross-range and range resolutions are approximately 3.5 mm and 6 mm, respectively. Complete information of both depth and cross resolution of the algorithm is described in[6].

In the data acquisition process when the target is present, a 2D scan is performed with both dipoles being x-polarized. Then a second 2D scan is performed when dipole 1 is y-polarized and dipole 2 is x-polarized. The S-parameters s_{pq}^{t} (p,q = 1,2) for the two antennas are acquired in the presence of the target and recorded for every (x', y') position of the antenna pair. The numerical noise in the acquired data is estimated through the numerical convergence error of the *S*-parameters which is 0.02.

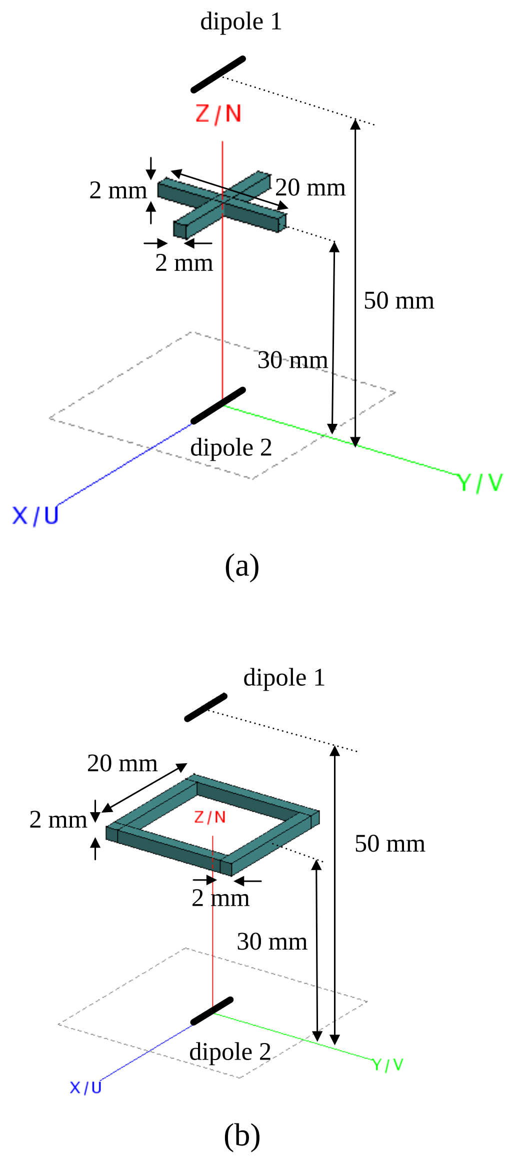

Fig. 2. Dielectric targets with $\varepsilon_r = 32$ and $\sigma = 1$ S/m in a background medium with $\varepsilon_r = 16$ and $\sigma = 0.5$ S/m scanned by two $\lambda/2$ (at 6.5 GHz) (*x*- or *y*- polarized) dipoles (only *x*-polarized antennas are shown): Dipole 1 is scanning the $z = 50$ mm plane while dipole 2 is scanning the $z = 0$ mm plane. The simulated *S*-parameters are recorded in the frequency

band from 3 GHz to 10 GHz with a step of 250 MHz. (a) Cross-shaped target. (b) Square-shaped target.

The proposed holography technique is applied to the calibrated *S*-parameters. To perform calibration, the same scans are performed without the target to obtain the background *S*-parameters s_{pq}^{b} (*p*,*q* = 1,2). Then, the calibrated *S*-parameters are calculated as

$$s_{pq}^{\mathrm{cal}}(x',y') = s_{pq}^{\mathrm{t}}(x',y') - s_{pq}^{\mathrm{b}}. \tag{14}$$

Here, due to the uniform background, the background simulations need to be performed only once in a sample (x',y') position since in all other positions they are the same. For both antenna polarizations, the *x*- and *y*- components of the simulated incident field and Green's function are recorded in the reconstruction planes at $z = z_n$, $n = 1,2,\ldots,N_z$. These planes are of size 80 mm $\times$ 80 mm. By replacing E^{sc} in (7) with the corresponding s_{pq}^{cal}, a system of equations is built. The systems of equations for the two polarization cases are then combined and solved as described in section 2.2.

Fig. 3 and Fig. 4 show the the reconstructed images in the range positions of 6 mm to 48 mm with a step of 6 mm when using only the cross-polarized data. It is observed that although the shape of the targets can be distinguished in the image at *z* = 30 mm, the arms parallel to the *x*-axis appear with higher contrast.

Fig. 5 and Fig. 6 show the reconstructed images in the same range positions when using only the co-polarized data. In this case, the targets' arms parallel to the *y*-axis appear with higher contrast at *z* = 30 mm.

Similarly, Fig. 5 and Fig. 8 show the reconstructed images in the same range positions when using both the co- and cross-polarized data. As observed in the images, the arms parallel to the *x*-axis and those parallel to the *y*-axis appear with almost similar contrast in the reconstructed images at z = 30 mm. This confirms the improvement in the image reconstruction quality when using both co- and cross-polarized data.

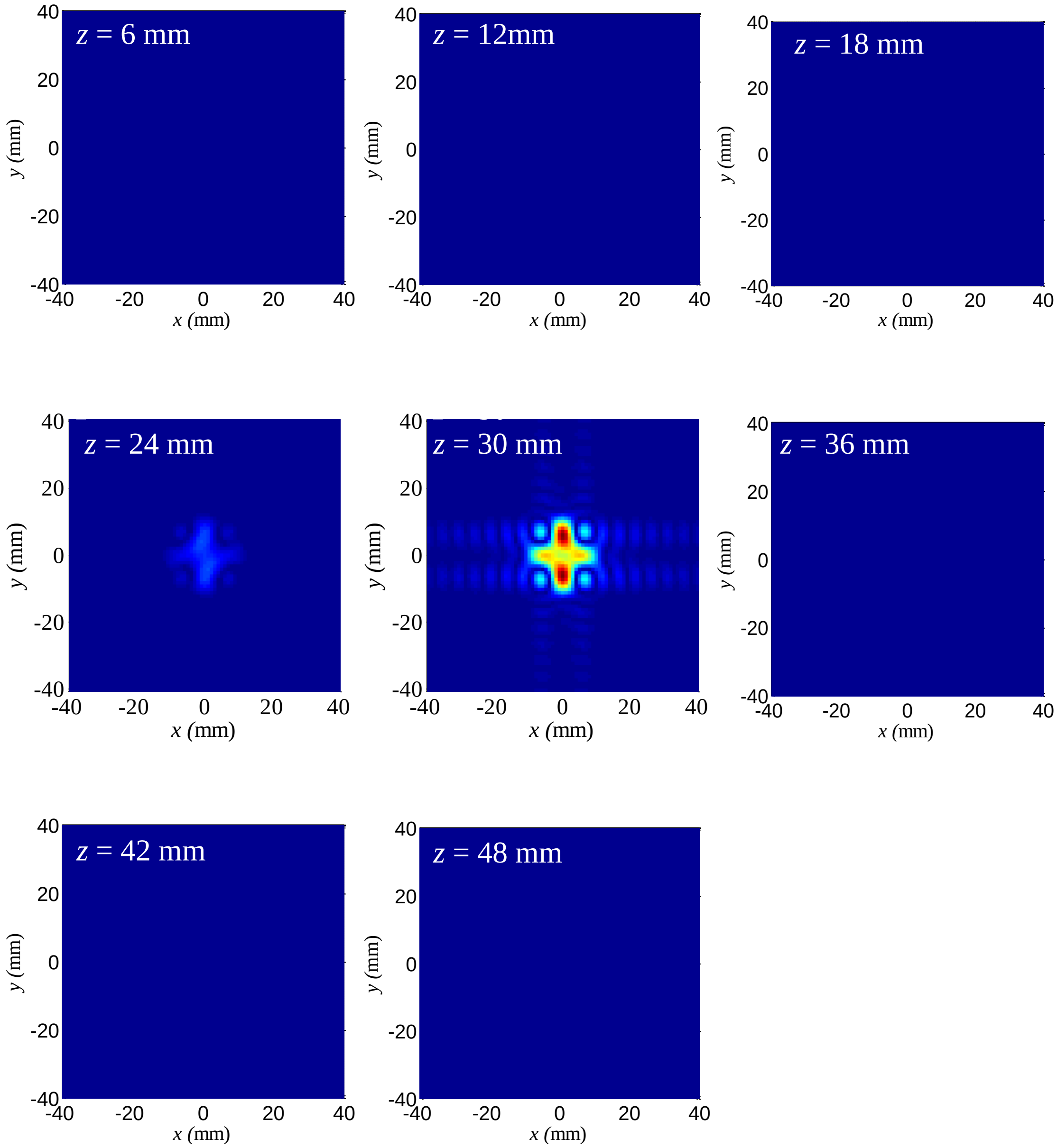

Fig. 3. Reconstructed images for the dielectric target in Fig. 2(a) using co- polarized data only.

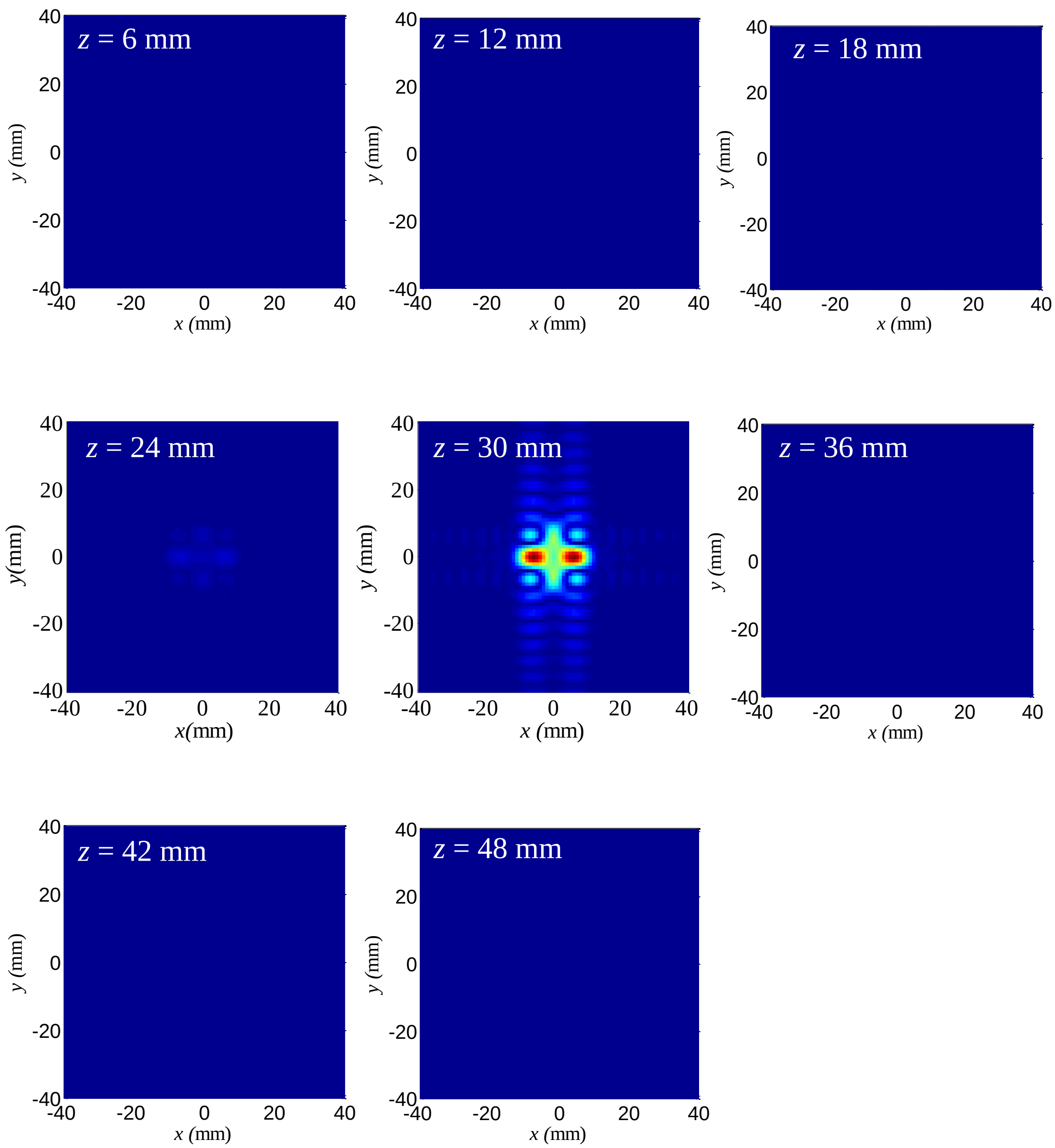

Fig. 4. Reconstructed images for the dielectric target in Fig. 2(a) using cross-polarized data only.

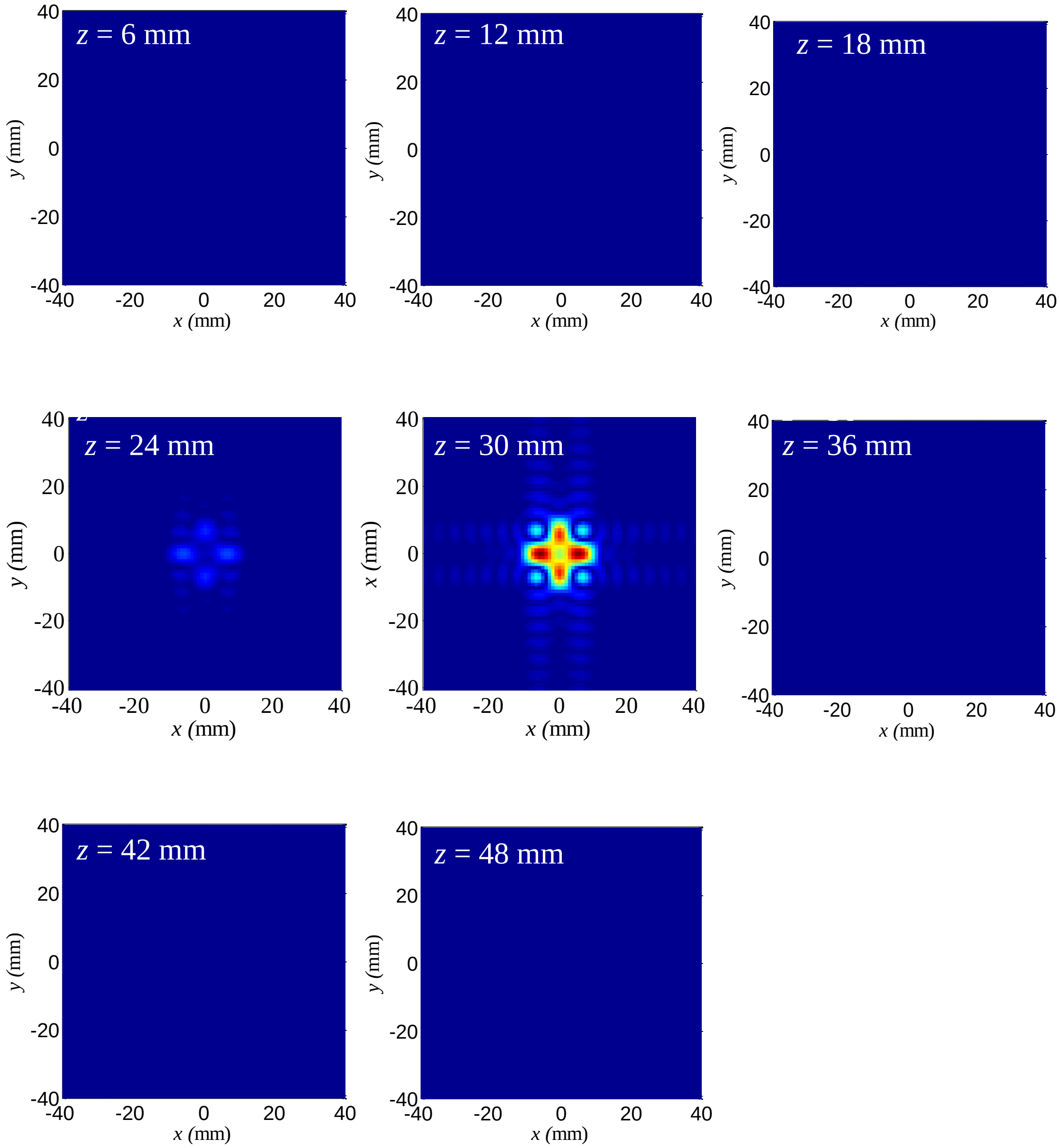

Fig. 5. Reconstructed images for the dielectric target in Fig. 2(a) using both co-polarized and cross-polarized data.

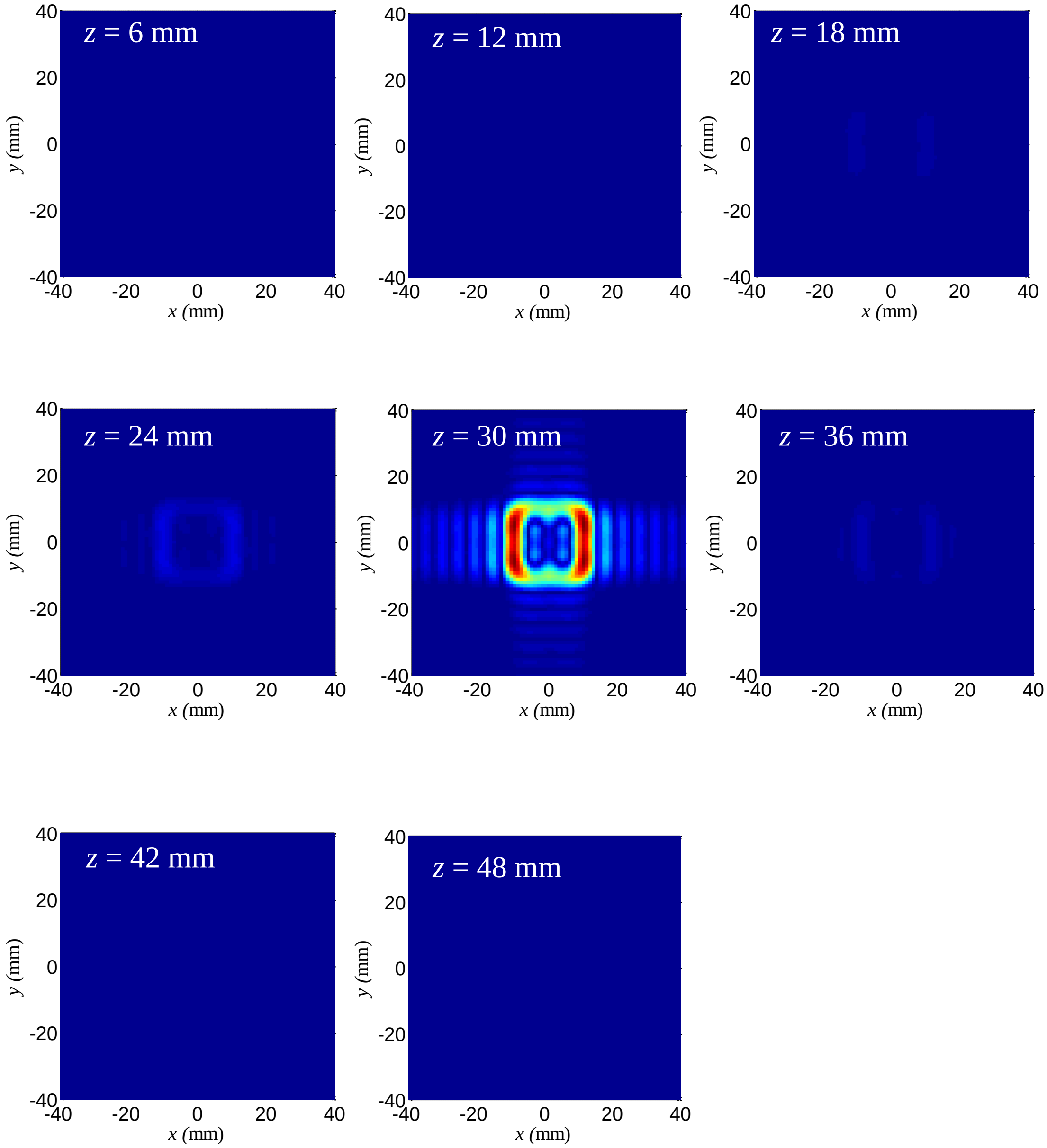

Fig. 6. Reconstructed images for the dielectric target in Fig. 2(b) using co-polarized data only.

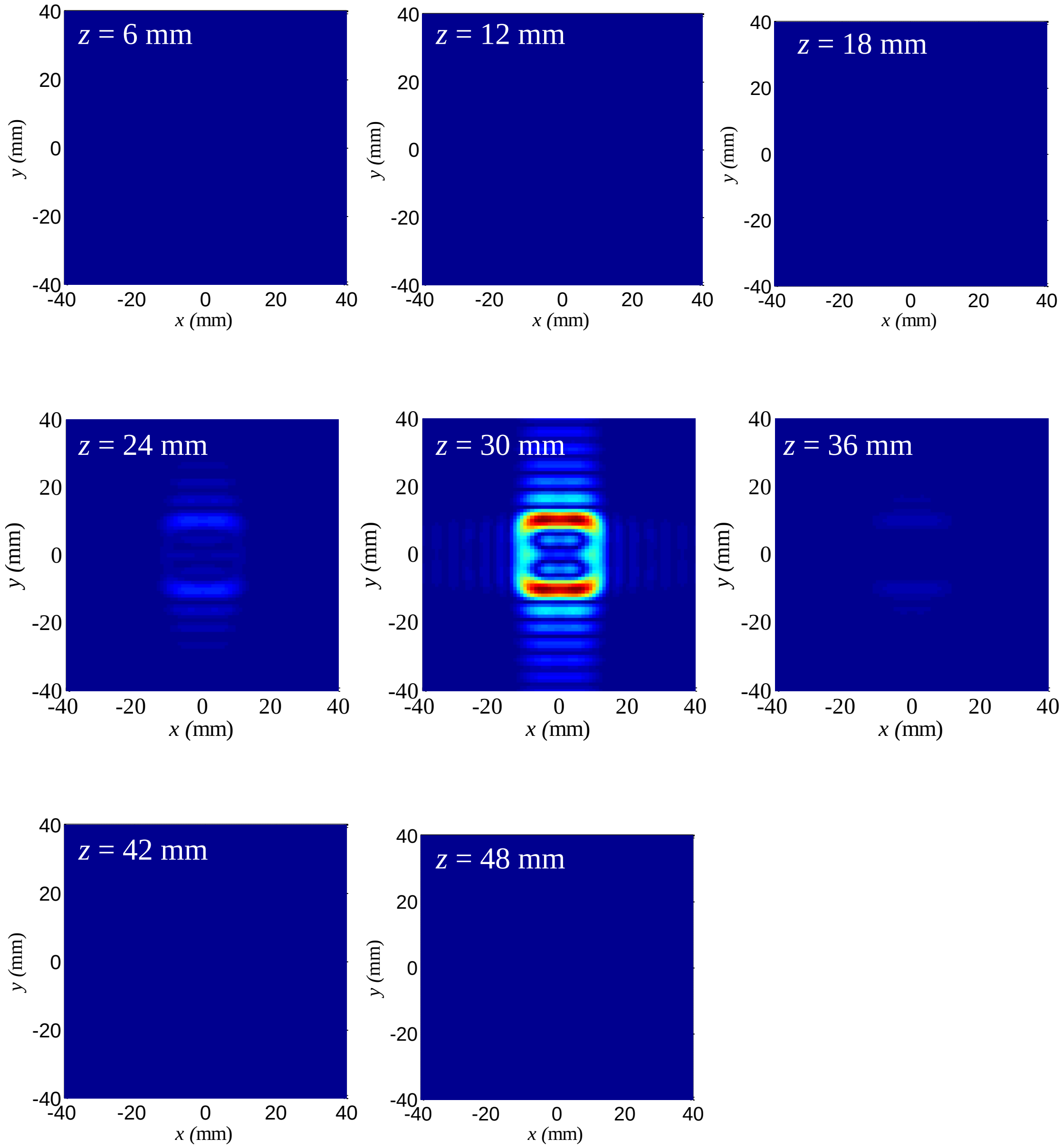

Fig. 7. Reconstructed images for the dielectric target in Fig. 2(b) using cross-polarized data only.

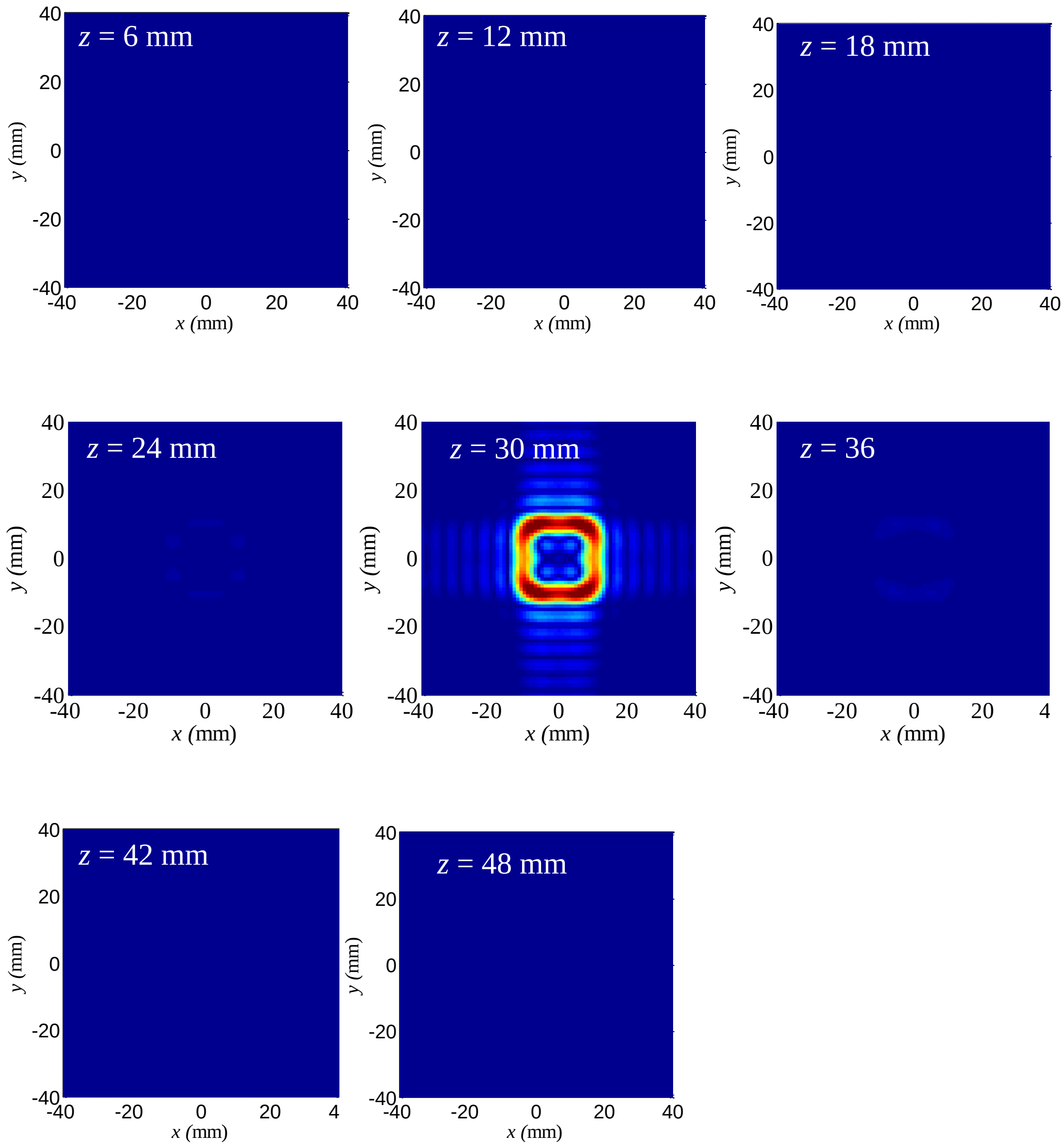

Fig. 8. Reconstructed images for the dielectric target in Fig. 2(b) using both co-polarized and cross-polarized data.

2.4 CONCLUSION

In this chapter, we proposed a full vector 3D microwave holographic imaging algorithm. This new formulation allows for combining the data measured with both co- and cross-polarized antennas in a single reconstruction process. We confirmed the improvement in the image reconstruction process by two simulation examples. The dielectric properties and the operating frequency band for the examples were chosen to be close to those considered in the microwave imaging of biological tissues. We observe that when using single polarization measurements, the shape components of the targets oriented along the receiving antenna polarization appear with higher contrast. However, when using both co- and cross-polarized data, all details appear with almost similar contrast. We should emphasize that this approach provides systems of equations with much smaller number of unknowns compared to the systems of equations constructed in regular optimization-based techniques (where the number of unknowns is equal to the number of reconstructed voxels). This reduces the ill-posedness of the proposed technique significantly.

REFERENCES

[1] D. M. Sheen, D. L. McMakin, and T. E. Hall, "Three-dimensional millimeter-wave imaging for concealed weapon detection," *IEEE Trans. on Microwave Theory and Tech.*, vol. 49, no. 9, pp. 1581−1592, Sep. 2001.

[2] D. M. Sheen, D. L. McMakin, and T. E. Hall, "Near field imaging at microwave and millimeter wave frequencies," *IEEE/MTT-S Int. Microwave Symp*., pp. 1693−1696, Jun. 2007.

[3] M. Ravan, R. K. Amineh, and N. K. Nikolova, "Two-dimensional near-field microwave holography," *Inverse Problems*, vol. 26, no. 5, May. 2010.

[4] M. Ravan, R. K. Amineh, and N. K. Nikolova, “Microwave holography for near-field imaging,” *IEEE AP-S/URSI Int. Symp. on Antennas and Propagation*, July 2010.

[5] M. Ravan, R. K. Amineh, and N. K. Nikolova, “Near-field microwave holographic imaging: target localization and resolution study,” *XX URSI Comm. B Int. Symp. on Electromagnetic Theory* (EMT-S 2010), Aug. 2010.

[6] R. K. Amineh, M. Ravan, A. Khalatpour, and N. K. Nikolova “Three-dimensional near-field microwave holography using reflected and transmitted signals,” accepted for publication in *IEEE Trans. Antennas Propag.*

[7] R. K. Amineh, A. Khalatpour, and N. K. Nikolova, “three-dimensional near-field microwave holography using co-polarized and cross-polarized data,” submitted to *IEEE Antennas Wireless Propag. Lett.*

[8] W. Chew, *Waves and Fields in Inhomogeneous Media*, Piscataway, NJ: IEEE Press, 1995.

[9] M. Slaney, A. C. Kak, and L. E. Larsen, “Limitation of imaging with first-order diffraction tomography,” *IEEE Trans. on Microwave Theory and Tech.*, vol. 32, no. 8, pp. 860−874, Aug. 1984.

[10] EM software & systems-S.A. (Pty) Ltd., http://www.feko.info.

CHAPTER 3

IMAGE QUALITY ENHANCEMENT IN THE MICROWAVE RASTER SCANNING METHOD

3.1 INTRODUCTION

Microwave imaging is a promising technique for near-field imaging of dielectric bodies. It can be employed for imaging of biological tissues [1], non-destructive testing of materials [2], etc. Although significant progress has been made on hardware developments, reliable processing techniques are still needed in order to extract maximum information from the measurement data.

Aperture raster scanning is a fast, reliable, and robust microwave imaging method for creating images of the interior of dielectric bodies. Recently, an ultra-wide band (UWB) antenna [3] has been tailor-made for planar aperture raster scanning of biological tissues or phantoms thereof without the need for coupling liquids. It is shown that more than 90% of the radiated power is coupled to the tissue via the antenna's front aperture. In the imaging setup, two of these antennas are placed face-to-face on both sides of a compressed tissue [3]. The transmitting and the receiving antennas perform a two dimensional (2D) scan while moving together on two separate parallel planes (transmitter and receiver planes) positioned at $z=0$ and $z=D$, respectively, as illustrated in Fig. 1. The coupling coefficient (S_{21} parameter) between the two antennas is measured at each sampling position while they perform a 2D scan.

A 2D near-field holographic imaging technique has been proposed in [4]. The required complex-valued data (scattering parameters) in this method is collected at a single frequency from a 2D raster scanning setup identical to the one illustrated in Fig. 1.

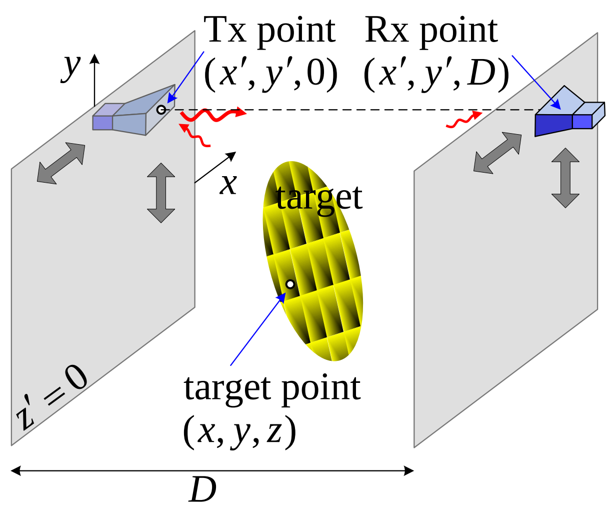

Fig. 1. Microwave raster scanning setup.

The holographic imaging requires complex-valued scattered field data. It is best if the field is sampled by a point-wise receiver. When an antenna with non-point-wise (realistic) aperture is utilized in the measurement, the integration effect of the aperture reduces the quality of the reconstructed images, e.g., the images are blurred. In order to remove this integration effect, as a first step, we employ a complex-valued blind de-convolution algorithm. This provides the required complex-valued data for the holographic imaging as a second processing step.

The efficiency of applying combined complex-valued blind deconvolution and microwave holographic imaging is examined through simulations and experiments with tissue phantoms.

3.2 BACKGROUND FOR 2D HOLOGRAPHY

With reference to Fig. 1, the target is positioned at $z = \bar{z}$ and its thickness along the *z*-axis is assumed negligible. A method to find the true position of the target $\bar{z}$ has been presented in [4].

In general, we can use both transmission and reflected signals. Here, we limit our study to transmitted signals only due to their high signal-to-noise ratio in both measurements and simulations.

The transmitting and the receiving antennas perform the 2D scan by moving together on two separate parallel planes (transmitter and receiver planes) positioned at *z* = 0 and *z* = *D*, respectively. Assume we know the incident field (the field in the same region when the target is not present) $s^{\text{inc}}(x, y, \bar{z})$ at the $z = \bar{z}$ plane as a function of *x* and *y* when the transmitting antenna is at $x' = 0$, $y' = 0$ ($\bar{z} = 0$ at the transmitting plane. In this case the transmission function is defined as[4]

$$\bar{g}(x, y, \bar{z}) = s^{\text{inc}}(x, y, \bar{z}) g(x, y, D - \bar{z}) \tag{1}$$

where $g(x, y, z)$ is the Green function of the medium for a point source at $(x, y, \bar{z})$ and an observation point at $(0,0,0)$.

The scattered wave due to a point target at $(x, y, \bar{z})$, when the transmitting and the receiving antennas are at $(x', y', 0)$ and (x', y', D), respectively, is denoted by $t(x', y')$. This represents the acquired *S*-parameters. Then, the contrast function of the target $f(x, y, \bar{z})$ is obtained as[4]:

$$f(x, y, \bar{z}) = \mathrm{F}_{2\mathrm{D}}^{-1} \left\{ \frac{T(k_x, k_y)}{\bar{G}(k_x, k_y, \bar{z})} \right\} \tag{2}$$

where $T(k_x, k_y)$ and $\bar{G}(k_x, k_y, \bar{z})$ are the 2D Fourier transforms (FT) of $t(x', y')$ and $\bar{g}(x, y, \bar{z})$, respectively, and $\mathrm{F}_{2\mathrm{D}}^{-1}$ denotes the inverse 2D FT. By plotting $|f(x, y, \bar{z})|$ versus *x* and *y*, we can produce a 2D colormap image of the target.

The Green function can be obtained numerically by putting an infinitesimal dipole at the origin. The electric field of this dipole is the Green function of the medium. In the case of a uniform medium, the Green function is available analytically[4]:

$$g(x, y, z) = \frac{e^{-ik\sqrt{x^2+y^2+z^2}}}{\sqrt{x^2 + y^2 + z^2}} \ . \tag{3}$$

3.3 COMPLEX-VALUED BLIND DECONVOLUTION

In image processing terminology, the convolution of an image with a point-spread function (PSF) results in a blurred image, i.e., $S_{\text{blurred}} = S_{\text{true}} * \text{PSF}$. In the ideal case, there would be no blurring, i.e., $S_{\text{blurred}} = S_{\text{true}}$ which implies that $\text{PSF}=\delta(x, y)$ where δ is the Dirac function. A PSF different from the ideal case results from effects such as the motion of the camera (or sensor), poor focusing or noise. The image restoration technique, which finds the true image when the blurred image and the PSF are known, is called deconvolution. Blind deconvolution is a special case of deconvolution where both the point-spread function (PSF) and the imaged object are not completely known [5].

Here, we assume that the integration effect of the non-point-wise antenna aperture over the collected microwave power acts like a convolution process in the spatial domain. Because this effect varies with the tissue properties and the presence of the tumor, complete information of this effect is not available, so a blind deconvolution algorithm is needed to reconstruct the true image. It provides ‘deblurred’ complex-valued data required for the holographic imaging described in section 3.2.

There are two common blind deconvolution techniques: optimization- based blind deconvolution and iterative blind deconvolution. The iterative blind deconvolution (IBD) was first proposed by Ayers and Dainty [6][7]. This technique alternates, between updating the restored image and the PSF where the update constitutes a standard classic deconvolution. The Ayers and Dainty scheme uses inverse filtering with the associated difficulties in inverting small values of the image or PSF spectrum [6][7]. Davey *et al*. [7] improved the robustness to noise by using a Wiener filter. They also achieved reconstruction of complex-valued data through the inclusion of a support constraint.

In the optimization-based blind deconvolution, the PSF and the true image are obtained by minimizing the following objective function

$$(\boldsymbol{x}, \boldsymbol{p})^{*} = \operatorname{argmin}\ J(\overline{\boldsymbol{x}}, \overline{\boldsymbol{p}}) \tag{4}$$

where

$$J(\boldsymbol{x}, \boldsymbol{p}) = \left\| \boldsymbol{x} * \boldsymbol{p} - \boldsymbol{t} \right\|. \tag{5}$$

In which we assume $\boldsymbol{x}$ is the actual image, $\boldsymbol{p}$ is the PSF, and $\boldsymbol{t}$ is the blurred image. An example for solving (4) by use of simulated annealing is reported in [9]. In [10], a regularization term is added to (4) for penalizing the noise amplification and conjugate-gradient optimization is used.

In microwave imaging, the true image is a complex-valued signal, which does not possess positivity constraint and the data is often noisy. The Wiener filter [7] has proved to be a suitable deconvolution method for complex-valued noisy signals. Other well-known algorithms like the Richardson-Lucy algorithm [8][9] , are not applicable to this problem due to their requirements for the image to be positive and real. Here, we use a two-stage deconvolution which is a combination of the IBD using a Wiener filter and an optimization-based algorithm.

In the first stage, we use iterative blind deconvolution using a Wiener filter. In the deconvolution problem, where $S_{\text{blurred}} = S_{\text{true}} * \text{PSF}$, all pairs $(S_{\text{true}} / k, k \times \text{PSF})$ with k is being any complex number are possible solutions. This leads to nonuniqueness of the problem minima in the problem. To avoid this, we impose a normalization constraint $\left\|\boldsymbol{x}^{(k)}\right\| = 1$ on the image as it has no effect on the holographic imaging but it facilitates the convergence of the blind deconvolution algorithm. The constraints on the PSF can also be imposed (positivity, symmetry).

Suppose $\boldsymbol{x}$ is the desired point-wise data, $\boldsymbol{p}$ is the PSF (due to the non-point-wise antenna aperture), and $\boldsymbol{t}$ is the blurred data measured by the antenna, i.e., $\boldsymbol{x} * \boldsymbol{p} = \boldsymbol{t}$, where $*$ denotes a 2D convolution operator in the spatial domain. Here, we assume that the initial guess for the PSF is available. We describe the methods for estimation of the initial PSF in section 3.4. The algorithm to obtain $\boldsymbol{x}$ is summarized as follows:

Step 1: Set k = 1; estimate $\boldsymbol{p}^{(0)}$.

Step 2: Find $\boldsymbol{x}^{(k)}$ with the Wiener filter algorithm using $\boldsymbol{p}^{(k-1)}$.

Step 3: Impose the normalization constraint: $\left\|\boldsymbol{x}^{(k)}\right\| = 1$, where $\|.\|$ denotes the 2-norm operator.

Step 4: Find $\boldsymbol{p}^{(k)}$ with the Wiener filter algorithm using $\boldsymbol{x}^{(k)}$.

Step 5: If $\left\|\boldsymbol{x}^{(k)} * \boldsymbol{p}^{(k)} - t\right\| \leq \varepsilon$ (ε is a pre-determined sufficiently small number) go to Step 7; else, go to Step 6.

Step 6: Set $k = k$+1; go to Step 2.

Step 7: Terminate.

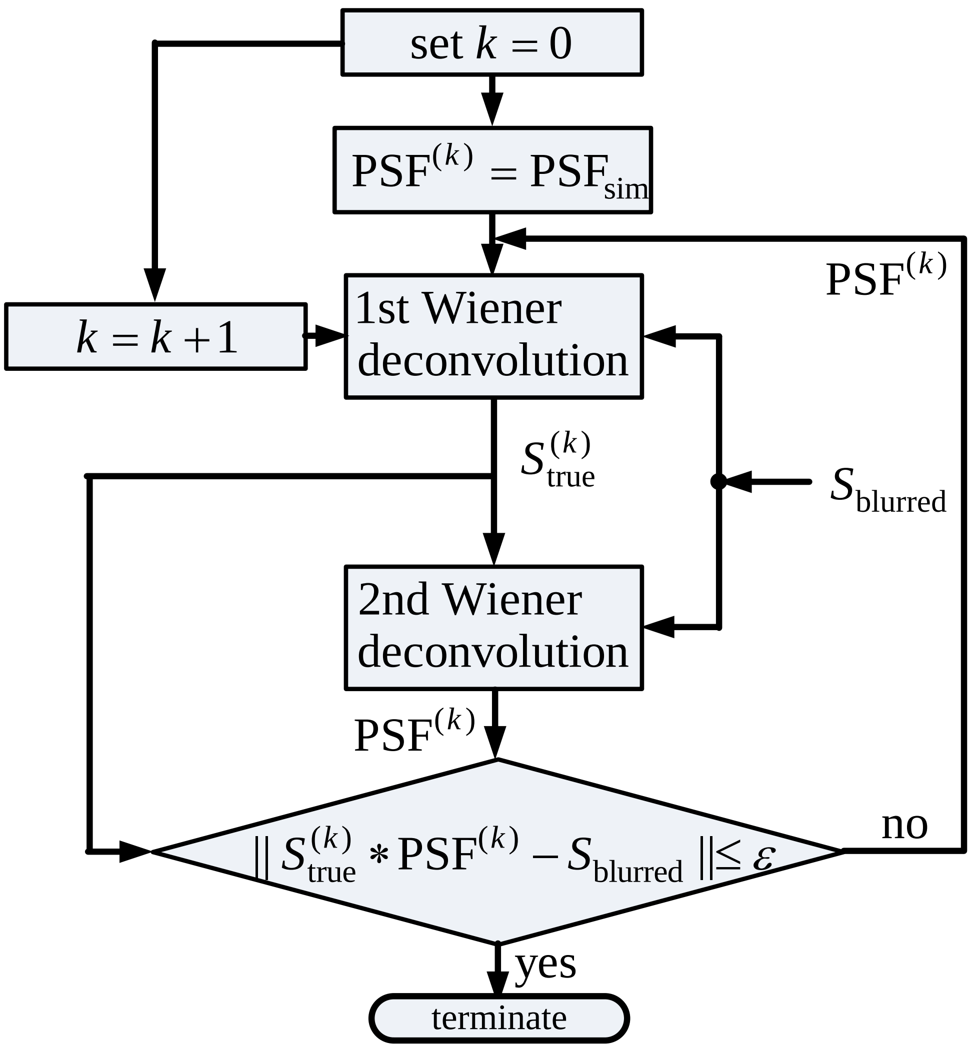

Fig. 2. Iterative blind deconvolution using a Wiener filter.

The overall algorithm is shown in also illustrated in Fig. 2 with a flow diagram. We use the Wiener filter algorithm available in MATLAB [12] .

The solution from the IBD is not the best possible solution as there is no guarantee for finding the global minimum of the problem. However, this approach is fast and it may provide a good starting point for the second stage, which is an optimization-based blind deconvolution. Here, we formulate our optimization problem as follow:

$$\begin{aligned} (\boldsymbol{x}, \boldsymbol{p})^* &= \operatorname{argmin} J(\overline{\boldsymbol{x}}, \overline{\boldsymbol{p}}), \quad \text{where} \\ J(\boldsymbol{x}, \boldsymbol{p}) &= \|\boldsymbol{x} * \boldsymbol{p} - \boldsymbol{t}\| + (1 - \|\boldsymbol{x}\|)^2. \end{aligned} \tag{6}$$

We use simulated annealing to obtain a global minimum for (6) [13]. There are other global minimum optimizers, which can be used to solve (6) [13]. The principle disadvantage of the global optimization is the computational burden for large-scale problems. Here, however, the number of unknowns is not large (typically 800 unknown). The summary of the two stages is shown in Fig. 3. The implementation of the deblurring procedure in MATLAB is shown in Appendix.

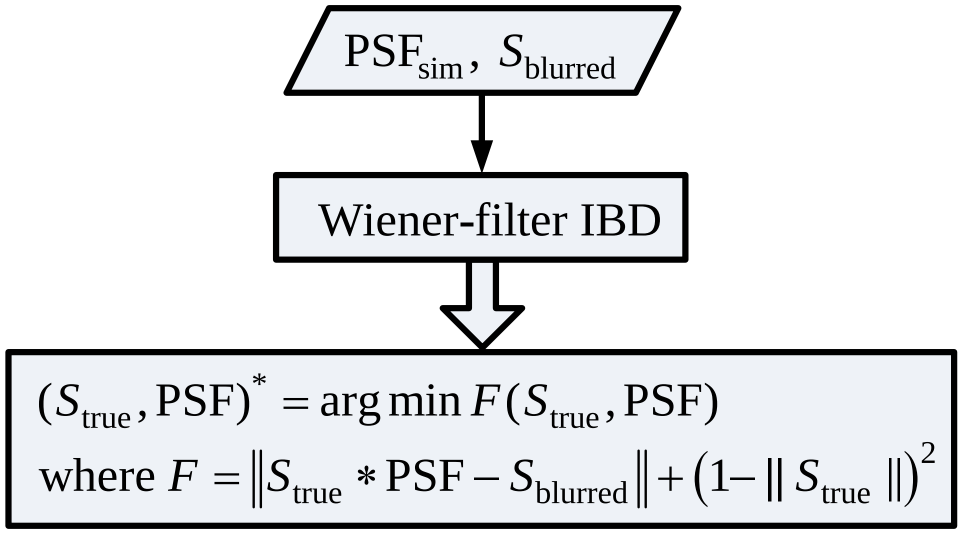

Fig. 3. Summary of the two stage blind deconvolution.

3.4 ESTIMATION OF THE INITIAL PSF

The accurate estimation of the size of the PSF is crucial in blind deconvolution algorithms [5]. Here, the size of the PSF is known *a priori* which is the size of the antenna aperture. In discrete form, the PSF is a $m \times n$ matrix where m and n are equal to the sides of the antenna aperture divided by the sampling rate (e.g., for 5 mm spatial sampling is 5×7).

Theoretically, we can estimate the PSF via raster scanning of a small but detectable metallic object located at the center of the setup. The reason for putting a metallic object is to have maximum sensitivity to its presence. The effectiveness of this approach depends on the sensitivity of the imaging setup to detect small objects.

The second approach for obtaining initial guess for the PSF is to use the results of raster scanning for known objects. The scattering field from this object should be considerable to have high signal-to-noise ratio. Here, we use a metallic sphere with the diameter 10 mm which is half of the length of the antenna aperture. Increasing the size of this known object will increase the simulation time but will keep the effect approximately unchanged. In general we can use both the transmitted and reflected signals. Here, because the transmitted signal is more sensitive to the presence of the object, we measure S_{21}. As shown in Fig. 4, first a 2D scan is performed by the actual antennas for the reference object. The data acquired in this setup is blurred by the integration effect of the receiver antenna. We call the measured data S_{blurred}. Another scan is performed by replacing the receiver antenna with a point-wise antenna. In this setup, the integration effect of the antenna is removed because of the point-wise antenna at the receiver side. We call the measured data S_{true}. The following relation can be made between the measured data and the PSF of the antenna:

$$S_{\text{true}} * \text{PSF} = S_{\text{blurred}}. \tag{7}$$

The PSF due to the effect of the antenna aperture can then be estimated by applying direct deconvolution to (7). We used Wiener deconvolution implemented in MATLAB [11] for solving (7). It is worth mentioning that the obtained PSF is strictly valid only for this setup. It could serve as an initial estimate of the PSF in the same frequency for other imaging setups in which the PSF would be slightly different due to the change in the material properties and the object’s shape. We call this approach the two-antenna approach. The two-antenna approach is preferable to the raster scanning of a small object if the sensitivity of the imaging setup is not sufficient for the imaging of a very small object.

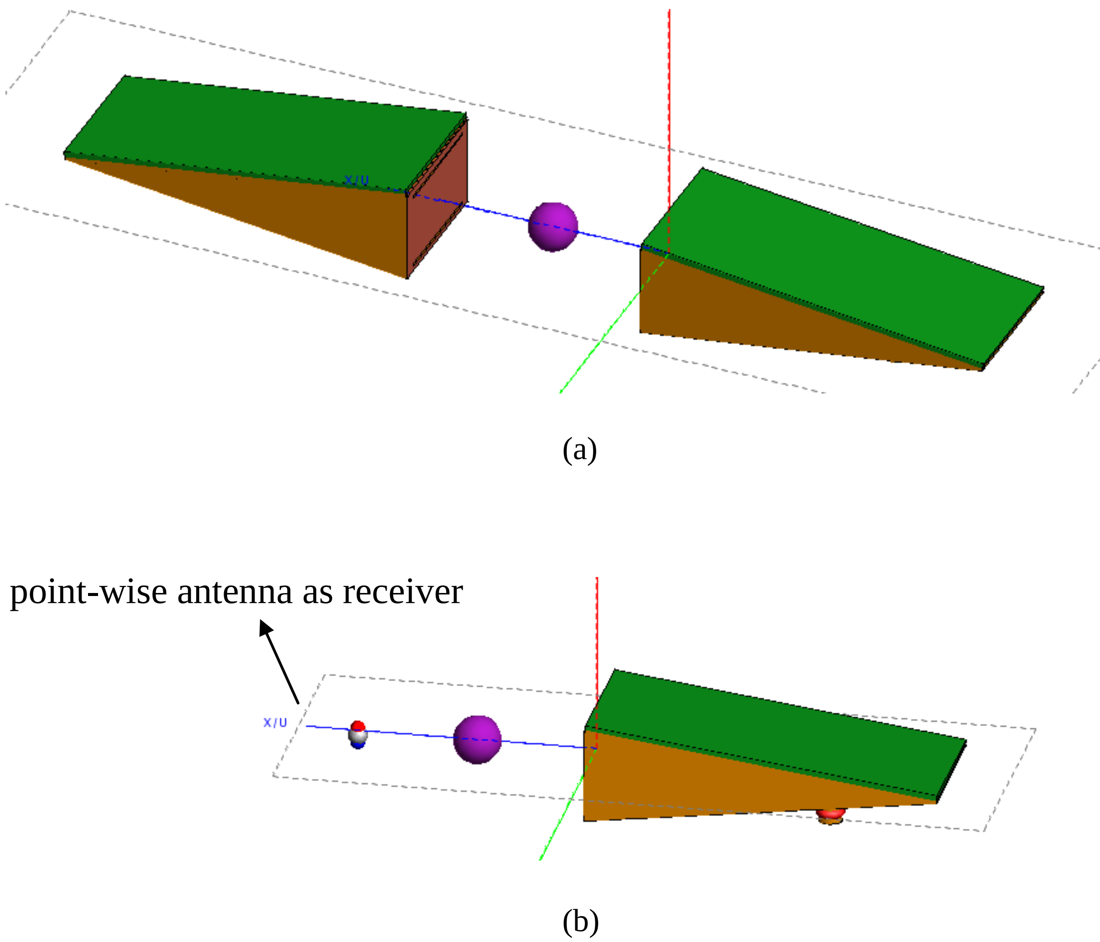

Fig. 4. Simulation setup for the estimation of the PSF in FEKO: (a) raster scan with the actual antennas; (b) raster scan with the actual antenna as the transmitter and a point-wise receiving antenna

3.5 IMAGE RECONSTRUCTION RESULTS

To verify the proposed processing algorithms, we present simulation and experimental results. The properties of the background medium and the targets are chosen to be close to those of biological healthy and cancerous tissues, respectively. In both measurement and simulation, the Green function and the field of antenna are calculated numerically.

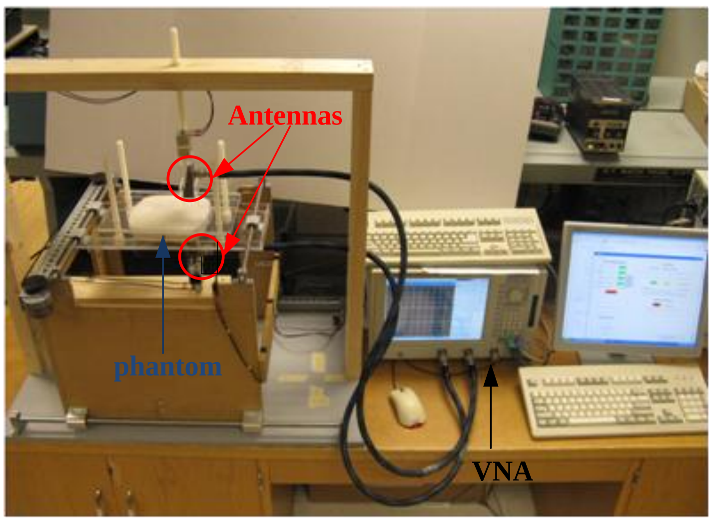

Fig. 5. Experimental set up for the aperture raster scanning.

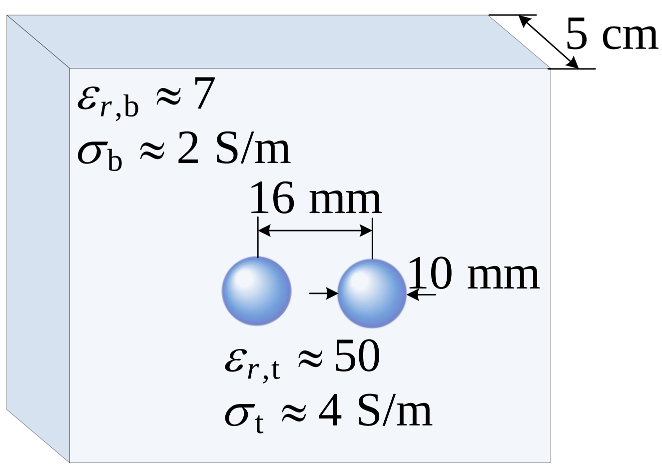

Fig. 6. Sketch of the measurement example.

In the first example (Fig. 6), we use the measured data from the 2D raster scanning setup shown in Fig. 5. The targets are two spheres with $\varepsilon_r \approx 50$ and $\sigma \approx 4$ S/m resembling tumors. They are made of alginate powder and are embedded inside a glycerin-based slab phantom emulating a tissue with $\varepsilon_r \approx 7$ and $\sigma \approx 1$ S/m. The diameter of spheres is 10 mm and the center-to-center distance between them is 16 mm. The phantom is compressed between two thin plexi-glass sheets. The distance between the antenna apertures after this compression is 50 mm. The antennas perform 2D scan on a region of size 70 mm by 70 mm with a spatial sampling rate of 5 mm. This scanning is performed by an automatic positioning system. At each sampling position, the complex coupling S-parameters between the two antennas (S_{21}) are measured at 5 GHz, 7 GHz, and 9 GHz using a vector network analyzer (VNA). The VNA averaging and resolution bandwidth are set to 16 and 1 KHz, respectively. Here, we obtained the initial PSF by the two-antenna approach, which was explained in section 3.2. Calibration is performed by subtracting the measured S-parameters obtained from the raster scanning of a phantom without tumor from those obtained from a phantom with tumor. In both cases, the background phantom properties are the same.

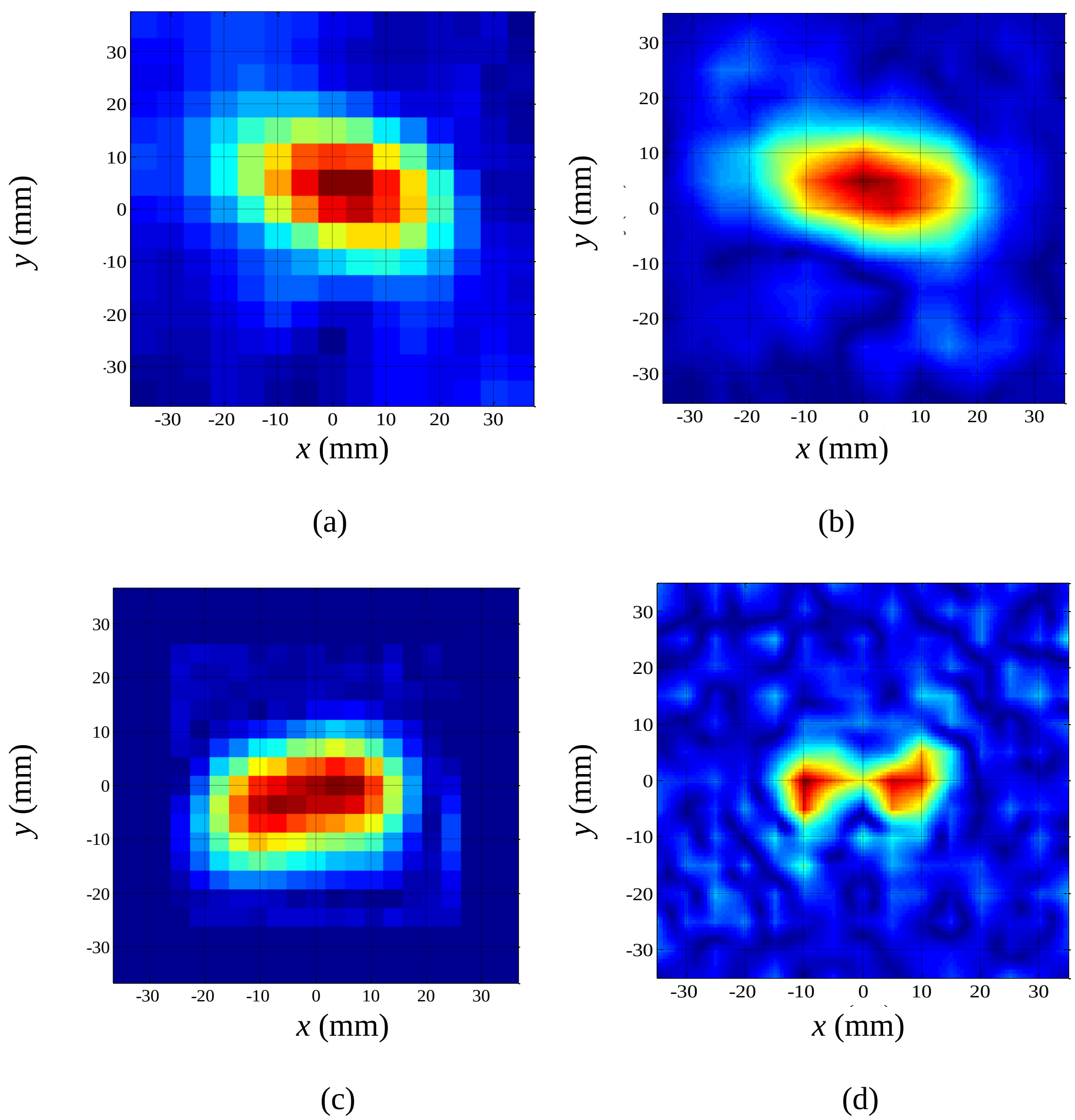

Fig. 7. (a) Raw image obtained from the calibrated $|S_{21}|$ for the example shown in Fig. 6 at 5 GHz. (b) Image obtained after applying blind de-convolution. (c) Image obtained after applying holographic imaging to the collected complex-valued S_{21}. (d) Image obtained after applying blind de-convolution and holographic imaging.

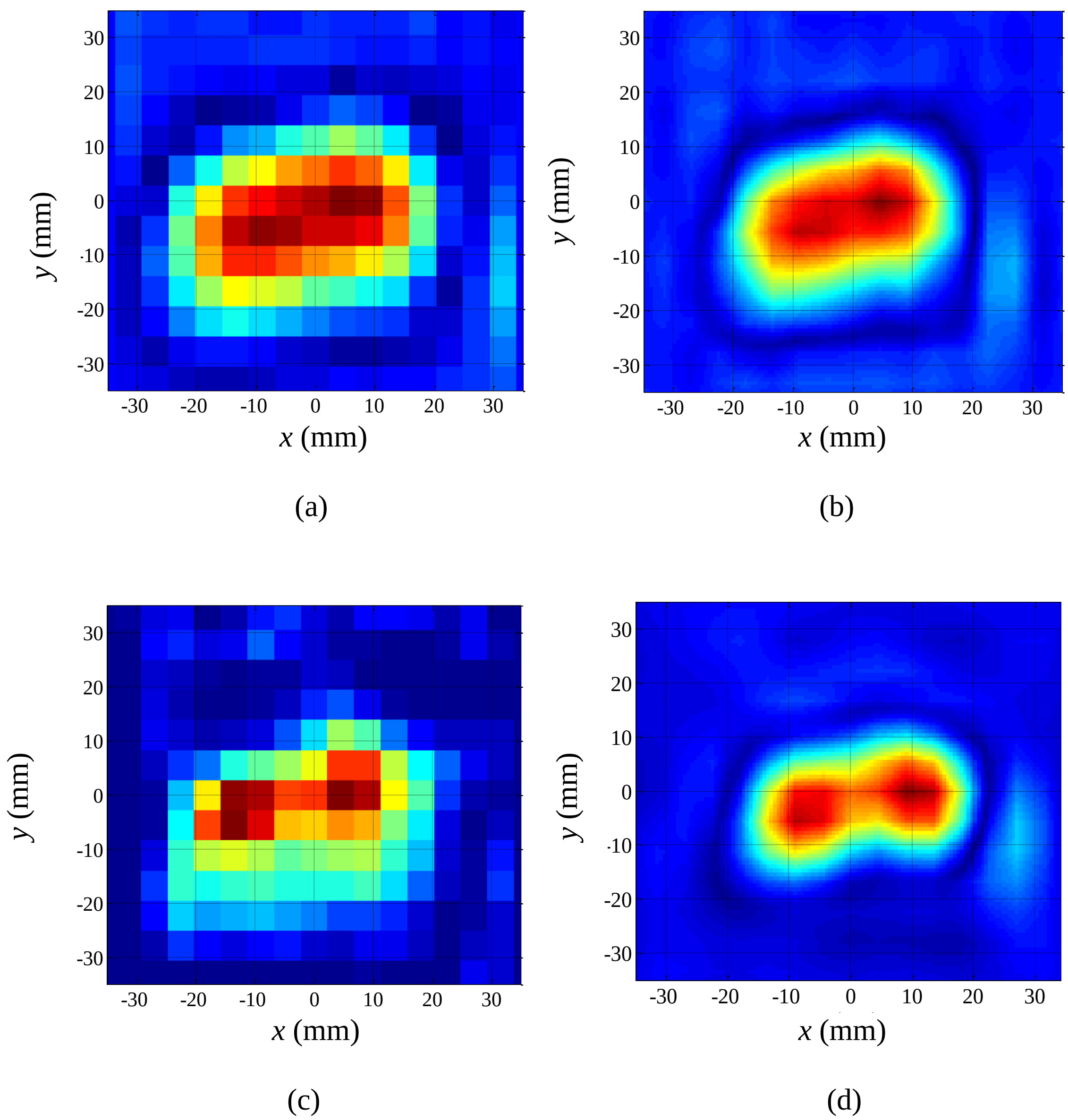

Fig. 8. (a) Raw image obtained from the calibrated $|S_{21}|$ for the example shown in Fig. 6 at 7 GHz. (b) Image obtained after applying blind de-convolution. (c) Image obtained after applying holographic imaging to the collected complex-valued S_{21}. (d) Image obtained after applying blind de-convolution and holographic imaging.

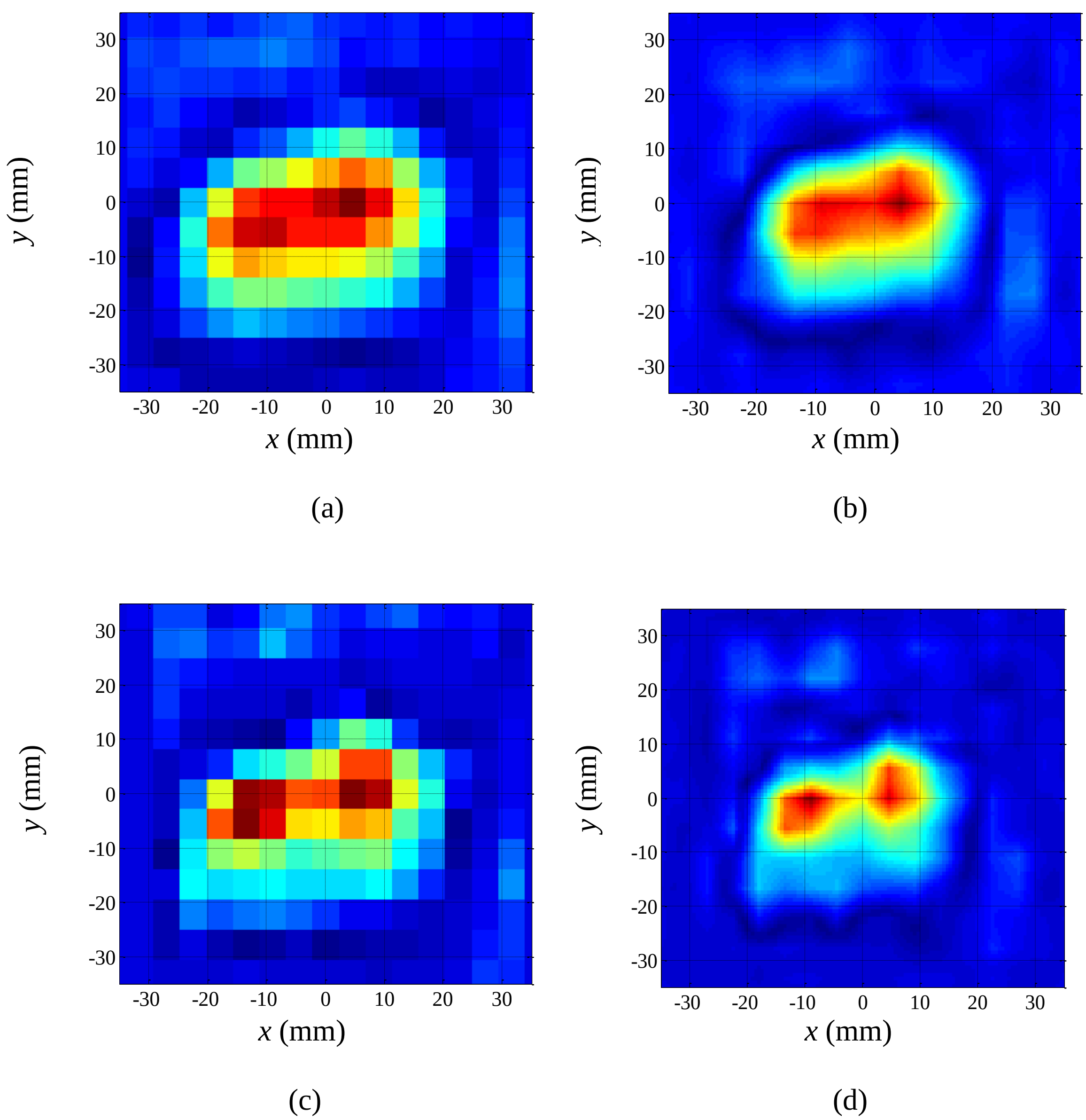

Fig. 9. (a) Raw image obtained from the calibrated $|S_{21}|$ for the example shown in Fig. 6 at 9 GHz. (b) Image obtained after applying blind de-convolution. (c) Image obtained after applying holographic imaging to the collected complex-valued S_{21}. (d) Image obtained after applying blind de-convolution and holographic imaging.

Figs. 7(a), 8(a), and 9(a) show the raw images created from the calibrated $|S_{21}|$ signals obtained from the measurement setup shown in Fig. 5. The two tumor stimulants cannot be distinguished easily especially at 5 GHz. Then we apply holographic imaging algorithm to the complex-valued S_{21}. Figs. 7(b), 8(b), and 9(b) show the reconstructed images. As seen in these figures, the targets still cannot be distinguished in the image due to the integration effect of the antenna aperture. To remove this effect, we apply the blind deconvolution to the calibrated S_{21} (Figs. 7(c), 8(c), and 9(c)) and then apply holographic imaging. Figs. 5(d), 6(d), and 7(d) show the reconstructed images. The targets are clearly distinguished in these images. Finally, we note that the improvement through blind deconvolution cannot be appreciated without applying holography.

In the second example, we use FEKO simulation data from the 2D raster scanning of five spheres with ε_r = 15 and σ = 2 S/m embedded inside a medium with ε_r = 10 and σ = 1 S/m as shown in Fig. 8. The diameter of the spheres is 7.6 mm and the center-to-center distance between the spheres is 15 mm. The distance between the antenna apertures is 5 cm. The spatial sampling is 5 mm at 5 GHz. The spatial sampling is 3 mm at 7 GHz and 9 GHz. Here, we obtained the initial PSF by the two-antenna approach explained in section 3.2.

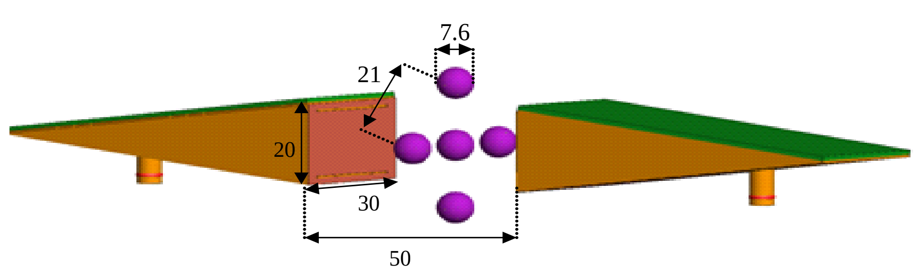

Fig. 10. The simulation setup in FEKO. The dimensions are in mm.

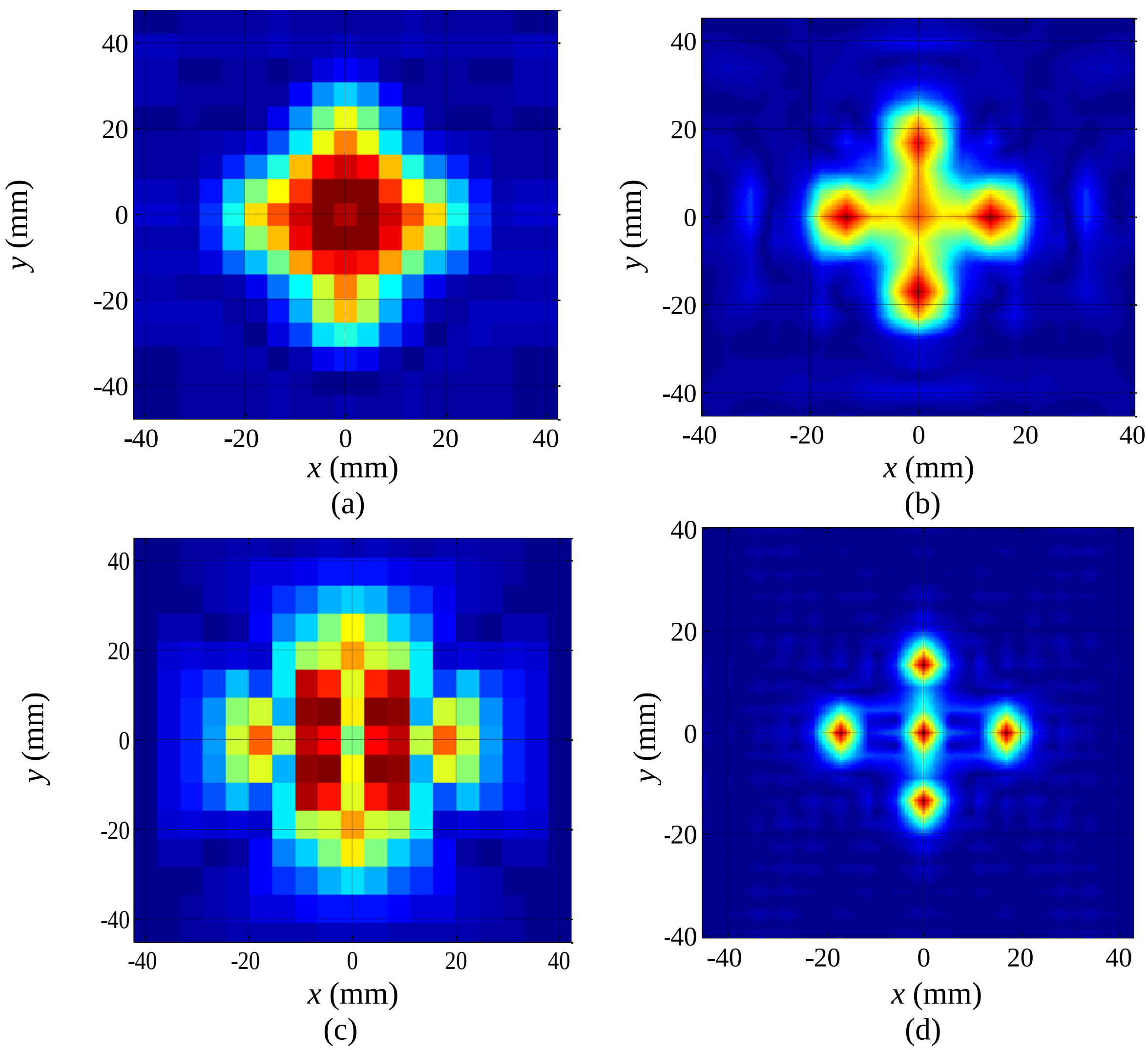

Fig.11. (a) Raw image obtained from the calibrated $|S_{21}|$ for the example shown in Fig. 10 at 5 GHz. (b) Image obtained after applying blind de-convolution. (c) Image obtained after applying holographic imaging to the collected complex-valued S_{21}. (d) Image obtained after applying blind de-convolution and holographic imaging.

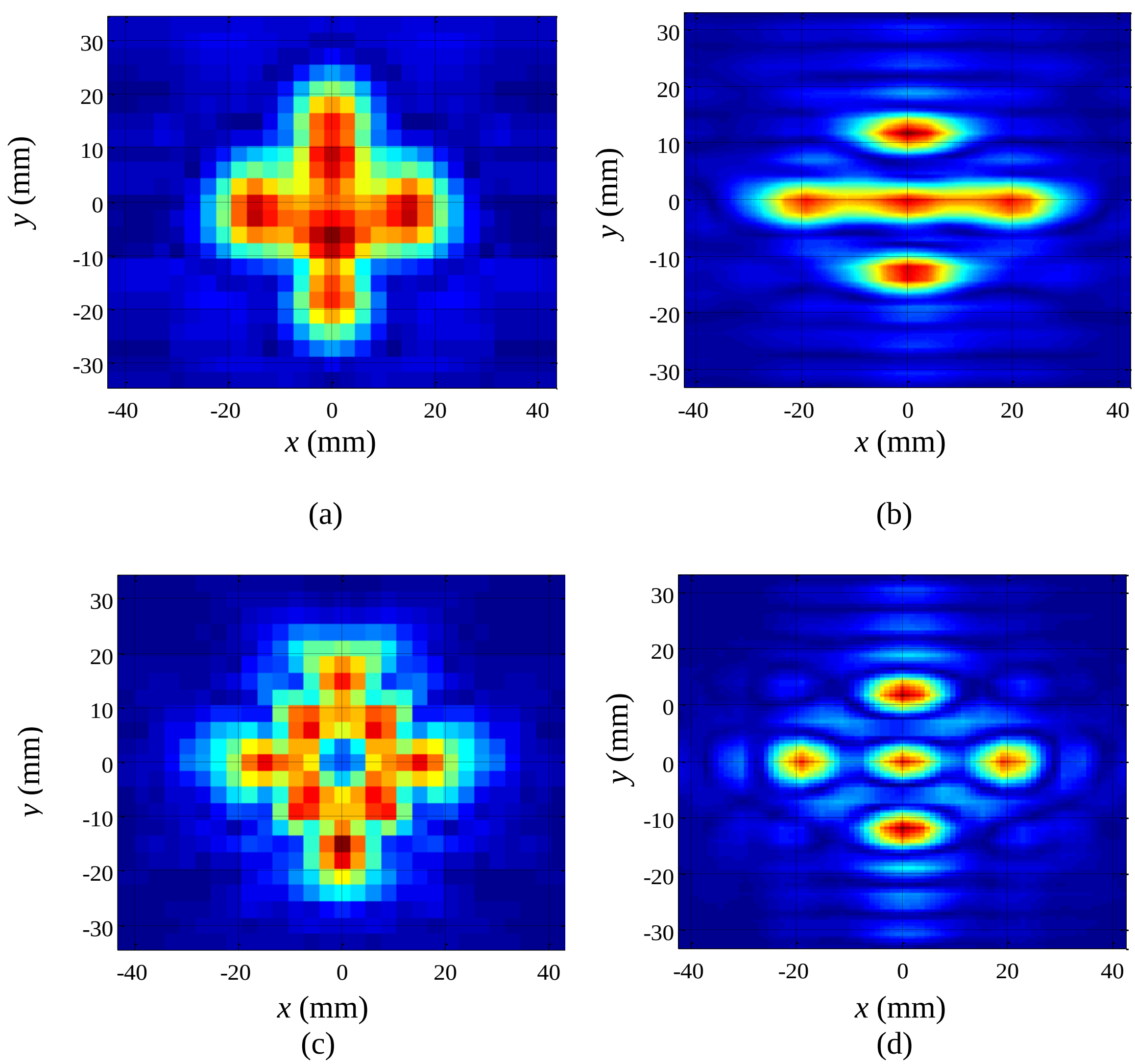

Fig.12. (a) Raw image obtained from the calibrated $|S_{21}|$ for the example shown in Fig. 10 at 7 GHz. (b) Image obtained after applying blind de-convolution. (c) Image obtained after applying holographic imaging to the collected complex-valued S_{21}. (d) Image obtained after applying blind de-convolution and holographic imaging.

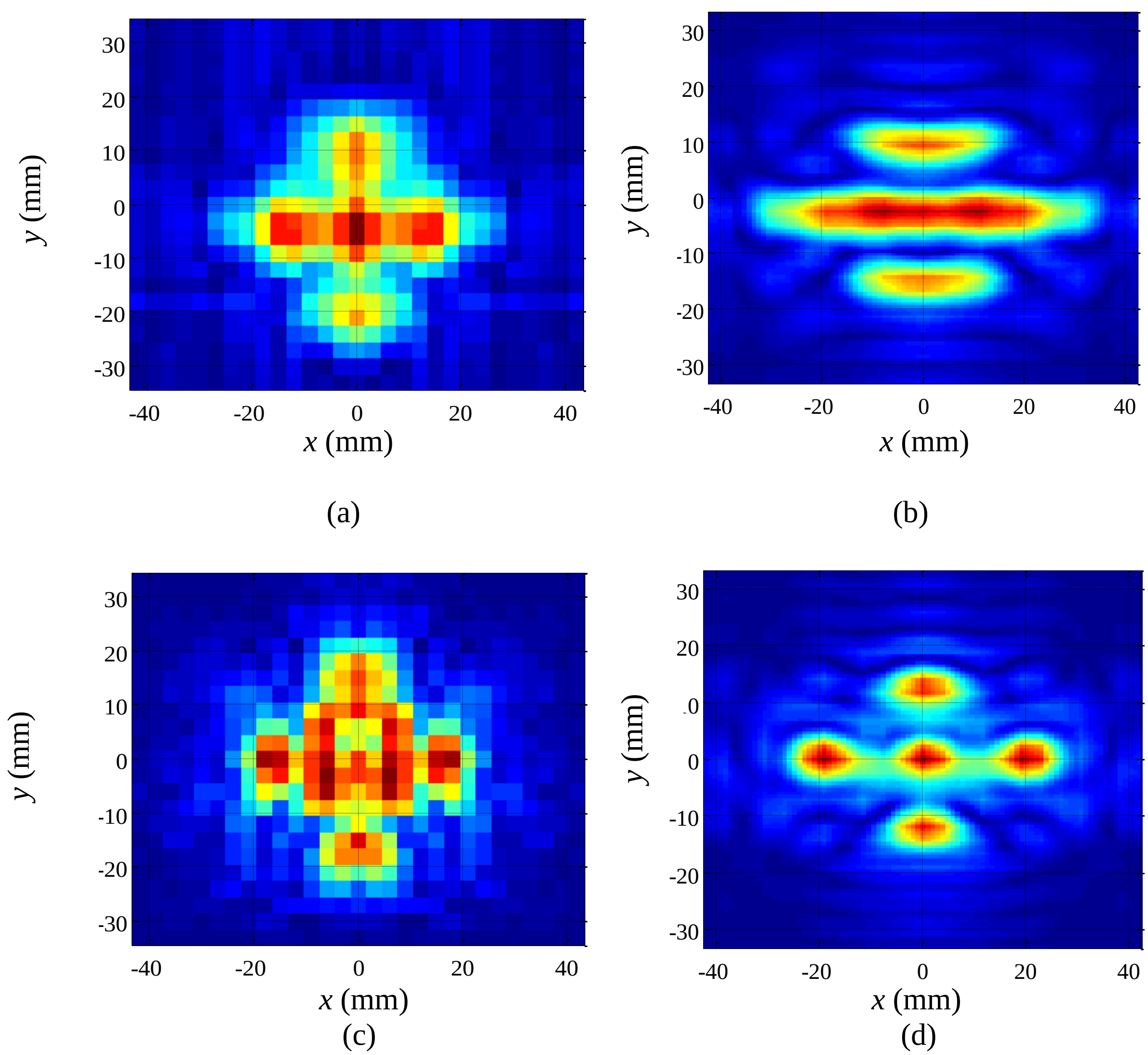

Fig.13. (a) Raw image obtained from the calibrated $|S_{21}|$ for the example shown in Fig. 10 at 9 GHz. (b) Image obtained after applying blind de-convolution. (c) Image obtained after applying holographic imaging to the collected complex-valued S_{21}. (d) Image obtained after applying blind de-convolution and holographic imaging.

Figs. 11(a), 12(a), and 13(a) show the raw images obtained from the calibrated $|S_{21}|$ acquired with the simulation setup shown in Fig. 10. The 5 spheres cannot be distinguished easily especially at 5 GHz. Then we apply the holographic imaging algorithm to the complex-valued S_{21}. Figs. 11(b), 12(b), and 13(b) show the reconstructed images. As seen in these figures, the targets still cannot be distinguished in the images due to the integration effect of the antenna aperture. To remove this effect, we apply blind deconvolution to the calibrated S_{21} (Figs. 11(c), 12(c), and 13(c)) and then apply holographic imaging. Figs. 11(d), 12(d), and 13(d) show the reconstructed images. The targets are clearly distinguished in these images. Finally, similarly to the measurement results, we note that the improvement through blind deconvolution cannot be appreciated without applying holography.

3.6 CURRENT ISSUES FOR EXTENSION TO 3D HOLOGRAPHY

The proposed deblurring approach can be implemented with 3D holography, where depth information becomes available. At the time of writing of this thesis, however, we were unable to obtain the proper reflection signals (S_{11} and S_{22}). These are crucial for the 3D holography reconstruction. The problem arises from the very low signal-to-noise ratio for the reflection coefficients. The level of the tumor signatures[1] falls below the level of the noise in the current setup. Improving the quality of the measurement setup and designing new sensors may help solve the problem.

[1]Tumor signature is the variation of measured signal due to the presence of tumor

Similar problems exist in the numerical simulation. The tumor signature falls below the level of the numerical error in the current setup especially at frequencies above 8 GHz. One way to overcome this problem in the simulation is to move the objects during the 2D scan instead of the antenna. This decreases the meshing error and helps to improve the accuracy of the simulated reflection coefficients.

Applying these methods to 3D holography in both measurement and simulation is the final stage of this research. This is the subject of future work.

3.7 CONCLUSION

We presented complex-valued blind deconvolution and holographic imaging as post-processing techniques for data acquired with microwave aperture raster scanning. The collected complex *S*-parameters obtained from a 2D planar scan at a single frequency are first processed by a blind deconvolution algorithm to remove the integration effect of the antenna aperture. Then, the complex-valued de-blurred data is processed by a holographic imaging algorithm. We have shown that the combination of these two algorithms leads to significant enhancement of the image quality.

REFERENCES

[1] E. C. Fear, S. C. Hagness, P. M. Meaney, M. Okoniewski, and M. A. Stuchly, "Enhancing breast tumor detection with near-field imaging," *IEEE Microwave Magazine*, vol. 3, no. 1, pp. 48−56, Mar. 2002.

[2] R. Zoughi, *Microwave Non-destructive Testing and Evaluation*, Kluwer Academic Publishers, 2000.

[3] R. K. Amineh, M. Ravan, A. Trehan, and N. K. Nikolova, "Near-field microwave imaging based on aperture raster scanning with TEM horn antennas," *IEEE Trans. Antennas Propag*., vol. 59, no. 3, pp. 928−940, Mar. 2011.

[4] M. Ravan, R. K. Amineh, and N. K. Nikolova, "Two-dimensional near-field microwave holography," *Inverse Problems*, vol. 26, no. 5, May. 2010.

[5] D. Kundur and D. Hatzinakos, "Blind image deconvolution," *IEEE Signal Proc. Mag.*, vol. 13, no. 3, pp. 43–64, May. 1996.
[6] G. R. Ayers and J. C. Dainty, "Iterative blind deconvolution method and its applications," *Optics Lett.*, vol. 13, no. 7, pp. 547–549, Jul. 1988.
[7] B. L. K. Davey, R. G. Lane, and R. H. T. Bates, "Blind deconvolution of noisy complex-valued image," *Optics Comm.*, vol. 69, no. 7, pp. 353–356, Jan. 1989.
[8] L. B. Lucy, "An iterative technique for the rectification of observed distributions," *Astron. J*. vol. 79, pp. 745–754, Jun, 1974.
[9] W. H. Richardson, "Bayesian-based iterative method of image restoration," *J. Opt. Soc*., vol 62, pp. 55–59, Jul. 1972.
[10] B. C. McCallum, "Blind deconvolution by simulated annealing," *Optics* Comm., vol. 75, no. 2, pp. 101–105, Feb. 1990.
[11] N. F. Law and R. G. Lane, "Blind deconvolution using least squares minimization," *Optics Communications*, vol 128, pp 341-352, Jul. 1996.
[12] http://www.mathworks.com/help/toolbox/images/ref/deconvwnr.html
[13] http://www.mathworks.com/help/toolbox/gads/simulannealbnd.html
[14] http://www.mathworks.com/help/techdoc/ref/fminsearch.html

CHAPTER 4

ACCELERATING SPACE MAPPING OPTIMIZATION WITH ADJOINT SENSITIVITIES

4.1 INTRODUCTION

Space mapping (SM) optimization aims at shifting the optimization burden from an expensive “fine” (or high-fidelity) model to a cheap “coarse” (or low-fidelity) model by iteratively optimizing and updating a surrogate. Utilizing a mapping between the parameter spaces of the coarse and fine models, the optimization iterates are guided in the fine-model space by very few fine-model simulations. In the field of microwave circuit design, SM usually exploits full-wave electromagnetic (EM) solvers as fine models while circuit-based CAD tools are utilized as coarse models [1], [2].

Several SM algorithms have been proposed since its inception in 1994 [1]. Aggressive SM (ASM) [2], [3] exploits a quasi-Newton iteration with the classical Broyden formula to estimate the mapping. Implicit space mapping (ISM) [4], [5] exploits pre-assigned parameters of the fine model. In ISM, an auxiliary set of parameters (e.g., dielectric constant of a substrate) is used to match the coarse model to the fine model. The coarse model is then calibrated by these parameters and re-optimized to predict a better fine-model design. Tuning SM (TSM) [6] integrates the engineering tuning concept into SM. Output SM (OSM) [4] introduces a transformation of the coarse-model response. OSM is usually used in the final stage when combined with other SM methods.

The theory of adjoint sensitivity analysis has been extended to electromagnetic solvers [7]-[9]. Using at most one extra EM simulation, we obtain the gradient of the fine-model response with respect to all design parameters regardless of their number. Adjoint sensitivity analysis can be implemented with different full-wave solvers. The self-adjoint sensitivity analysis (SASA) has the advantage of eliminating the extra adjoint EM simulation. It is applicable to network responses such as *S*-parameters [8].

In this thesis, we propose an algorithm for enhancing input SM optimization. Using the self-adjoint sensitivities supplied by the EM solver and the cheap response sensitivities of the coarse model, a mapping between the fine and coarse parameter spaces is accurately estimated. Results show that using available sensitivities dramatically decreases the number of iterations and, hence, the number of fine-model evaluations.

4.2 BACKGROUND

The input SM algorithm [1] aims at establishing a mapping between the design parameters of the coarse and fine models:

$$\boldsymbol{x}_c = \boldsymbol{B}\boldsymbol{x}_f + \boldsymbol{c} \tag{1}$$

such that

$$\left\| \boldsymbol{R}_c(\boldsymbol{x}_c) - \boldsymbol{R}_f(\boldsymbol{x}_f) \right\| \le \varepsilon . \tag{2}$$

Here, $\boldsymbol{x}_c$ and $\boldsymbol{x}_f$ are the coarse- and fine-model design or input parameters, respectively, and $\boldsymbol{R}_c$ and $\boldsymbol{R}_f$ are their corresponding responses. ε is a sufficiently small number. Once the mapping matrix $\boldsymbol{B}$ is obtained, an approximation of the fine-model optimal design is given by[1]

$$\boldsymbol{x}_c^* = \boldsymbol{B}^{(i)}\overline{\boldsymbol{x}}_f + \boldsymbol{c}^{(i)} \tag{3}$$

where $\boldsymbol{x}_c^*$ is the optimal coarse-model solution, $\boldsymbol{B}^{(i)}$ is the ith iteration mapping matrix, $\bar{\boldsymbol{x}}_f$ is an estimate of the optimal fine model, and $\boldsymbol{c}^{(i)}$ is the corresponding shift vector.

Input SM differs in the way $\boldsymbol{B}$ is estimated. In [1], two sets of points in the fine- and coarse-model parameter space are used to estimate the mapping parameters. This approach requires an overhead of expensive fine-model simulations. In [2], the so-called ASM algorithm was introduced. Here, $\boldsymbol{B}$ is updated at each iteration using the Broyden formula [10]. An initial guess is usually the identity matrix. If the two models are significantly misaligned, the algorithm may fail to give a good result. In [3], a trust region methodology is integrated with ASM. This approach limits the step taken in every iteration to guarantee the convergence of the algorithm. In ISM [5], the mapping is established inside the surrogate model.

In this thesis, we aim at integrating SM optimization with adjoint sensitivity analysis that has recently become available in commercial solvers, e.g., HFSS [11] and CST [12].

4.3 INTEGRATING SM AND SASA

Based on the concept of ISM, at iteration i, the surrogate model response can be defined as [5]

$$\boldsymbol{R}_s^{(i)}(\boldsymbol{x}_c) = \boldsymbol{R}_c^{(i)}(\boldsymbol{x}_c, \boldsymbol{p}^{(i)}) \tag{4}$$

where

$$\boldsymbol{p}^{(i)} = \arg\min_{\boldsymbol{p}} \left\| \boldsymbol{R}_f(\boldsymbol{x}_c^{*(i)}) - \boldsymbol{R}_c(\boldsymbol{x}_c^{*(i)}, \boldsymbol{p}) \right\| \tag{5}$$

$\boldsymbol{p}^{(i)}$ is a vector of preassigned parameters which are different from the optimizable parameters $\boldsymbol{x}_c$. These parameters are optimized to ensure a better match between the fine and surrogate model responses. $\boldsymbol{x}_c^{*(i)}$ is the optimum surrogate response using $\boldsymbol{p}^{(i-1)}$. The main drawback of this approach is the requirement of enough preassigned parameters to match the fine and surrogate model responses at each iteration which are not always available. Here we have a different approach both in using preassigned parameters and exploiting surrogate sensitivities. In this approach, by using Jacobian information, we establish a mapping between the input of the surrogate and fine models and we use preassigned parameters to match the responses of the surrogate and fine models.

Contrary to (5) our parameter extraction (PE) process is performed via

$$(\boldsymbol{x}_c^{(i)}, \boldsymbol{p}^{(i)}) = \arg \min_{(\boldsymbol{x}_c, \boldsymbol{p})} \left\| \boldsymbol{R}_f(\boldsymbol{x}_f^{(i)}) - \boldsymbol{R}_c(\boldsymbol{x}_c, \boldsymbol{p}) \right\| \tag{6}$$

where $\boldsymbol{x}_f^{(i)}$ and $\boldsymbol{R}_f(\boldsymbol{x}_f^{(i)})$ are the *i*th fine-model solution and fine-model response, respectively. The initial point for performing (6) is $(\boldsymbol{x}_c^{*(i-1)}, \boldsymbol{p}^{(i-1)})$. Using (6) allows more degrees of freedom for matching the responses in comparison with ISM. Based on [13], the Jacobians of the surrogate and fine-model responses at two corresponding points in the *i*th iteration are related by

$$\boldsymbol{J}_s(\boldsymbol{x}_c^{(i)})\boldsymbol{B}^{(i)} \cong \boldsymbol{J}_f(\boldsymbol{x}_f^{(i)}). \tag{7}$$

The Jacobian of the fine-model response is estimated using SASA. If not available, the Jacobian of the surrogate-model response is obtained through finite differences (FD). The latter computation is fast because the coarse model is much faster than the fine model. The linear input-mapping matrix is obtained by solving (7) as [13]

$$\boldsymbol{B}^{(i)} \cong \left(\boldsymbol{J}_s(\boldsymbol{x}_c^{(i)})^T \boldsymbol{J}_s(\boldsymbol{x}_c^{(i)})\right)^{-1} \boldsymbol{J}_s(\boldsymbol{x}_c^{(i)})^T \boldsymbol{J}_f(\boldsymbol{x}_f^{(i)}) \tag{8}$$

where $\boldsymbol{J}_s(\boldsymbol{x}_c^{(i)})$ is the Jacobian of the surrogate model. Then we re-optimize the new surrogate model to find

$$\boldsymbol{x}_c^{*(i)} = \arg\min_{\boldsymbol{x}} U(\boldsymbol{R}_s^{(i)}(\boldsymbol{x})) \tag{9}$$

where U is the given objective function. Finally, the fine-model solution is updated as:

$$\boldsymbol{x}_f^{(i+1)} = (\boldsymbol{B}^{(i)})^{-1}(\boldsymbol{x}_c^{*(i)} - \boldsymbol{x}_c^{(i)}) + \boldsymbol{x}_f^{(i)}. \tag{10}$$

If we denote the simulation response accuracy by δ_f, the termination criterion for the optimization is set as

$$\left\| \boldsymbol{R}_f(\boldsymbol{x}_f^{(i+1)}) - \boldsymbol{R}_s^{\,i}(\boldsymbol{x}_c^{*(i)}) \right\|_\infty \le \delta_f \tag{11}$$

where $\|\cdot\|_\infty$ is the infinite norm operator. One can terminate the program if $\boldsymbol{R}_f(\boldsymbol{x}_f^{(i+1)})$ satisfies the specifications but this may prevent the optimizer from reaching the best possible solution. The proposed algorithm can be summarized as follows:

Step 0: Obtain $\boldsymbol{x}_c^{*(0)}$ through (9) starting from $\boldsymbol{x}_c^{(0)}$, $\boldsymbol{p}^{(0)}$.

Step 1: Set $i = 1$, set $x_f^{(i)} = \boldsymbol{x}_c^{*(0)}$, obtain $\boldsymbol{R}_f(\boldsymbol{x}_f^{(i)})$ and obtain $\boldsymbol{J}_f(\boldsymbol{x}_f^{(i)})$ simultaneously using SASA.

Step 2: Find $\boldsymbol{x}_c^{(i)}$ and $\boldsymbol{p}^{(i)}$ using (6).

Step 3: If not available, obtain $\boldsymbol{J}_s(\boldsymbol{x}_c^{(i)})$ through finite difference approximation.

Step 4: Calculate $\boldsymbol{B}^{(i)}$ using (8).

Step 5: Obtain $\boldsymbol{x}_c^{*(i)}$ through (9).

Step 6: Find $\boldsymbol{x}_f^{(i+1)}$ using (10), set $i = i+1$.

Step 7: Obtain $\boldsymbol{R}_f(\boldsymbol{x}_f^{(i)})$ and obtain $\boldsymbol{J}_f(\boldsymbol{x}_f^{(i)})$ using SASA.

Step 8: If (11) is true, go to Step 9; else go to Step 2.

Step 9: Terminate.

4.4 VERIFICATION

Here, we consider an eight-section H-plane filter, an extended version of a design presented in [15]. The design specifications are:

$$|S_{11}| \le 0.16 \qquad 5.0 \text{ GHz} \le \omega \le 9.4 \text{ GHz}$$

$$|S_{11}| \ge 0.85 \qquad \omega \le 4.9 \text{ GHz}$$

$$|S_{11}| \ge 0.5 \qquad \omega \ge 9.8 \text{ GHz}$$

The fine model is an EM model simulated using HFSS ver. 13 on an X5670 3 GHz workstation with 48 GB of RAM. The simulation accuracy is set to 0.002 at 5.0 GHz with 50% mesh refinement. A magnetic wall is used (because of symmetry) to reduce the simulation time. The average simulation time is 240 minutes. As shown in Fig. 1, the coarse model is constructed by waveguide sections and inductances to model the septa. The *a* and *b* in Fig. 1 are the width and the height of the waveguide which are used as preassigned parameters. The values of the inductances are found from a simplified formula [16]. This coarse model is simulated using the model solver Agilent ADS [17]. We used the MATLAB optimization toolbox for parameter extraction (using *fminsearch*), direct optimization and re-optimizing the surrogate model (using *fminimax*).

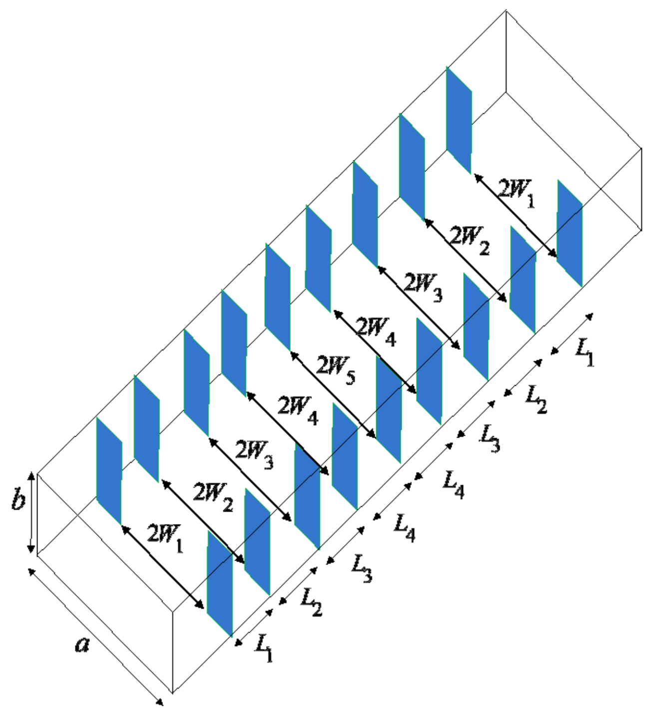

(a)

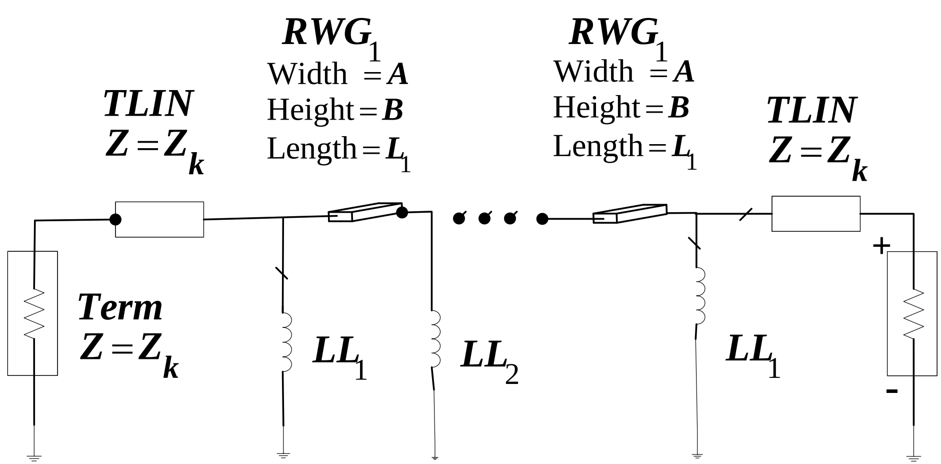

(b)

Fig. 1. The eight-section H-plane filter: (a) the fine model in HFSS with a =1.372 inch (3.48488 cm) and b = 0.622 inch (1.57988 cm); (b) the coarse model in Agilent ADS.

The initial design parameters $\boldsymbol{x}_c^{(0)}$ as well as the fine- and surrogate-model parameters obtained during the optimization processes, as well as the preassigned parameters, are shown in Tables I and II, respectively. Fig. 3 shows that our enhanced SM algorithm converges in fewer fine-model simulations than required by the other SM algorithms [18]. Direct optimization needs 19 fine-model evaluations to converge even though it uses SASA and starts from the optimum coarse model which is the best possible starting point. Fig. 4 shows a comparison of the new algorithm with direct optimization using SASA starting from different starting points.

TABLE I

Design Parameter Values during the Optimization Processes

(all values are in inches)

	$x_c^{(0)}$	$x_c^{*(0)}$ $(x_f^{(1)})$	$x_c^{*(1)}$	$x_f^{(2)}$	$x_c^{*(2)}$	$x_f^{(3)}$
W_1	0.5	0.57433	0.56723	0.53318	0.56278	0.53139
W_2	0.5	0.55880	0.56199	0.52337	0.56216	0.52243
W_3	0.5	0.54539	0.54984	0.50497	0.55107	0.50487
W_4	0.5	0.53965	0.54463	0.49759	0.54612	0.49720
W_5	0.5	0.53804	0.54317	0.49663	0.54505	0.49562
L_1	0.7	0.59479	0.69760	0.69200	0.75096	0.69930
L_2	0.7	0.63638	0.63286	0.63552	0.63490	0.63059
L_3	0.7	0.65139	0.65159	0.65101	0.65491	0.65051
L_4	0.7	0.65729	0 65833	0.65992	0.66130	0.65749

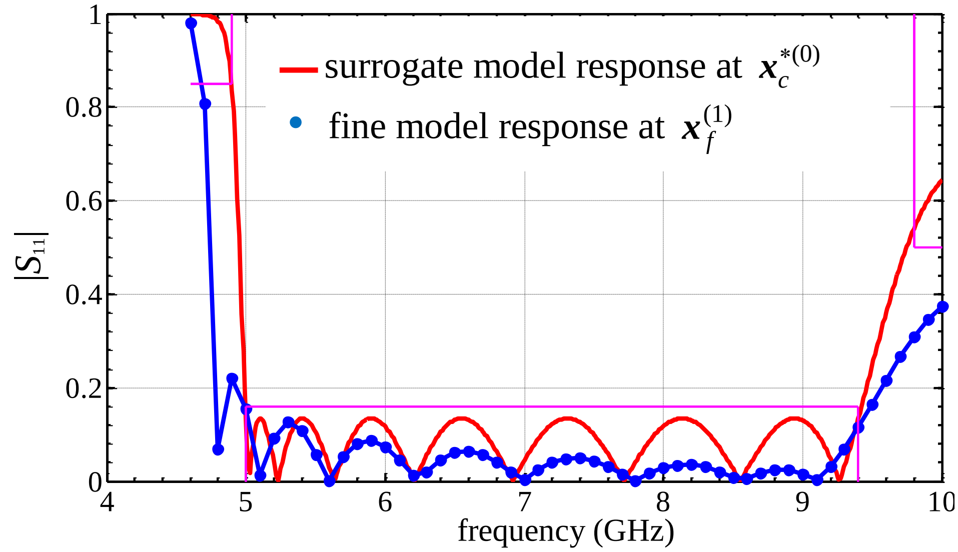

(a)

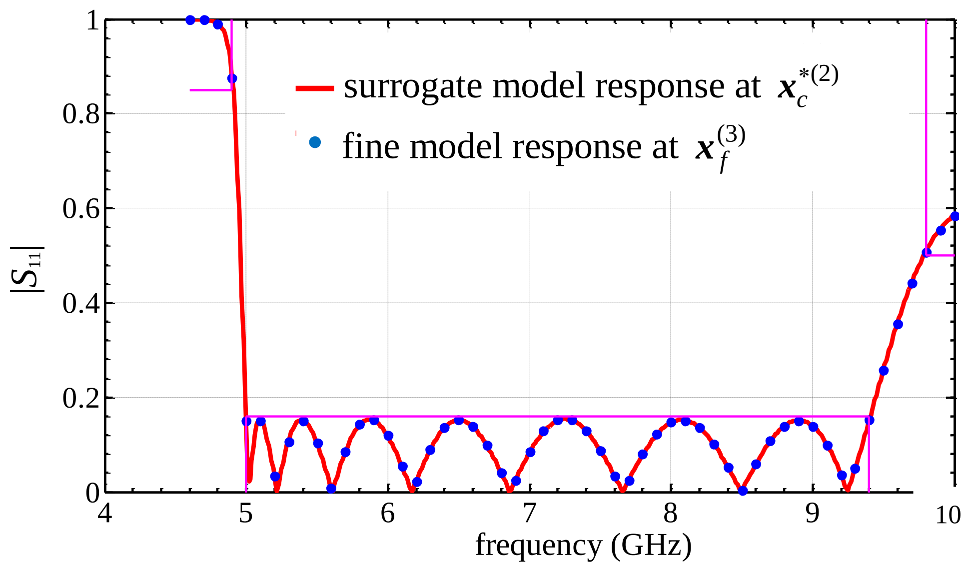

(b)

Fig. 2. The responses obtained during the optimization processes: (a) after 1st iteration; (b) after 2nd iteration. The horizontal purple lines show the specifications.

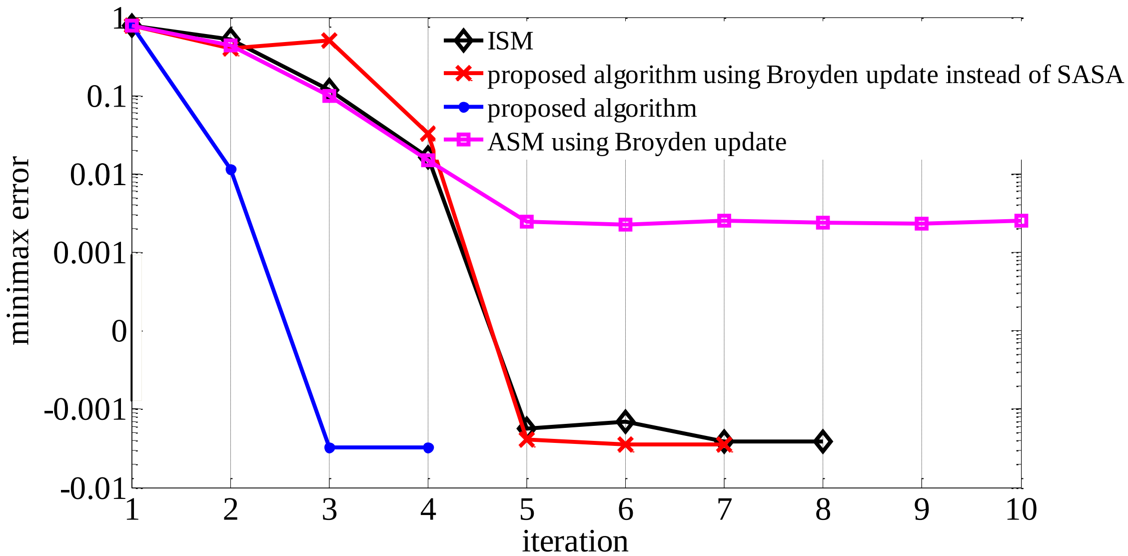

Fig. 3. Comparison of the proposed algorithm with other SM algorithms.

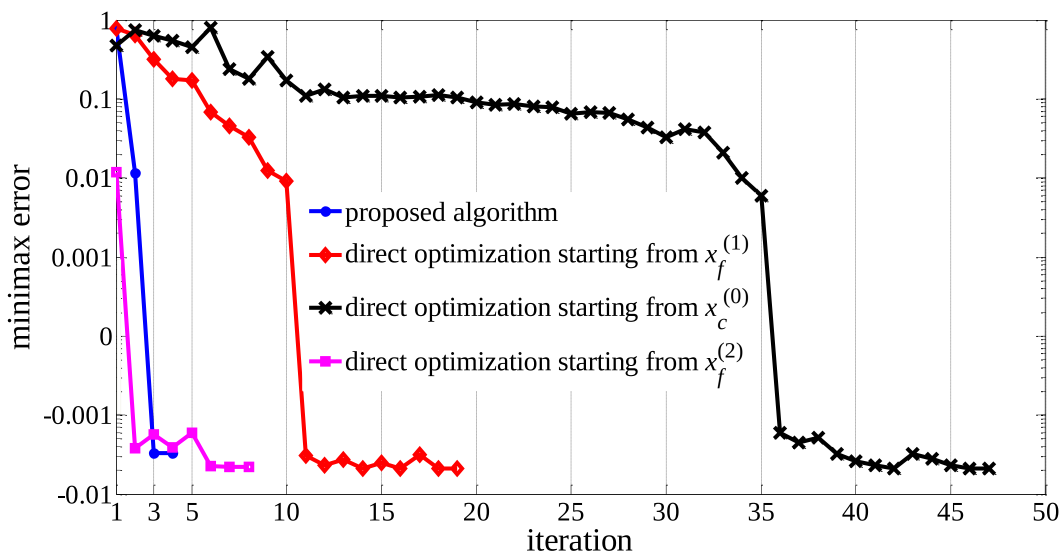

Fig. 4. Comparison of direct gradient optimization starting from different points with the proposed SM algorithm. One iteration corresponds to one fine- model evaluation.

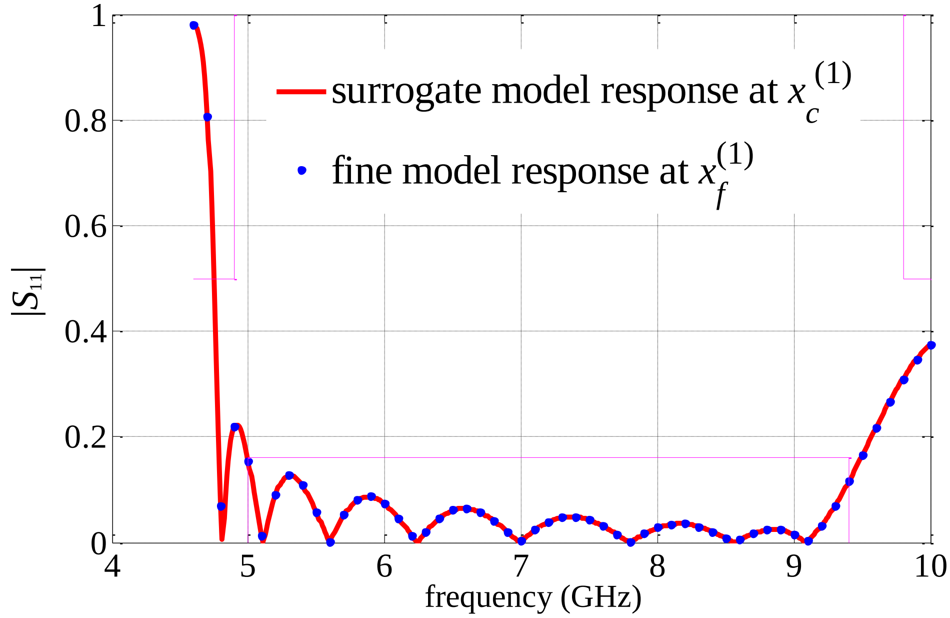

(a)

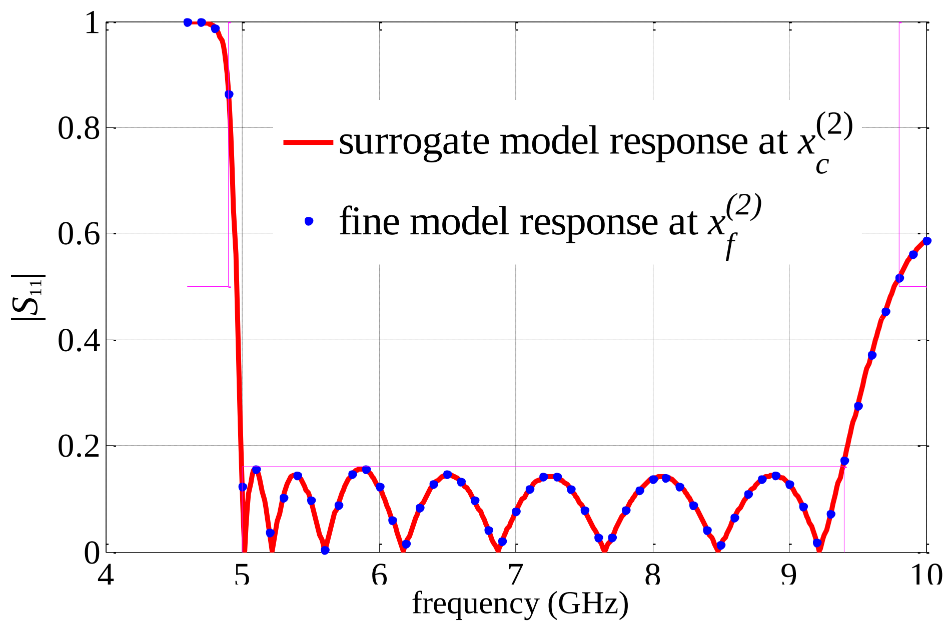

(b)

Fig. 5. Parameter extraction process: (a) after first iteration; (b) after second iteration. The horizontal purple lines show the specifications.

TABLE II

Preassigned Parameter Values (all values are in inches)

	a	b
$\boldsymbol{p}^{(0)}$	1.3720	0.6220
$\boldsymbol{p}^{(1)}$	1.3526	0.6778
$\boldsymbol{p}^{(2)}$	1.3333	0.7003

4.5 ADJOINT-ACCELERATED DESIGN FRAMEWORK FOR NOVEL MATERIALS IN MICROWAVE APPLICATIONS

Novel materials such as left-handed (LH) materials or so-called "metamaterials" are characterized by simultaneously negative permittivity and permeability. A large number of resonant-type LH materials, mostly realized by split-ring resonators (e.g., [19][21]) and transmission-line (TL) LH materials [22] have been proposed. These artificial materials have been employed in a number of applications like superlens for subdiffraction focusing, invisibility cloaks, etc.

Although fast analytical approaches have been presented to design many metamaterial structures, reliable synthesis of such materials still requires full-wave simulations. These simulations are expensive in terms of memory and time which makes metamaterial design a cumbersome task. This problem becomes even more acute in the synthesis of non-uniform metamaterial cells employed in the recently introduced transformation electromagnetics/optics (e.g., see [23]).

We propose a design framework to expedite the design of metamaterial structures. Our sensitivity-enabled framework implements a space-mapping algorithm as well as a direct-optimization algorithm. Our framework uses an accelerated space-mapping technique which expedites implicit/input space mapping by taking advantage of the coarse and fine model Jacobians.

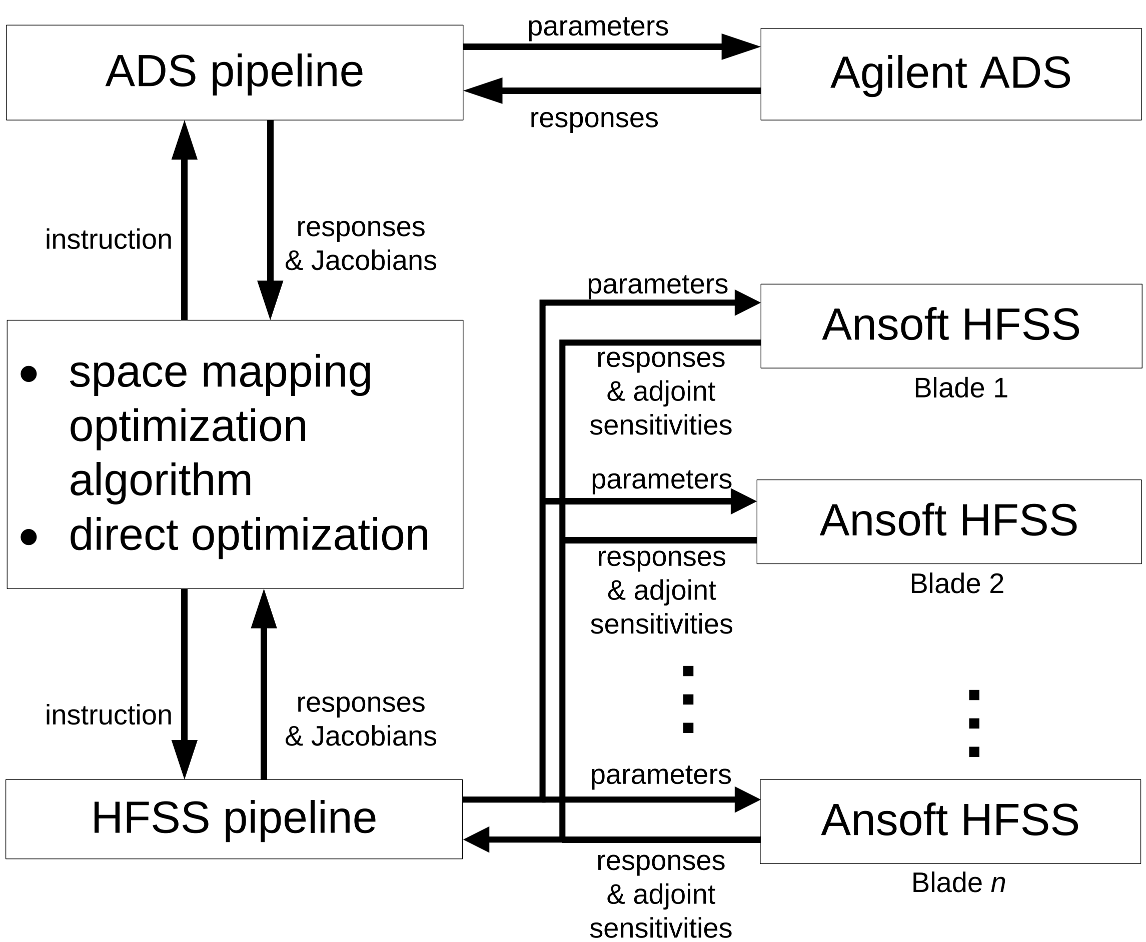

Fig. 6. Architecture of the implemented design framework.

We present the application of our framework to the design of the TL-based flat lens proposed in [24]. The design framework is implemented in MATLAB. The framework consists of space-mapping and direct optimization algorithms, an ADS pipeline, an HFSS pipeline and the Agilent ADS and Ansoft HFSS simulators. The algorithms send instructions and parameters to the ADS pipeline and collect data from it. The ADS pipeline follows the instructions to alter the structure of the ADS design and calls the Agilent ADS simulator. The ADS simulator writes responses to a file. The ADS pipeline picks up the responses and forwards them to the main algorithm. The ADS pipeline is also capable of creating Jacobians of an ADS model using finite differences. Similarly, the HFSS pipeline can alter the Ansoft HFSS structures, call the simulator and return the responses. Since the adjoint sensitivities are available in HFSS, they are fed to the main algorithm directly via the HFSS pipeline. We show in Fig. 6 the architecture of the implemented framework.

In the ADS pipeline, ADS generates a netlist.org file for a schematic file. This netlist file contains the design parameters, which can be changed. The simulation in ADS is called for the current design parameters by using the following command in MATLAB

system (‘hpeesofsim netlist.org’)

In the HFSS pipeline, to run HFSS through MATLAB, we export the script generated for a specific schematic. This script is then called through the following command in MATLAB:

System(‘hfss RunScriptAndExit script.vbs’).

The above command runs the script.vbs which starts the corresponding simulation in HFSS. We change the design parameters in script.vbs at each iteration.

For the parameter extraction process, the MATLAB function fminsearch is used. For direct optimization and re-optimizing the surrogate model, we use the fminimax function. The function utilizes the Jacobian of the objective function if supplied, otherwise it uses finite differences to approximate the Jacobian. In direct optimization, the exact Jacobian is available through adjoint sensitivity analysis. In surrogate re-optimization of the ADS model, finite differences are used.

The framework takes advantage of clustered blades which enable us to continue with direct optimization subroutines at any space-mapping iteration.

4.6 DESIGN OF TRANSMISSION LINE METAMATERIAL STRUCTURES

In this section, we employ the proposed SM optimization algorithm to re-design a TL metamaterial structure. In [24], a compact TL metamaterial superlens has been presented which has a refractive index of n = –1 around 1.5 GHz which is within its passband. Based on the theory presented in [24], the authors have shown that with this lens they can achieve a sub-diffraction limit resolution. This makes this lens suitable for applications requiring strongly confined electromagnetic radiation, such as high resolution biomedical imaging or non-destructive testing.

This metamaterial lens is constructed by loading a microstrip line periodically with spiral inductors and interdigital capacitors. Fig. 7(a) shows the patterns created on the microstrip line to create these loading elements. The simulated structure in HFSS includes four cells cascaded in the longitudinal direction (x-direction in Fig. 7). Perfect E

and H walls are applied to the top/bottom walls and the side walls, respectively, to create an infinitely large structure in the transverse direction. The shorting vias connecting the beginning and the end of the microstrip line to the upper E plane ensure elimination of the parallel-plate waveguide mode. Also, the center of each pad shown in Fig. 7(a) is connected to the lower E plane to create the required loading inductance combined with the spiral inductor. The evaluation of such model takes 3 to 10 hours on a Pentium 4 with CPU speed of 3 GHz and with a RAM of 32 GB.

To show the efficiency of designing this metamaterial lens with the proposed SM optimization, we first build a coarse model in ADS (Fig. 8). The coarse model consists of interdigital capacitor, spiral inductor, microstrip line and vias inserted on a substrate. To model the upper E plane, we inset transmission lines with the same length as in the HFSS model and with the free-space characteristic impedance. Then, these transmission lines are connected in parallel to the microstrip line with lumped inductors which model the vias connecting the microstrip line to the upper E plane at the beginning and the end of the structure. Since the structure is infinite in the transverse direction, the equivalent circuit model is left open in the transverse direction. The simulation time for this coarse model is negligible.

Since the emphasis here is on the design of metamaterial structures with SM optimization, we set our design specifications the same as presented in [24] while starting from a different solution. The specifications are:

$$\begin{array}{ll} |S_{21}| \geq -2 \text{ dB} & 1.45 \text{ GHz} \leq f \leq 1.65 \text{ GHz} \\ |S_{21}| \leq -8 \text{ dB} & f \leq 1.3 \text{ GHz} \ \text{ and } \ f \geq 1.9 \text{ GHz} \end{array} \tag{12}$$

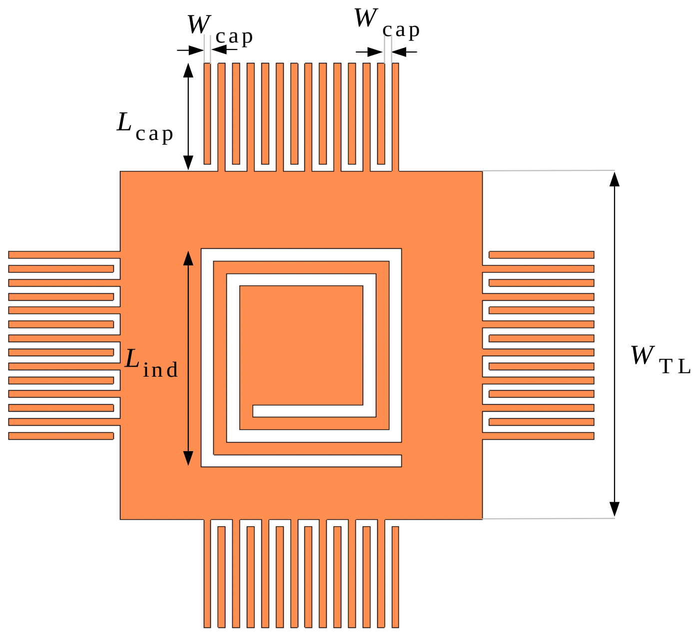

(a)

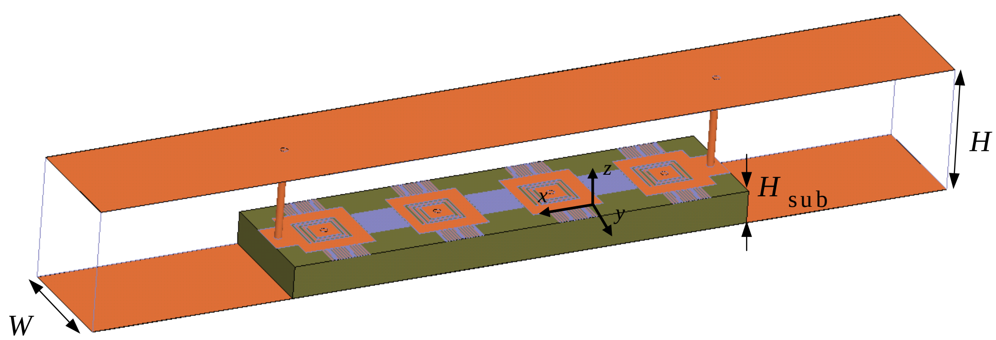

(b)

Fig. 7. (a) Unit cell design with spiral inductor and interdigital capacitor and (b) Simulation block for TL metamaterial lens.

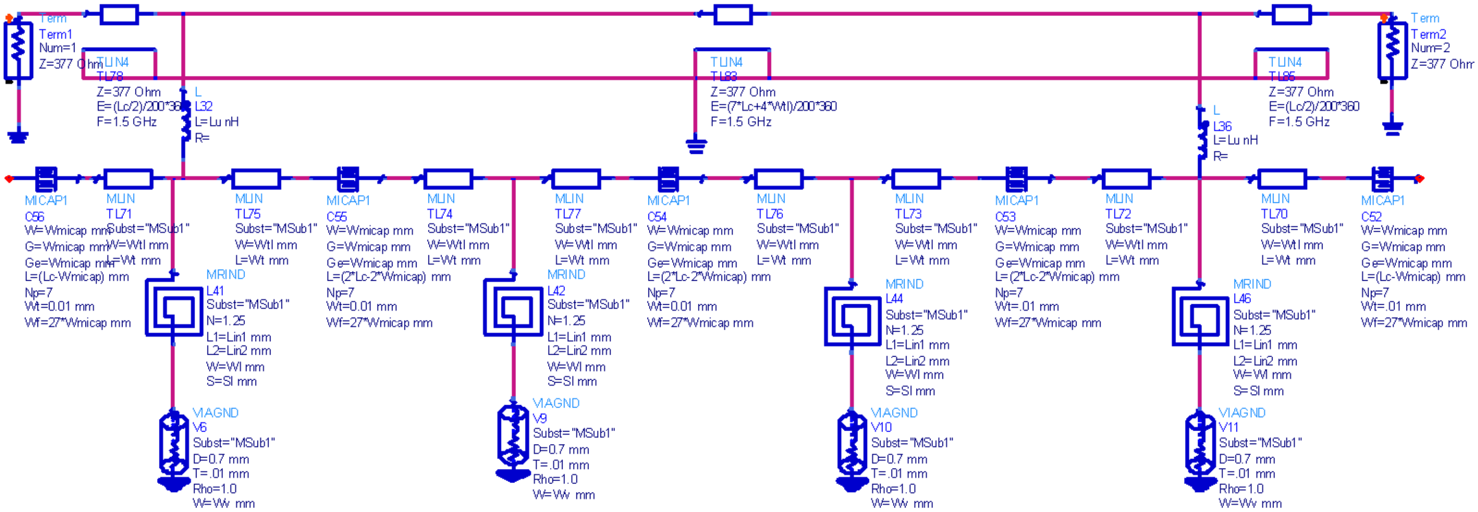

Fig. 8. Coarse model for the TL metamaterial lens shown in Fig. 1 as implemented in ADS.

TABLE III

Values of the Parameters in the Fine-model as Reported in [24]

Parameter	Value
Diameter of vias (mm)	0.7
W_{TL} (mm)	7
W (mm)	12
ε_r for substrate	2.2
tanδ for substrate	0.0009
H_{sub} (mm)	3.175
H (mm)	12

TABLE IV

Solutions Obtained During the Optimization Processes

Parameter	$\boldsymbol{x}_f^{(1)}$	$\boldsymbol{x}_f^{(2)}$	$\boldsymbol{x}_f^{(3)}$	$\boldsymbol{x}_d$
L_{ind} (mm)	4.20	5.00	4.40	4.57
W_{cap} (mm)	0.12	0.08	0.18	0.25
L_{cap} (mm)	1.60	2.20	2.30	2.16

TABLE V

Values of Implicit Parameters Obtained During the Optimization Process

Parameter	$i = 1$	$i = 2$	$i = 3$
L_{up} (nH)	6.60	5.90	5.75
W_{TL} (mm)	4.20	5.60	5.40
ε_r	3.00	4.20	4.21
H_{sub} (mm)	3.20	2.00	2.10

The design parameters are selected to be the length of the spiral inductor and the length and width of the interdigital capacitor's fingers, i.e, $\boldsymbol{x}_f = [L_{\text{ind}} \quad W_{\text{cap}} \quad L_{\text{cap}}]^T$. The implicit parameters that are employed to facilitate a better match between the coarse and fine models are the inductance of the upper vias L_{up}, the width of the microstrip lines W_{TL}, and the substrate permittivity ε_r and height H_{sub} in the coarse model, i.e., $\boldsymbol{p} = [L_{\text{up}} \quad W_{\text{TL}} \quad \varepsilon_r \quad H_{\text{sub}}]^T$.

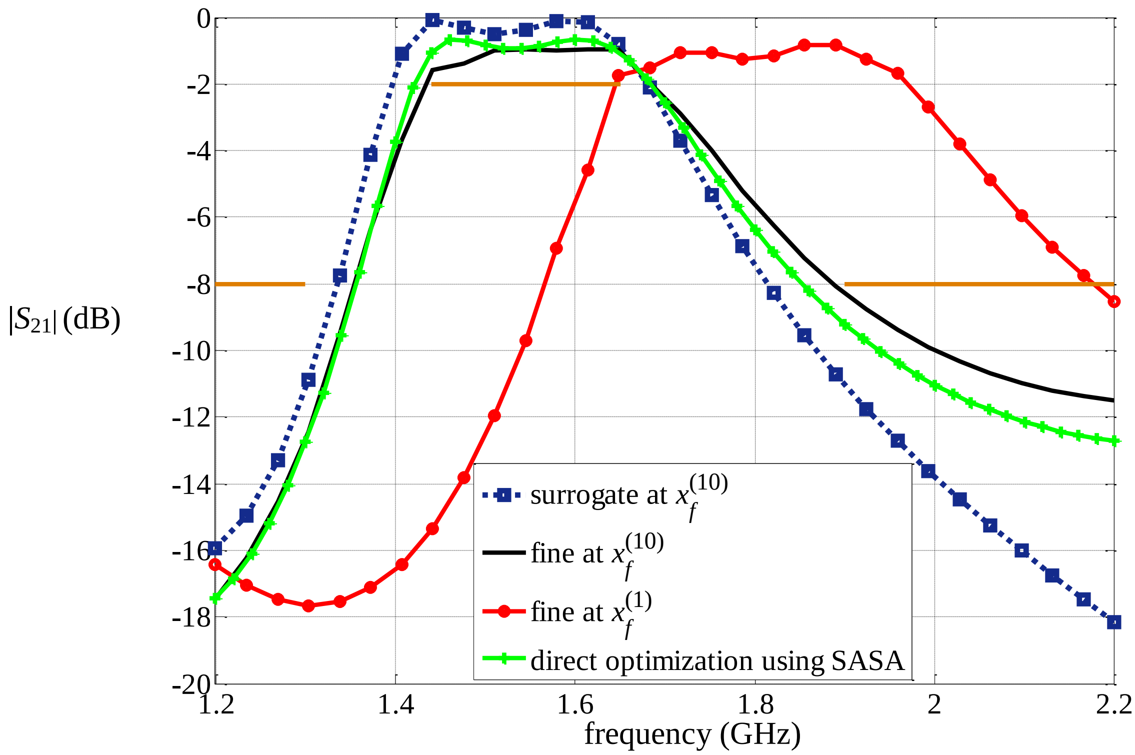

Fig. 9. Responses obtained during SM and direct optimization processes

At the initial point, the fine-model response, shown in Fig. 9, is unsatisfactory. The shape parameters and properties are $\boldsymbol{x}_f^{(1)} = [4.2 \quad 0.12 \quad 1.6]^T$, which are subject to optimization, the same as in [24]. TABLE III shows these values. The values of $\boldsymbol{x}_f^{(i)}$ and $\boldsymbol{p}^{(i)}$ obtained during the optimization process are shown in TABLE IV and TABLE V, respectively. After three fine model evaluations, the fine-model response satisfies the design specifications of (12).

Fig. 9 shows the optimal responses of the fine and surrogate model obtained at $\boldsymbol{x}_f^{(10)}$. This solution is very close to the values presented in [24], i.e., $[4.3 \quad 0.2 \quad 2.5]^T$ mm.

We also use our framework to perform direct optimization of the fine model with available HFSS adjoint sensitivities. For the direct fine-model optimization, we use the minimax algorithm from MATLAB optimization toolbox in conjunction with the Jacobian information provided by HFSS. The termination criteria for both algorithms are objective function change $\delta_f \leq 0.01$ and step size $\delta_x \leq 0.001$ mm. As is shown in Fig. 10, by starting from the same initial point, i.e., $\boldsymbol{x}_f^{(1)} = [4.2\ 0.12\ 1.6]^T$ mm, the direct fine-model optimization satisfies the specifications after four fine-model evaluations while the solution of the space mapping optimization satisfies the specifications in three iterations. The final solution of the direct fine-model optimization is $[4.57\ 0.25\ 2.16]^T$ mm.

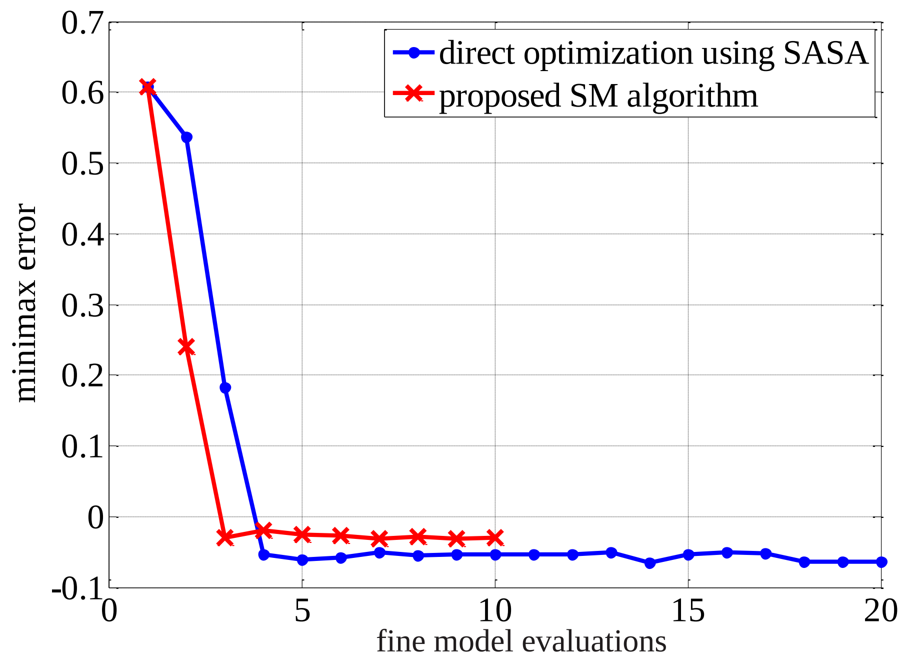

Fig. 10. Comparison of computed minimax cost function for SM optimization with the one obtained for the direct fine model optimization when employing sensitivity information for both.

4.7 CONCLUSION

We proposed an algorithm for the integration of sensitivity analysis with SM optimization. It is shown through an example that the number of fine-model evaluations is reduced compared to direct optimization, even when using Jacobian information in the direct optimization process and starting from the optimum coarse-model solution. The proposed algorithm also converges in fewer fine- model evaluations than other space-mapping methodologies. The availability of parallel processing makes the combination of space mapping and direct optimization more interesting as direct optimization can be performed by starting from different points obtained from space mapping optimization independently. We also present a sensitivity-enabled design framework. The framework features the adjoint-accelerated space mapping and direct optimization that utilize fine model adjoint sensitivity information. We use the framework to design a TL flat lens. This provides a fast and reliable tool to optimize the shape parameters of the novel structures

REFERENCES

[1] J. W. Bandler, R. M. Biernacki, S.H. Chen, P. A. Grobelny, and R. H. Hemmers, "Space mapping technique for electromagnetic optimization," *IEEE Trans. Microwave Theory Tech*., vol. 42, no. 12, pp. 2536–2544, Dec. 1994.

[2] J. W. Bandler, R. M. Biernacki, S.H. Chen, R.H. Hemmers, and K. Madsen, "Electromagnetic optimization exploiting aggressive space mapping," *IEEE Trans. Microwave Theory Tech*., vol. 43, no. 12, pp. 2874–2882, Dec. 1995.

[3] M. H. Bakr, J. W. Bandler, R. M. Biernacki, S. H. Chen, and K. Madsen, "A trust region aggressive space mapping algorithm for EM optimization," *IEEE Trans. Microwave Theory Tech*., vol. 46, no. 12, pp. 2412–2425, Dec. 1998.

[4] J. W. Bandler, Q. S. Cheng, D.H. Gebre-Mariam, K. Madsen, F. Pedersen, and J. Søndergaard, "EM-based surrogate modeling and design exploiting implicit, frequency and output space mappings," *IEEE MTT-S Int. Microwave Symp*. Dig., Philadelphia, PA, vol. 2, pp. 1003–1006, Jun. 2003.

[5] J. W. Bandler, Q. S. Cheng, N. K. Nikolova, and M. A. Ismail, "Implicit space mapping optimization exploiting preassigned parameters," *IEEE Trans. Microwave Theory Tech*., vol. 52, no. 1, pp. 378–385, Jan. 2004.

[6] S. Koziel, J. Meng, J. W. Bandler, M. H. Bakr, and Q. S. Cheng, "Accelerated microwave design optimization with tuning space mapping," *IEEE Trans. Microwave Theory Tech*., vol. 57, no. 2, pp. 383–394, Feb. 2009.

[7] N. K. Georgieva, S. Glavic, M. H. Bakr, and J. W. Bandler, "Feasible adjoint sensitivity technique for EM design optimization," *IEEE Trans. Microwave Theory Tech*., vol. 50, no. 12, pp. 2751–2758, Dec. 2002.

[8] N. K. Nikolova, J. Zhu, D. Li, M. H. Bakr, and J. W. Bandler, "Sensitivity analysis of network parameters with electromagnetic frequency domain simulators," *IEEE Trans. Microwave Theory Tech*., vol. 54, no. 2, pp. 670–681, Feb. 2006.

[9] N. K. Nikolova, X. Zhu, Y. Song, A. Hasib, and M. H. Bakr, "*S*-parameter sensitivities for electromagnetic optimization based on volume field solutions," *IEEE Trans. Microwave Theory Tech*., vol. 57, no. 6, pp. 1527–1538, June 2009.

[10] C.G. Broyden, "A class of methods for solving nonlinear simultaneous equations," *Math. Comp*., vol. 19, pp. 577–593, 1965.

[11] Ansoft Corporation, USA, *http://www.ansoft.com*.

[12] CST Corporation, USA, *http://www.cst.com*.

[13] M. H. Bakr, J. W. Bandler, N. Georgieva, and K. Madsen, "A hybrid aggressive space mapping algorithm for EM optimization," *IEEE Trans. Microwave Theory Tech*., vol. 47, no. 12, pp. 2440–2449, Dec. 1999.

[14] J. W. Bandler, R. M. Biernacki, S.H. Chen, P. A. Grobelny, and S. Ye, "Yield-driven electromagnetic optimization via multilevel multidimensional models," *IEEE Trans. Microwave Theory Tech*., vol. 41, no. 12, pp. 2269–2278, Dec. 1993.

[15] L. Young and B.M. Schiffman, "A useful high-pass filter design," *Microwave J.*, vol. 6, no. 2, pp. 78–80, Feb. 1963.

[16] N. Marcuvitz, *Waveguide Handbook.* 1st ed. New York: McGraw-Hill, pp. 221, 1951

[17] Agilent Technology, USA, *http://www.home.agilent.com*.

[18] J. W. Bandler, Q. S. Cheng, S. A. Dakroury, A.S. Mohamed, M. H. Bakr, K. Madsen, and J. Søndergaard, "Space mapping: the state of the art," *IEEE Trans. Microwave Theory Tech.,* vol. 52, no. 1, pp. 337–361, Jan. 2004.

[19] R. Simovski, P. A. Belov, and H. Sailing, "Backward wave region and negative material parameters of a structure formed by lattices of wires and split-ring resonators," *IEEE Trans. Antennas Propag.*, vol. 51, no. 10, pp. 2582–2591, Oct. 2003.

[20] E. Ozbay, K. Aydin, E. Cubukcu, and M. Bayindir, "Transmission and reflection properties of composite double negative metamaterials in free space," *IEEE Trans. Antennas Propag.*, vol. 51, no. 10, pp. 2592–2595, Oct. 2003.

[21] R. W. Ziolkowski and A. D. Kipple, "Application of double negative materials to increase the power radiated by electrically small antennas," *IEEE Trans. Antennas Propag.*, vol. 51, no. 10, pp. 2626–2640, Oct. 2003.

[22] C. Caloz and T. Itoh, *Electromagnetic Metamaterials: Transmission Line Theory and Microwave Applications*, John Wiley and Sons, Inc., 2006.

[23] D. Kwon and D. H. Warner, "Transformation electromagnetcis: an overview of the theory and applications," *IEEE Antennas and Propag. Mag.*, vol. 52, no. 1, pp. 24–46, Feb. 2010.

[24] J. Zhu and G. V. Eleftheriades, "Experimental verification of overcoming the diffraction limit with a volumetric Veselago-Pendry transmission line lens," *Phy. Rev. Lett.*, vol. 101, no. 1, pp. 013902-1–4, Jul. 2008.

CHAPTER 5

CONCLUSION AND FUTURE WORK

5.1 VECTORIAL 3D MICROWAVE HOLOGRAPHY

In this thesis, a vectorial 3D near-field microwave holography is proposed which is an improvement over the existing holography algorithms. This new algorithm allows for the processing of co- and cross- polarized field measurements. It is shown that in order to reconstruct correctly the shape and contrast-function distribution of an object this information is necessary.

It is possible to further improve the quality of the acquired images while retaining real-time performance by: (i) using chirp-pulse signals similar to chirp-pulse computed tomography, (ii) a hybrid algorithm which exploits both sensitivity-based detection and holography, (iii) modifying the algorithm to be applicable to detection of metallic objects, (iv) modifying the algorithm to be applicable to heterogeneous background, (v) considering the radiation pattern of the antennas, (vi) noise-cancelation algorithms.

Beside the possibilities to improve the quality of the holography algorithm, it is crucial to design new sensors which are more sensitive to the reflected signal. Without a decent reflection signal, as is mentioned in the thesis the algorithm does not perform well.

5.2 IMAGE QUALITY ENHANCEMENT IN MICROWAVE RASTER SCANNING TECHNIQUE

In this thesis, a simple and fast post-processing algorithm based on the principle of blind de-convolution is proposed for removing the integration effect of the antenna aperture. This allows for the data collected by the antennas to be used in 3D holography reconstruction. The blind deconvolution algorithm is a well-known algorithm in signal processing and our contribution here is its adaptation to microwave data processing.

For future investigation, finding robust methods, which do not need a time consuming simulation is needed for PSF estimation. Here, we use the simulation which may not exactly model the measurement setup very accurately. A possible way is to use the field distribution on the antenna aperture to estimate the PSF. This can be done with measurement at different frequencies using the electric field probes.

5.3 ACCELERATING SPACE MAPPING OPTIMIZATION WITH ADJOINT SENSITIVITIES

In this thesis, an algorithm which exploits the advantages of both the response sensitivities and space mapping is proposed. The algorithm uses the response sensitivities with respect to the design parameters and the implicit space mapping.

Further investigation on approximating the Hessian matrix through space mapping is needed. The Hessian of network parameters could also be efficiently estimated using space mapping and sensitivity analysis. In addition, a hybrid algorithm which exploits both space mapping and direct optimization is promising.

It is also a worthwhile to investigate response sensitivities in parameter extraction and in surrogate modeling.

On the application side, the design and the optimization of antennas and metamaterial structures deserve more investigation. Contrary to metamaterial structures, where a good coarse model is available, finding a good coarse model for antennas is still challenging. Developing 2D codes with approximations for the Green function of the medium and a coarse mesh may provide a solution.

APPENDIX

ITERATIVE BLIND DECONVOLUTION MATLAB CODE

% In this function you need to supply psf which is your initial guess, x which is your blurred data and an integer number for number of iteration (around 100). When you run the program it will give you *S* which is the unburned data and an integer number *r*. You have to run the program again and put m= r.

% Program

%%%%%%%%%%%%%%%%%%%%%%%%%%%%%%

% Iterative Blind Deconvolution

%%%%%%%%%%%%%%%%%%%%%%%%%%%%%%

```
function[r,S]=IBD(x,psf,m)
for i=1:m
psfnew=psf; % updating the PSF
S=direct(x,psfnew,1); % first deconvolution, direct function  is a direct deconvolution
S=S/norm(S); % normalizing the data
psf=direct(x,S,1); % second deconvolution
u(i)=[norm(conv2(psf,S)-x)]; % estimation of error
r=find(u==min(u)); % finding the best number of iterations
function J =direct(varargin) % this function is Wiener deconvolution from MATLAB
```

```
[I, PSF, ncorr, icorr, sizeI, classI, sizePSF, numNSdim] = ...
parseInputs(varargin{:});
H = psf2otf(PSF, sizeI);
if isempty(icorr)
   % noise-to-signal power ratio is given
   S_u = ncorr;
   S_x = 1;
   else
   % noise & signal frequency characteristics are given
   NSD = length(numNSdim);

   S_u = powerSpectrumFromACF(ncorr, NSD, numNSdim, sizePSF, sizeI);
   S_x = powerSpectrumFromACF(icorr, NSD, numNSdim, sizePSF, sizeI);
end
% Compute the denominator of G in pieces.
denom = abs(H).^2;
denom = denom .* S_x;
denom = denom + S_u;
clear S_u
denom = max(denom, sqrt(eps));
G = conj(H) .* S_x;
clear H S_x
G = G ./ denom;
clear denom
```

```
% Apply the filter G in the frequency domain.
J = ifftn(G .* fftn(I));
clear G
% If I and PSF are both real, then any nonzero imaginary part of J is due to
% floating-point round-off error.
if isreal(I) && isreal(PSF)
   J = real(J);
 end
% Convert to the original class
if ~strcmp(classI, 'double')
   J = changeclass(classI, J);
end;
%%%%%%%%%%%%%%%%%%%%%%%%%%%%%%%%%%%%%
nx=size(J);
np=size(PSF);
nm1=nx(1)-np(1)+1;
nm2=nx(2)-np(2)+1;
n1x=(nx(1)-nm1)/2;
n2x=(nx(2)-nm2)/2;
warning off
 J=J(n1x+1:n1x+nm1,n2x+1:n2x+nm2);
%============================================================
function S = powerSpectrumFromACF(ACF, NSD, numNSdim, sizePSF, sizeI)
sizeACF = size(ACF);
```

```
if (length(sizeACF)==2) && (sum(sizeACF==1)==1) && (NSD>1)
  ACF = createNDfrom1D(ACF,NSD,numNSdim,sizePSF);
end
% Calculate power spectrum
S = abs(fftn(ACF,sizeI));
%------------------------------------------------------------------
%====================================================================
function [I, PSF, ncorr, icorr, sizeI, classI, sizePSF, numNSdim] = ...
  parseInputs(varargin)
ncorr = 0;
icorr = [];
iptchecknargin(2,4,nargin,mfilename);
input_names={'PSF','NCORR','ICORR'};
I = varargin{1};%       deconvwnr(A,PSF)
PSF = varargin{2};
switch nargin
 case 3,%              deconvwnr(A,PSF,nsr)
  ncorr = varargin{3};
 case 4,%              deconvwnr(A,PSF,ncorr,icorr)
  ncorr = varargin{3};
  icorr = varargin{4};
end
% Third, Check validity of the input parameters:
% Input image I
```

```
sizeI = size(I);
classI = class(I);
% iptcheckinput(I,{'uint8','uint16','int16','double','single'},{'real' ...
%                   'finite'},mfilename,'I',1);
if prod(sizeI)<2,
   eid = sprintf('Images:%s:mustHaveAtLeast2Elements',mfilename);
   error(eid,'In function %s, input image must have at least two elements.', ...
        mfilename);
elseif ~isa(I,'double')
   I = im2double(I);
end

% PSF array
sizePSF = size(PSF);
if prod(sizePSF)<2,
   eid = sprintf('Images:%s:mustHaveAtLeast2Elements',mfilename);
   error(eid,'In function %s, PSF must have at least two elements.', ...
        mfilename);
elseif all(PSF(:)==0),
   eid = sprintf('Images:%s:psfMustNotBeZeroEverywhere',mfilename);
   error(eid,'In function %s, PSF cannot be zero everywhere.', ...
        mfilename);
end
% NSR, NCORR, ICORR
```

```
if isempty(ncorr) && ~isempty(icorr),

   eid = sprintf('Images:%s:invalidInput',mfilename);

   error(eid, ...

        'Invalid input in function %s: provide characteristics for noise.', ...

        mfilename);

end


% Sizes: PSF size cannot be larger than the image size in non-singleton dims

[sizeI, sizePSF, sizeNCORR] = padlength(sizeI, sizePSF, size(ncorr));

numNSdim = find(sizePSF~=1);

if any(sizeI(numNSdim) < sizePSF(numNSdim))

   eid = sprintf('Images:%s:psfMustBeSmallerThanImage',mfilename);

   error(eid, ...

        'In function %s, size of the PSF must not exceed the image size in any nonsingleton
dimension.', mfilename);

end

if isempty(icorr) && (prod(sizeNCORR)>1) && ~isequal(sizeNCORR,sizeI)

   eid = sprintf('Images:%s:nsrMustBeScalarOrArrayOfSizeA',mfilename);

   error(eid, ...

        'DECONVWNR(A,PSF,NSR): NSR has to be a scalar or an array of size A.');

end

%----------------------------------------------------------------------

function f = createNDfrom1D(ACF,NSD,numNSdim,sizePSF)

cntr = ceil(length(ACF)/2);%location of the ACF center
```

```
vec = (0:(cntr-1))/(cntr-1);
[x,y] = meshgrid(vec,vec);% grid for the quarter
   % 2. Calculate radius vector to each grid-point and number the points
% above the diagonal in order to use them later for ACF interpolation.
radvect = sqrt(x.^2+y.^2);
nums = [1;find(triu(radvect)~=0)];
% 3. Interpolate ACF at radius-vector distance for those points.
acf1D = ACF(cntr-1+[1:cntr cntr]);% last point is for the corner.
radvect(nums) = interp1([vec sqrt(2)],acf1D,radvect(nums));
% 4. Unfold 45 degree triangle to a square, and then the square
% quarter to a full square matrix.
radvect = triu(radvect) + triu(radvect,1).';
acf = radvect([cntr:-1:2 1:cntr],[cntr:-1:2 1:cntr]);

% Second, once 2D is ready, extrapolate 2D-ACF to NSD-ACF
if NSD > 2,% that is create volumetric ACF
  idx0 = repmat({':'},[1 NSD]);
  nextDimACF = [];
  for n = 3:NSD,% make sure not to exceed the PSF size
    numpoints = min(sizePSF(numNSdim(n)),length(ACF));
    % and take only the central portion of 1D-ACF
    vec = cntr-ceil(numpoints/2)+(1:numpoints);
    for m = 1:numpoints,
      idx = [idx0(1:n-1),{m}];
```

```
        nextDimACF(idx{:}) = ACF(vec(m))*acf; %#ok<AGROW>
      end;
      acf = nextDimACF;
    end
end
% Third, reshape NSD-ACF to the right dimensions to include PSF
% singletons.
idx1 = repmat({1},[1 length(sizePSF)]);
idx1(numNSdim) = repmat({':'},[1 NSD]);
f(idx1{:}) = acf;
%------------------------------------------------------------------
function varargout = padlength(varargin)
numDims = zeros(nargin, 1);
for k = 1:nargin
  numDims(k) = length(varargin{k});
end
numDims = max(numDims);
limit = max(1,nargout);
varargout = cell(1,limit);
for k = 1 : limit
  varargout{k} = [varargin{k} ones(1,numDims-length(varargin{k}))];
end
```

BIBLIOGRAPHY

[1] P. Neittaanmaki, M. Rudnicki, and A. Savini, *Inverse Problems and Optimal Design in Electricity and Magnetism*. Clarendon Press, Oxford, 1996.

[2] D. M. Parkin, F. Bray, J. F. And, and P. Pisani, “Global cancer statistics, 2002,” *CA: A Cancer J. Clinicians*, vol. 55, pp. 74–108, Mar. 2005.

[3] C. H. Jones, “Methods of breast imaging,” *Phys. Med. Biol.*, vol. 27, pp. 463–499, Apr. 1982.

[4] M. Säbel and H. Aichinger, “Recent developments in breast imaging,” *Phys. Med. Biol.*, vol. 41, pp. 315–368, Mar. 1996.

[5] P. T. Huynh, A. M. Jarolimek, and S. Daye, “The false-negative mammogram,” *Radiographics*, vol. 18, pp. 1137–1154, Sep. 1998.

[6] E. C. Fear, S. C. Hagness, P. M. Meaney, M. Okoniewski, and M. A. Stuchly, “Enhancing breast tumor detection with near-field imaging,” *IEEE Microwave Magazine*, vol. 3, no. 1, pp. 48−56, Mar. 2002.

[7] J. H. Jacobi, L. E. Larsen, and C. T. Hast, “Water-immersed microwave antennas and their application to microwave interrogation of biological targets,” *IEEE Trans. Microwave Theory Tech.*, vol. MTT-27, no. 1, pp. 70–78, Jan. 1979.

[8] L. E. Larsen and J. H. Jacobi, “Microwave scattering parameter imagery of an isolated canine kidney,” *Med. Phys.*, vol. 6, pp. 394–403, 1979.

[9] A. J. Devaney, “Reconstructive tomography with diffracting wave-fields,” *Inv. Problems*, vol. 2, no. 2, pp. 161–183, May 1986.

[10] R. Aitmehdi, A. P. Anderson, S. Sali, and M. Ferrando, “The determination of dielectric loss tangent by microwave phase tomography,” *Inv. Problems*, vol. 4, no. 2, pp. 333–345, May 1988.

[11] M. Slaney, A. C. Kak, and L. E. Larsen, “Limitations of imaging with first order diffraction tomography,” *IEEE Trans. Microwave Theory Tech.*, vol. 32, no. 8, pp. 860–873, Aug. 1984.

[12] J. C. Bolomey, C. Pichot, and G. Gaboriaud, “Planar microwave camera for biomedical applications: Critical and prospective analysis of reconstruction algorithms,” *Radio Sci.*, vol. 26, no. 2, pp. 541–549, Apr. 1991.

[13] A. Fhager and M. Persson, “Comparison of two image reconstruction algorithms for microwave tomography,” *Radio Sci.*, vol. 40, no. 3, Jun. 2005.

[14] A. Abubakar, P. M. van den Berg, and J. J. Mallorqui, “Imaging of biomedical data using a multiplicative regularized contrast source inversion method,” *IEEE Trans. Microwave Theory Tech.*, vol. 59, no. 7, pp. 1761–1771, Jul. 2002.

[15] R. E. Kleinman and P. M. van den Berg, “A modified gradient method for two-dimensional problems in tomography,” *J. Comput. Appl. Math.*, vol. 42, no. 1, pp. 17–35, Sep. 1992.

[16] W. C. Chew and Y. M.Wang, “Reconstruction of two-dimensional permittivity distribution using the distorted born iterative method,” *IEEE Trans. Med. Imag.*, vol. 9, no. 2, pp. 218–225, Jun. 1990.

[17] A. E. Bulyshev, A. E. Souvorov, S. Y. Semenov, V. G. Posukh, and Y. E. Sizov, “Three-dimensional vector microwave tomography: Theory and computational experiments,” *Inv. Problems*, vol. 20, no. 4, pp. 1239–1259, Aug. 2004.
[18] A. Abubakar and P. M. van den Berg, “Iterative forward and inverse algorithms based on domain integral equations for three-dimensional electric and magnetic objects,” *J. Comput. Phys.*, vol. 195, no. 1, pp. 236–262, Mar. 2004.
[19] Z. Q. Zhang and Q. H. Liu, “Three-dimensional nonlinear image reconstruction for microwave biomedical imaging,” *IEEE Trans. Biomed. Eng.*, vol. 51, no. 3, pp. 544–548, Mar. 2004.
[20] Q. Fang, P. M. Meaney, S. D. Geimer, A. V. Streltsov, and K. D. Paulsen, “Microwave image reconstruction from 3D fields coupled to 2D parameter estimation,” *IEEE Trans. Med. Imag.*, vol. 23, no. 4, pp. 475–484, Apr. 2004.
[21] S. Y. Semenov, A. E. Bulyshev, A. Abubakar, V. G. Posukh, Y. E. Sizov, A. E. Souvorov, P. M. van den Berg, and T. C. Williams, “Microwave-tomographic imaging of high dielectric-contrast objects using different image-reconstruction approaches,” *IEEE Trans. Microwave Theory Tech.*, vol. 53, no. 7, pp. 2284–2295, Jul. 2005.
[22] T. Isernia, V. Pascazio, and R. Pierri, “On the local minima in a tomographic imaging technique,” *IEEE Trans. Geosci. Remote Sens.*, vol. 39, no. 7, pp. 1596–1607, Jul. 2001.
[23] R. Benjamin, “Synthetic, post-reception focusing in near-field radar,” *Proc. EUREL Int. Conf. on the Detection of Abandoned Land Mines: A Humanitarian Imperative Seeking a Tech. Solution*, pp. 133–137, Oct 1996.
[24] R. Benjamin, “Detecting reflective object in reflective medium,” U.K. GB 2313969, Dec. 1997.
[25] S. C. Hagness, A. Taflove, and J. E. Bridges, “Two-dimensional FDTD analysis of a pulsed microwave confocal system for breast cancer detection: Fixed-focus and antenna-array sensors,” *IEEE Trans. Biomed. Eng.*, vol. 45, pp. 1470–1479, Dec. 1998.
[26] E. C. Fear and M. A. Stuchly, “Microwave system for breast tumor detection,” *IEEE Microwave Wireless Compon. Lett.*, vol. 9, pp. 470–472, Nov. 1999.
[27] L. Xu, S. K. Davis, S. C. Hagness, D. W. van der Weide, and B. D. Van Veen, “Microwave imaging via space-time beamforming: Experimental investigation of tumor detection in multilayer breast phantoms,” *IEEE Trans. Microwave Theory Tech.*, vol. 52, pt. Part 2, pp. 1856–1865, Aug. 2004.
[28] E. J. Bond, L. Xu, S. C. Hagness, and B. D. Van Veen, “Microwave imaging via space-time beamforming for early detection of breast cancer,” in *Proc. IEEE Int. Conf. on Acoust., Speech, and Signal Process. (ICASSP ’02)*, vol. 3, pp. 2909–2912, May 2002.
[29] Y. Xie, B. Guo, L. Xu, J. Li, and P. Stoica, “Multi-static adaptive microwave imaging for early breast cancer detection,” in *Proc. 39th Asilomar Conf. on Signals, Syst. and Comput.*, pp. 285–289, Nov. 2005.
[30] M. Klemm, I. J. Craddock, J. A. Leendertz, A. Preece, and R. Benjamin “Radar-based breast cancer detection using a hemispherical antenna array-experimental

results” *IEEE Trans. Antennas and Propag.*, vol. 57, no. 6, pp. 1692–1704, Jun. 2009.
[31] E. C. Fear, J. Sill, and M. A. Stuchly, “Experimental feasibility study of confocal microwave imaging for breast tumor detection,” *IEEE Trans. Microw. Theory Tech.*, vol. 51, pp. 887–892, Mar. 2003.
[32] J. M. Sill and E. C. Fear, “Tissue sensing adaptive radar for breast cancer detection—experimental investigation of simple tumor models,” *IEEE Trans. Microwave Theory Tech.*, vol. 53, pp. 3312–3319, Nov. 2005.
[33] D. M. Sheen, D. L. McMakin, and T. E. Hall, “Three-dimensional millimeter-wave imaging for concealed weapon detection,” *IEEE Trans. Microw. Theory Tech.*, vol. 49, no. 9, pp. 1581−1592, Sep. 2001.
[34] D. M. Sheen, D. L. McMakin, and T. E. Hall, “Near field imaging at microwave and millimeter wave frequencies,” *IEEE/MTT-S Int. Microwave Symp.*, pp. 1693−1696, Jun. 2007.
[35] M. Ravan, R. K. Amineh, and N. K. Nikolova, “Two-dimensional near-field microwave holography,” *Inverse Problems*, vol. 26, no. 5, May. 2010.
[36] M. Ravan, R. K. Amineh, and N. K. Nikolova, “Microwave holography for near-field imaging,” *IEEE AP-S/URSI Int. Symp. on Antennas and Propagation*, July 2010.
[37] M. Ravan, R. K. Amineh, and N. K. Nikolova, “Near-field microwave holographic imaging: target localization and resolution study,” *XX URSI Comm. B Int. Symp. on Electromagnetic Theory* (EMT-S 2010), Aug. 2010.
[38] R. K. Amineh, M. Ravan, A. Khalatpour, and N. K. Nikolova, “Three-dimensional near-field microwave holography using reflected and transmitted signals,” accepted for publication in *IEEE Trans. Antennas Propag.*
[39] N. H. Farhat and W. R. Guard, “Millimeter wave holographic imaging of concealed weapons,” *Proc. of the IEEE*, vol. 59, pp. 1383−1384, 1971.
[40] D. Slater, *Near-Field Antenna Measurements*, Artech House, Boston, 1991.
[41] M. Elsdon, M. Leach, S. Skobelev, and D. Smith, “Microwave holographic imaging of breast cancer,” *IEEE Int. Symp. on Microwave, Antenna, Propag., and EMC Tech. For Wireless Commun.*, pp. 966−969, Aug. 2007.
[42] Tank spray on foam insulation (SOFL) using synthetic aperture focusing techniques,” (SAFT) *Review of Quantitative Nondestructive Evaluation*, vol. 25, pp. 1546−1553, 2006.
[43] R. K. Amineh, M. Ravan, A. Trehan, and N. K. Nikolova, “Near-field microwave imaging based on aperture raster scanning with TEM horn antennas,” *IEEE Trans. Antennas Propag.*, vol. 59, no. 3, pp. 928−940, Mar. 2011.
[44] R. K. Amineh, A. Khalatpour, and N. K. Nikolova, “Three-dimensional near-field microwave holography using co-polarized and cross-polarized data,” submitted to *IEEE Antennas Wireless Propag. Lett.*
[45] A. Khalatpour, R. K. Amineh, and N. K. Nikolova, “Image quality enhancement in the microwave raster scanning method accepted for the presentation at the *IEEE MTT-S Int. Microwave Symposium* 2011, June 2011

[46] D. Kundur and D. Hatzinakos, “Blind image deconvolution,” *IEEE Signal Proc. Mag.*, vol. 13, no. 3, pp. 43–64, May. 1996.
[47] G. R. Ayers and J. C. Dainty, “Iterative blind deconvolution method and its applications,” *Optics Lett.*, vol. 13, no. 7, pp. 547–549, July. 1988.
[48] B. L. K. Davey, R. G. Lane, and R. H. T. Bates, “Blind deconvolution of noisy complex-valued image,” *Optics Comm.*, vol. 69, no. 7, pp. 353–356, Jan. 1989.
[49] B. C. McCallum, “Blind deconvolution by simulated annealing,” *Optics Comm.*, vol. 75, no. 2, pp. 101–105, Feb. 1990.
[50] J. W. Bandler, “Optimization methods for computer-aided design,” *IEEE Trans. Microwave Theory Tech.*, vol. 17, no. 8, pp. 533–525, Aug. 1969.
[51] J. W. Bandler, “Computer optimization of microwave circuits,” *Proc. European Microwave Conf.*, Stockholm, Sweden, pp. B8/S: 1S: 8, Aug. 1971.
[52] M. B. Steer, J. W. Bandler, and C. M. Snowden, “Computed-aided design of RF and microwave circuits and systems,” *IEEE Trans. Microwave Theory Tech.*, vol. 50, no. 3, pp. 996–1005, Mar. 2002.
[53] D. M. Pozar, *Microwave Engineering*, Wiley, Hoboken, NJ, 2005. D.G.
[54] *Ansoft Corporation*, http://www.ansoft.com.
[55] Agilent ADS 2005A, *Agilent Technologies*, 1400 Fountain grove Parkway, Santa Rosa, CA 95403–1799, USA.
[56] J. W. Bandler and S. H. Chen, “Circuit optimization: the state of the art,” *IEEE Trans. Microwave Theory Tech.*, vol. 36, no. 2, pp. 424– 443, Feb. 1998.
[57] J. W. Bandler, W. Kellermann, and K. Madsen, “A superlinearly convergent minimax algorithm for microwave circuit design,” *IEEE Trans. Microwave Theory Tech.*, vol. *MTT*-33, no. 12, pp. 1519–1530, Dec. 1985.
[58] J. W. Bandler, S. H. Chen, S. Daijavad, and K. Madsen, “Efficient optimization with integrated gradient approximations,” *IEEE Trans. Microwave Theory Tech.*, vol. 36, no. 2, pp. 444–455, Feb. 1988.
[59] J. W. Bandler, R. M. Biernacki, S. H. Chen, P. A. Grobelny, and R.H. Hemmers, “Space mapping technique for electromagnetic optimization,” *IEEE Trans. Microwave Theory Tech.*, vol. 42, no. 12, pp. 2536–2544, Dec. 1994.
[60] J. W. Bandler, Q. S. Cheng, S. A. Dakroury, A. S. Mohamed, M. H. Bakr, K. Madsen, and J. Søndergaard, “Space mapping: the state of the art,” *IEEE Trans. Microwave Theory Tech.*, vol. 52, no. 1, pp. 337–361, Jan. 2004.
[61] S. Koziel and J. W. Bandler, *International Journal of Numerical Modeling*, vol. 23, no. 6, pp. 425–446, Nov 2010.
[62] N. K. Nikolova, J. Zhu, D. Li, M. H. Bakr, and J. W. Bandler, “Sensitivity analysis of network parameters with electromagnetic frequency domain simulators,” *IEEE Trans. Microwave Theory Tech.*, vol. 54, no. 2, pp. 670–681, Feb. 2006.
[63] A. Khalatpour, R. K. Amineh, Q. S. Cheng, M. H. Bakr, N. K. Nikolova, and J. W. Bandler, “Accelerating space mapping optimization with adjoint sensitivities,” *IEEE Microw.Wireless Compon. Lett.*, vol. 21, no. 6, pp. 280–282, June 2011.

[64] M. H. Bakr, J. W. Bandler, N. Georgieva, and K. Madsen, "A hybrid aggressive space-mapping algorithm for EM optimization," *IEEE Trans. Microwave Theory Tech*., vol. 47, no. 12, pp. 2440–2449, Dec. 1999.
[65] A. Khalatpour, R. K. Amineh, N. K. Nikolova, and J. W. Bandler, "Adjoint-Accelerated design framework for novel materials in microwave applications," accepted for the presentation at the 41st *European Microwave Conference,* Oct. 2011.
[66] W. Chew*, Waves and Fields in Inhomogeneous media*, Piscataway, NJ: IEEE Press, 1995.
[67] EM software & systems-S.A. (Pty) Ltd., http://www.feko.info
[68] R. Zoughi, *Microwave Non-destructive Testing and Evaluation,* Kluwer Academic Publishers, 2000.
[69] L. B. Lucy, "An iterative technique for the rectification of observed distributions," *Astron. J*. vol. 79, pp. 745–754, Jun, 1974.
[70] W. H. Richardson, "Bayesian-based iterative method of image restoration," *J. Opt. Soc*., vol 62, pp. 55–59, Jul. 1972.
[71] N. F. Law and R. G. Lane, "Blind deconvolution using least squares minimization," *Optics Communications*, vol 128, pp 341-352, Jul. 1996.
[72] http://www.mathworks.com/help/toolbox/images/ref/deconvwnr.html
[73] http://www.mathworks.com/help/toolbox/gads/simulannealbnd.html
[74] http://www.mathworks.com/help/techdoc/ref/fminsearch.html
[75] N. K. Georgieva, S. Glavic, M. H. Bakr, and J. W. Bandler, "Feasible adjoint sensitivity technique for EM design optimization," *IEEE Trans. Microwave Theory Tech*., vol. 50, no. 12, pp. 2751–2758, Dec. 2002.
[76] N. K. Nikolova, X. Zhu, Y. Song, A. Hasib, and M. H. Bakr, "*S*-parameter sensitivities for electromagnetic optimization based on volume field solutions," *IEEE Trans. Microwave Theory Tech*., vol. 57, no. 6, pp. 1527–1538, June 2009.
[77] C.G. Broyden, "A class of methods for solving nonlinear simultaneous equations," *Math. Comp*., vol. 19, pp. 577–593, 1965.
[78] CST Corporation, USA, *http://www.cst.com*.
[79] J. W. Bandler, R. M. Biernacki, S.H. Chen, P. A. Grobelny, and S. Ye, "Yield-driven electromagnetic optimization via multilevel multidimensional models," *IEEE Trans. Microwave Theory Tech*., vol. 41, no. 12, pp. 2269–2278, Dec. 1993.
[80] L. Young and B.M. Schiffman, "A useful high-pass filter design," *Microwave J.*, vol. 6, no. 2, pp. 78–80, Feb. 1963.
[81] N. Marcuvitz, *Waveguide Handbook.* 1st ed. New York: McGraw-Hill, pp. 221, 1951
[82] R. Simovski, P. A. Belov, and H. Sailing, "Backward wave region and negative material parameters of a structure formed by lattices of wires and split-ring resonators," *IEEE Trans. Antennas Propag.*, vol. 51, no. 10, pp. 2582–2591, Oct. 2003.
[83] E. Ozbay, K. Aydin, E. Cubukcu, and M. Bayindir, "Transmission and reflection properties of composite double negative metamaterials in free space," *IEEE Trans. Antennas Propag.*, vol. 51, no. 10, pp. 2592–2595, Oct. 2003.

[84] R. W. Ziolkowski and A. D. Kipple, “Application of double negative materials to increase the power radiated by electrically small antennas,” *IEEE Trans. Antennas Propag.*, vol. 51, no. 10, pp. 2626–2640, Oct. 2003.

[85] C. Caloz and T. Itoh, *Electromagnetic Metamaterials: Transmission Line Theory and Microwave Applications*, John Wiley and Sons, Inc., 2006.

[86] D. Kwon and D. H. Warner, “Transformation electromagnetcis: an overview of the theory and applications,” *IEEE Antennas and Propag. Mag.*, vol. 52, no. 1, pp. 24–46, Feb. 2010.

[87] J. Zhu and G. V. Eleftheriades, “Experimental verification of overcoming the diffraction limit with a volumetric Veselago-Pendry transmission line lens,” *Phy. Rev. Lett.*, vol. 101, no. 1, pp. 013902-1–4, Jul. 2008.